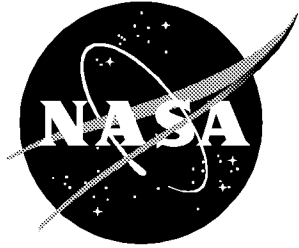


NASA/TM-2000-210079



Test-to-Test Repeatability of Results From a Subsonic Wing-Body Configuration in the National Transonic Facility

*Raymond E. Mineck and Odis C. Pendergraft, Jr.
Langley Research Center, Hampton, Virginia*

March 2000

The NASA STI Program Office . . . in Profile

Since its founding, NASA has been dedicated to the advancement of aeronautics and space science. The NASA Scientific and Technical Information (STI) Program Office plays a key part in helping NASA maintain this important role.

The NASA STI Program Office is operated by Langley Research Center, the lead center for NASA's scientific and technical information. The NASA STI Program Office provides access to the NASA STI Database, the largest collection of aeronautical and space science STI in the world. The Program Office is also NASA's institutional mechanism for disseminating the results of its research and development activities. These results are published by NASA in the NASA STI Report Series, which includes the following report types:

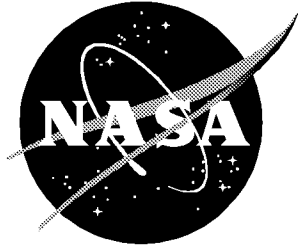
- **TECHNICAL PUBLICATION.** Reports of completed research or a major significant phase of research that present the results of NASA programs and include extensive data or theoretical analysis. Includes compilations of significant scientific and technical data and information deemed to be of continuing reference value. NASA counterpart of peer-reviewed formal professional papers, but having less stringent limitations on manuscript length and extent of graphic presentations.
- **TECHNICAL MEMORANDUM.** Scientific and technical findings that are preliminary or of specialized interest, e.g., quick release reports, working papers, and bibliographies that contain minimal annotation. Does not contain extensive analysis.
- **CONTRACTOR REPORT.** Scientific and technical findings by NASA-sponsored contractors and grantees.
- **CONFERENCE PUBLICATION.** Collected papers from scientific and technical conferences, symposia, seminars, or other meetings sponsored or co-sponsored by NASA.
- **SPECIAL PUBLICATION.** Scientific, technical, or historical information from NASA programs, projects, and missions, often concerned with subjects having substantial public interest.
- **TECHNICAL TRANSLATION.** English-language translations of foreign scientific and technical material pertinent to NASA's mission.

Specialized services that complement the STI Program Office's diverse offerings include creating custom thesauri, building customized databases, organizing and publishing research results . . . even providing videos.

For more information about the NASA STI Program Office, see the following:

- Access the NASA STI Program Home Page at <http://www.sti.nasa.gov>
- Email your question via the Internet to help@sti.nasa.gov
- Fax your question to the NASA STI Help Desk at (301) 621-0134
- Telephone the NASA STI Help Desk at (301) 621-0390
- Write to:
NASA STI Help Desk
NASA Center for AeroSpace Information
7121 Standard Drive
Hanover, MD 21076-1320

NASA/TM-2000-210079



Test-to-Test Repeatability of Results From a Subsonic Wing-Body Configuration in the National Transonic Facility

*Raymond E. Mineck and Odis C. Pendergraft, Jr.
Langley Research Center, Hampton, Virginia*

National Aeronautics and
Space Administration

Langley Research Center
Hampton, Virginia 23681-2199

March 2000

Available from:

NASA Center for AeroSpace Information (CASI)
7121 Standard Drive
Hanover, MD 21076-1320
(301) 621-0390

National Technical Information Service (NTIS)
5285 Port Royal Road
Springfield, VA 22161-2171
(703) 605-6000

Abstract

Results from three wind tunnel tests in the National Transonic Facility of a model of an advanced-technology, subsonic-transport wing-body configuration have been analyzed to assess the test-to-test repeatability of several aerodynamic parameters. The scatter, as measured by the prediction interval, in the longitudinal force and moment coefficients increases as the Mach number increases. Residual errors with and without the ESP tubes installed suggest a bias leading to lower drag with the tubes installed. Residual errors as well as average values of the longitudinal force and moment coefficients show that there are small bias errors between the different tests.

Introduction

Data quality or error from wind tunnel test measurements should be known in order to determine the magnitude of variation that is meaningful before using wind tunnel test results. The error in the test measurements has two components: bias error and precision (or repeatability) error. The bias error is the fixed, systematic, or constant component and the precision error is the random component. Proper experimental procedures can eliminate large bias errors but generally small bias errors remain in the measurements. Without knowing the true value, it is difficult to determine the bias error. One means of assessing the precision error is to compare repeated measurements on a common configuration within a single wind tunnel test (short-term repeatability) or over several wind tunnel tests (long-term repeatability). The potential for introducing bias errors into the measurements increases when going from short-term repeatability to long-term repeatability. Short-term repeatability of results from within a test on a subsonic transport configuration tested in the National Transonic Facility (NTF) was documented in reference 1. This report will investigate the long-term repeatability of results on a different subsonic transport configuration over three tests in the NTF.

A scale model of an advanced-design transonic wing for a conceptual subsonic transport has been tested in several tunnel entries in the NTF. The wing is designed for a tail-off lift coefficient of 0.6 at a Mach number of 0.85 and Reynolds number of 30×10^6 based on the mean aerodynamic chord. One model configuration, the wing-body alone, was tested at high Reynolds number in three wind tunnel tests, designated tests 62, 79, and 87. Test 62 was conducted in 1994, and tests 79 and 87 were conducted in 1996. Effects of boundary layer transition, Reynolds number, and aeroelasticity on the aerodynamic characteristics from test 62 are reported in reference 2.

The purpose of this report is to assess the long-term repeatability of data from the NTF for a wing-body configuration representative of a subsonic transport. The primary aerodynamic parameters used in the assessment

were the lift, drag, pitching moment, and surface static pressure coefficients. The limited amount of repeat data points within a single test typically precluded a detailed statistical analysis of the precision error. Comparisons of these aerodynamic parameters obtained from the different tests are presented herein at Mach numbers from 0.80 to 0.85 at a Reynolds number of 30×10^6 and at a Mach number of 0.85 at Reynolds numbers of 25×10^6 and 20×10^6 based on the mean aerodynamic chord.

Symbols and Abbreviations

b	span, in.
\bar{c}	mean aerodynamic chord, in.
c_r	root chord, in.
c_t	tip chord, in.
C_A	axial-force coefficient
C_D	drag coefficient
$C_{D,b}$	body cavity pressure correction to the drag coefficient
C_L	lift coefficient
C_m	pitching-moment coefficient
C_N	normal-force coefficient
C_p	wing upper surface static pressure coefficient
$C_{p,b}$	body cavity pressure coefficient
E	wing material modulus of elasticity (Young's modulus), lb/ft ²
ESP	electronically scanned pressure
FRP	fuselage reference plane
FS	fuselage station, in.
LE	leading edge
M_∞	Mach number
NTF	National Transonic Facility
q	dynamic pressure, lb/ft ²
R_c	Reynolds number based on mean aerodynamic chord

T_t	stagnation temperature, °F
TE	trailing edge
x/c	local chord fraction
α	angle of attack, deg
α_f	test section flow angularity, deg
Δ	residual error (difference between measured value and the estimated mean value from the curve fit)
η	wing semispan fraction
Λ	wing sweep angle, deg
λ	taper ratio

Experimental Apparatus and Procedures

Test Facility

The National Transonic Facility is a fan-driven, closed-circuit, continuous-flow, pressurized wind tunnel (ref. 3). It may be operated as a conventional wind tunnel using air as a test gas or as a cryogenic wind tunnel using nitrogen as a test gas. NTF capabilities allow testing of aircraft configurations at speeds ranging from low subsonic to low supersonic, at Reynolds numbers up to full-scale flight values (depending on aircraft type and size). The test section is 8.2 feet by 8.2 feet in cross section and 25 feet in length. Longitudinal slots in the floor and ceiling give wall-openness ratios of 6 percent. The test-section sidewalls are solid. The NTF is capable of an absolute pressure range from 15 psi to 125 psi, a stagnation temperature range from -320°F to 150°F , a Mach number range from 0.2 to 1.2, and a maximum Reynolds number per foot of 146×10^6 at Mach 1.

Free stream turbulence is reduced by four damping screens and the 15:1 contraction ratio between the settling chamber and the test section. An initial assessment of the flow quality in the NTF has been reported in reference 4. Conventional model support is provided by an aft-mounted sting attached to a vertically mounted arc sector. The pitch range of the arc sector is from about -11° to 19° , depending on the test setup. A remotely controlled roll coupling, with a range from -180° to 180° , provides the interface between the arc sector and the sting. The test-section floor, ceiling, and reentry flap angles were fixed during these tests.

Model Description

The wind-tunnel model wing is a 2.426-percent scale representation of a conceptual subsonic transport aircraft design by the Boeing Aircraft Company, Long Beach Division (the former Douglas Aircraft Company of the McDonnell Douglas Corporation). The wing, designated

W44, incorporates divergent trailing-edge technology (ref. 5) and an aggressive design strategy that includes an aft shock position and a steep pressure recovery gradient approaching the trailing edge. A photograph of the model installed in the NTF test section is presented in figure 1. Sketches of the model general arrangement, details of the wing geometry, and the wing pressure orifice locations are presented in figure 2. The wing is designed for a tail-off lift coefficient of 0.6 at a Mach number of 0.85 and a Reynolds number of 30×10^6 based on mean aerodynamic chord. The planform has an aspect ratio of 9.0, a taper ratio of 0.3, and a dihedral angle of 3.0° . The quarter-chord line is swept back 35° . Other model dimensional characteristics are presented in table 1 and in figure 2. The model was fabricated from Vascomax C-200 steel with a surface finish of 16 microinches or less. To accommodate static-aeroelastic deformation under load, the wing is fabricated to deform to the design shape at NTF test conditions corresponding to the design point ($M_{\infty} = 0.85$, $R_c = 30 \times 10^6$, $T_t = -250^{\circ}\text{F}$, $q = 2000$ psf).

The wing contains 225 static-pressure orifices: 203 orifices distributed in 12 chordwise rows (7 rows on the wing upper surface and 5 rows on the wing lower surface), and 22 orifices distributed along the wing trailing edges as shown in figure 2(c). The nominal orifice diameter was 0.015 inches. Because of the large number of wing pressure orifices and the volume of the associated pressure tubing, the orifices are distributed over both wings. To simplify model fabrication and maximize wing strength, upper-surface orifices are located in the right-hand wing and lower-surface orifices are located in the left-hand wing. Body cavity pressure is measured at two locations inside the fuselage cavity.

The model wing is designed for use with existing NTF Pathfinder-I subsonic transport model fuselage components (ref. 6). A 10.5-in. fuselage extension plug that properly scales the fuselage length to the wing span for the conceptual aircraft design is inserted between the nose and wing. The model configuration used in the tests documented in this report consists of the wing, fuselage, and wing-fuselage fillets but without the flap track fairings, nacelles, and pylons. The base of the fuselage was tapered to a thickness of 0.040 inches at the trailing edge.

Instrumentation

Aerodynamic force and moment data were obtained with a six-component, strain-gage balance. For each test, the NTF balance with the smallest load capacity that exceeded the expected model loads was selected. All NTF balances were not always available because of periodic maintenance such as moisture proofing. Thus, different balances were used for the different tests as shown

in table 2. The accuracy of each longitudinal component of each balance was determined from the measured and applied loads from the balance calibration. Loadings that were outside of the test envelope, such as the lateral balance component loadings and the negative normal force loadings, were eliminated from the determination of the balance accuracy. From the remaining loadings, the balance accuracy for each of the longitudinal components is stated in terms of the worst outlying point in the calibration. The full scale loads and quoted accuracies are presented as a percent of the full-scale loads in table 2.

An onboard, heated, single-axis accelerometer package was used to measure the model angle of attack. The accelerometer package has a quoted accuracy of $\pm 0.01^\circ$ under smooth wind-tunnel operating conditions (ref. 7). For the test conditions presented in this report, the model dynamic acceleration was small and was not expected to have a significant impact on the accuracy of the angle of attack measurement.

Wing-pressure measurements were made with six 48-port, electronically scanned pressure (ESP) modules contained in an internal, nose-mounted, heated enclosure. The upper surface (right wing) pressures were measured using modules having a full-scale pressure range of ± 45 psid; the lower surface (left wing) pressures were measured using modules having a range of ± 30 psid. The quoted accuracy of the modules was ± 0.20 percent of full scale pressure. The modules were calibrated immediately before each series of runs.

Body cavity pressures were measured at two locations inside the fuselage cavity using externally located, ± 5 psid pressure transducers with a worst case system accuracy of 0.05 psi plus 0.37 percent of the measurement (ref. 8).

The wind tunnel total and static pressures were measured using two banks of quartz bourdon tube transducers referenced to a vacuum. A controller selects the smallest transducer from each bank capable of measuring the total and the static pressures. For the test conditions reported herein, a 50 psi transducer with an accuracy of ± 0.012 percent of reading and ± 0.006 percent of full scale was used for each measurement. The tunnel total temperature was measured with a platinum resistance thermometer with an accuracy of $\pm 0.2^\circ\text{F}$.

Procedures, Data Reduction, and Corrections

Reference 8 provides information on NTF instrumentation devices, tunnel process and data-acquisition systems, and data-reduction algorithms. Balance output is sensitive to the balance temperature as well as the balance longitudinal temperature gradient. Balance readings were compensated for changes in balance temperature

between the wind-on and wind-off conditions. Also, temperature gradients within the balance were minimized by allowing the balance to approach thermal equilibrium with the stream before recording any data. Balance-temperature gradients of less than 10°F were maintained throughout these tests. Wind-off data were acquired prior to and following each set of runs to monitor balance electrical zero shifts over the course of a run set. The ending wind-off point was used for all data reduction because the thermal state of the balance (for both temperature and temperature gradient) at the end of a run set was generally more representative of the wind-on conditions.

Axial force and drag were corrected to the condition of free-stream static pressure acting in the body cavity. No corrections were required for normal force or pitching moment for the static pressure acting in the body cavity. A buoyancy correction was applied to the drag coefficient based on the longitudinal Mach number gradient measured in the test section during the tunnel calibration. The data used in this report were not corrected for test-section wall interference or sting interference.

The model angle of attack was corrected for upflow in the test section, with the upflow angle determined from data acquired with the model in both upright and inverted orientations at a given set of tunnel conditions. Over the range of Mach number used in this study, the upflow angle variation with Mach number was negligible (reference 2). In each test, an upright and inverted run was obtained for each Reynolds number at the design Mach number, 0.85, and the resulting upflow correction applied across the Mach number range. Calculated flow angularities for the three tests are presented in figure 3. Results at nominal stagnation temperatures of -185°F , -225°F , and -250°F correspond to Reynolds numbers of 20×10^6 , 25×10^6 , and 30×10^6 , respectively. Results from all three tests show a reduction in the flow angularity as the temperature decreases. The spread in the flow angularity is similar to the scatter in the flow angularity reported in the data repeatability study in reference 1.

All results presented herein were obtained with natural boundary layer transition; that is, no artificial boundary layer trip strips were used. Each tunnel entry was identified by a unique test number: 62, 79, and 87. Each polar (angle-of-attack sweep) in a given tunnel entry was identified by a unique run number. All polars were obtained in a "pitch-pause" mode in which the model is pitched to the next angle of attack in the series, transients in the flow and instrumentation are allowed to damp out, and the data are then recorded before repeating the cycle.

The effect of wing static aeroelastic deformation is minimized in the comparison of the results from the three tests. Static aeroelastic deformation of the wing depends on the applied load and the material stiffness. An indica-

tor of static aeroelastic deformation is the nondimensional ratio of dynamic pressure (q), to the modulus of elasticity (E) for the metal that comprises the wing. The parameter q/E is appropriate for characterizing aeroelastic condition because the material stiffness E increases as the temperature decreases. To minimize the effects of static aeroelastic deformation on the comparisons, only results at the nominal ratio of $q/E = 0.5 \times 10^{-6}$ are used in this report.

Test 62 was divided into two phases: an initial phase in which balance (force and moment) and wing pressure data were acquired, and a final phase in which only balance data were acquired. In test 79, balance (force and moment) and wing pressure data were acquired. In test 87, only balance (force and moment) data were acquired. Wing pressure data acquisition required ESP hardware (tubing for the reference pressure, calibration pressure, and control pressure and electrical wires for data acquisition and control) to bridge the balance. The wires and tubing that bridge the balance were removed for the balance only testing, removing the influence of the ESP hardware on the balance measurements. Previous test experiences (e.g. ref. 2) indicated that the presence of the ESP instrumentation had a small effect on the lift and pitching moment measurements but could have a significant effect on the drag measurements. Thus, drag data from the NTF measured with the ESP hardware present have been used with caution and are frequently excluded in the analysis of the test results.

Analysis

The accuracy of the measurement instruments was used to estimate the error bands for the model force and moment coefficients and the wing static pressure coefficients for the loads encountered near the angle of attack for the design lift coefficient using the technique described in reference 9. Error bands for the force and moment coefficients based on the quoted instrumentation accuracies for the three tunnel tests are presented in table 3. The error estimate for the static pressure coefficient was about ± 0.005 over the Mach number range for tests 62 and 79.

The results presented in the Appendix from the three tests were analyzed to investigate the long-term or test-to-test repeatability at the design lift coefficient using the regression statistical analysis of reference 1. There was not a statistically significant number of repeat runs in each test to investigate the short-term or within-test repeatability. Statistical analysis of the combined results from all three tests will be used to determine the precision or repeatability error.

The statistical analysis was applied to the results for lift coefficients from 0.50 to 0.70. In general, the flow

was well behaved over this range reducing the potential for unsteady, separated flow phenomena that could affect repeatability. The estimated mean value was calculated from a fourth-order polynomial regression equation fitted to the results. From the measured data and the estimated mean value, the residual error, the confidence interval, and the prediction interval were determined. The confidence interval is the bounds about the estimated mean that encompass the true mean with a 95-percent probability. The prediction interval is the bounds about the estimated mean that will contain any single future measurement with a 95-percent probability. The confidence interval is related to the location of the true mean and the prediction interval is a measure of the data scatter. As defined in reference 1, confidence and prediction intervals are inversely proportional to the number of measurements in the data set and the local density of the measurements. Thus, at the ends of the intervals, the local density of points decreases and the confidence and prediction intervals widen.

Results and Discussion

The results from the regression statistical analysis of the longitudinal force and moment coefficients are presented in figures 4 to 6. The lower part of each figure presents the measurements from the tests (in the range of interest of C_L from 0.5 to 0.7) and the estimated mean value from the fourth order polynomial regression analysis. The upper part of the figure presents the residual error for each measurement and the 95-percent confidence and prediction intervals. Data points recorded with the ESP tubes crossing the balance are noted by solid symbols in the residual error plots.

The results associated with the statistical analysis of the lift coefficient at the five combinations of Mach number and Reynolds number are presented in figure 4. At a Reynolds number of 30×10^6 near the design lift coefficient, the prediction interval increases from about ± 0.0026 to about ± 0.0049 as the Mach number increases from 0.80 to 0.85 in spite of the increased number of measurements at a Mach number of 0.85. Scatter increases as the Mach number increases. The prediction interval does not change significantly with Reynolds number. Comparison of residual errors from test 62 with and without the ESP tubes installed does not show bias errors associated with the addition of the ESP tubes. The confidence interval ranges from ± 0.0005 to about ± 0.0012 for the five cases.

The results for the pitching-moment coefficient are presented in figure 5. The prediction interval for the pitching-moment coefficient increases from ± 0.0011 to ± 0.0026 with increasing Mach number. Residual errors from test 62 are generally more negative than the esti-

mated mean value suggesting that there is a bias error present. Residual errors from test 62 do not show a strong effect of the ESP tubes on the pitching-moment coefficient. The confidence interval ranges from ± 0.0002 to ± 0.0007 .

The results for the drag coefficient are presented in figure 6. Frequently, drag coefficient data with the tubes installed are not included in the analysis but have been included in this study for completeness. The prediction interval varies over the five test conditions from ± 0.00025 to about ± 0.00042 . Examination of the residual errors indicates a change in the bias errors in each test in that the test 62 residual errors typically show increased drag and the test 79 residual errors typically show reduced drag relative to the estimated mean value. The residual errors with and without the ESP tubes installed in test 62 suggest a bias leading to a lower drag with the tubes installed. The confidence interval ranges from about ± 0.00007 to ± 0.00010 .

The drag coefficient is corrected for the pressure relative to the free-stream static pressure acting over the aft facing opening on the body. The results from the analysis of the drag-coefficient correction from the measured body cavity pressures are presented in figure 7. The prediction interval is about ± 0.0001 and the confidence interval is about ± 0.00002 at the design lift coefficient for all five cases. The repeatability error and the confidence interval for the correction to the drag coefficient are a small part of the repeatability and confidence interval of the drag coefficient. The residual errors for test 62 generally show a small negative bias.

Repeatability of the lift and drag coefficients include effects of the balance normal force and axial force measurements as well as the angle-of-attack measurement. To eliminate the angle-of-attack effects, the repeatability of the model axial-force coefficient was calculated as a function of the model normal-force coefficient and the results are presented in figure 8. The prediction interval varies over the five test conditions with values from ± 0.00024 to ± 0.00061 . These values are similar to those found for the variation of drag coefficient with lift coefficient in figure 6. Thus, much of the scatter in the lift and drag coefficients is associated with the balance measurement. For the test 62 results, the residual errors with the ESP tubes are generally less positive than the residual errors without the tubes. This suggests that there is a bias introduced with the addition of the ESP tubes. Also, the residual errors from test 62 are typically positive and the residual errors from test 79 are typically negative suggesting a bias between the tests.

The regression statistical analysis was applied to a sample of the wing pressure data at two spanwise stations: $\eta = 0.42$ and 0.85 ; the results are presented in fig-

ures 9 and 10. At $x/c = 0.05$, many of the residual errors from test 62 are positive and many from test 79 are negative (see part a of figures 9 and 10). This suggests that there might be a small bias between the two tests for some of the orifices. The regression analysis could not provide reasonable curve fits for cases in which the pressure coefficient rapidly changed between two levels, such as those at $x/c = 0.45$ in figure A5(c), so no prediction or confidence intervals are presented at those locations. For the angles of attack where the pressure is changing between the two levels, the flow is probably unsteady as the shock location changes with disturbances in the local flow. In these cases, the measured pressure coefficients show large scatter (for example, see $\alpha \approx 1.25^\circ$ in figure 9(c)). Although the flow was unsteady at the blunt trailing edge, the data scatter, represented by the prediction interval, is much smaller for the trailing edge orifices than for the wing upper surface orifices. The prediction intervals for the upper surface static pressures range from about ± 0.005 to about ± 0.019 whereas the prediction intervals for the trailing edge pressures are typically about ± 0.003 to ± 0.004 .

The bias error over several tests is likely to be larger than the bias error within a single test because of the possibility of introducing additional biases associated with preparing and installing the model. Change in the estimated mean value of a particular aerodynamic parameter from test to test could be used to estimate the change in the bias error between tests if a statistically significant number of runs were available. Since this is not the case herein, the average value of the lift, drag, and pitching-moment coefficients from each test are compared to provide an estimate of the bias error between the tests. Each polar from each test was fitted to a fourth-order, least-squares polynomial (over a range of C_L from 0.5 to 0.7). The curve fit was used to predict the lift coefficient at a nominal angle of attack and the pitching-moment and drag coefficients at a lift coefficient of 0.6. To be consistent with standard practice at the NTF, the drag data with the ESP tubes installed have been eliminated from the analysis.

The results from each test at a given Mach number and Reynolds number combination were averaged and the results are presented in figures 11 to 13. The change in the mean value of the lift coefficient between the three tests is typically on the order of the balance error band except at the lowest Mach number. The change in the average values of the pitching-moment coefficient was larger than the balance error bands. The change in the average value of the drag coefficient was less than the balance error bands. These results are indicative of the types of bias errors introduced into tests of this type of model using the procedures in place at the time of the test.

Concluding Remarks

Data from three tests of a wing-body configuration in the NTF have been analyzed to assess test-to-test repeatability. The results indicated that:

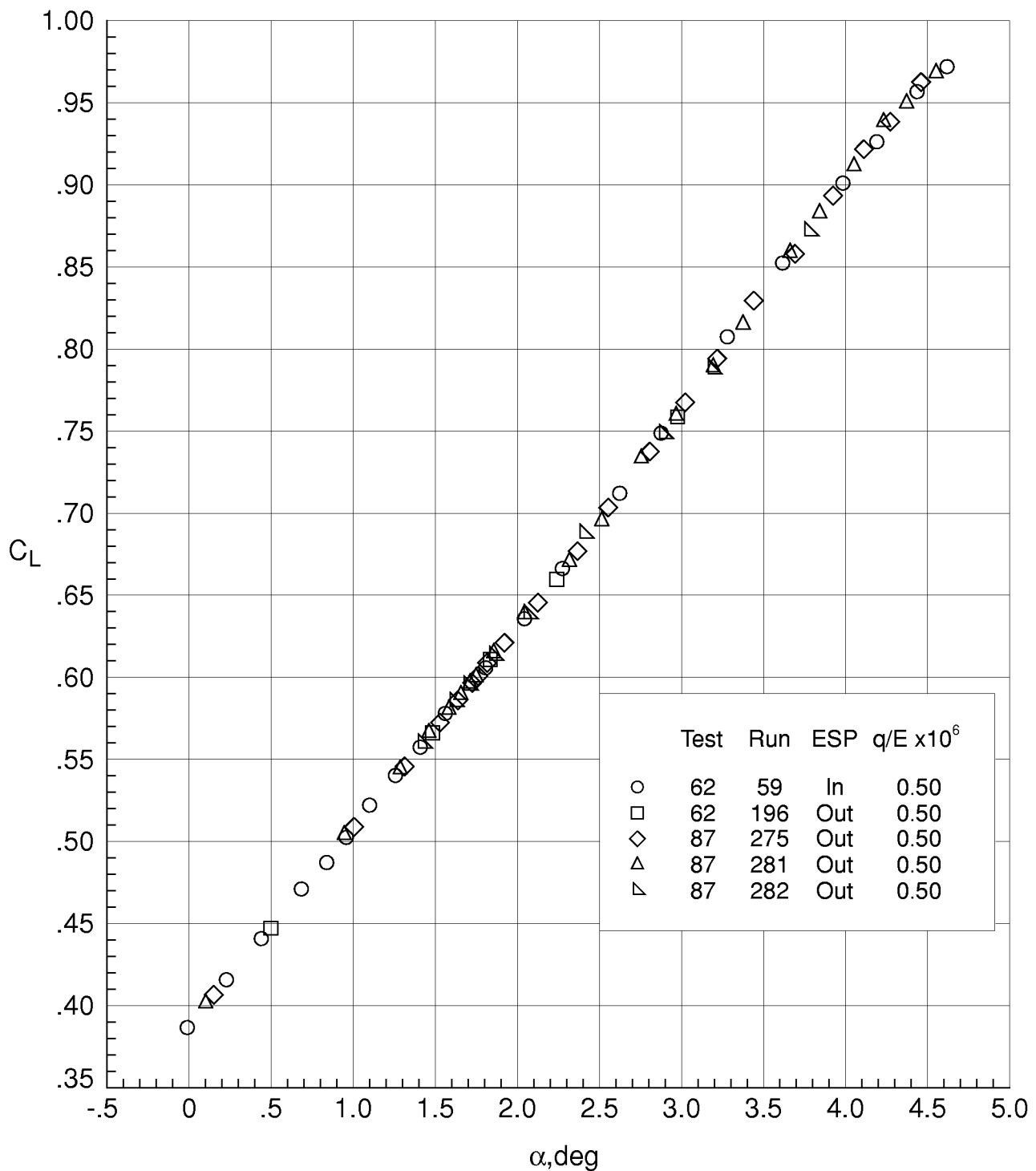
1. The scatter, as measured by the prediction interval, in the longitudinal force and moment coefficients increases as the Mach number increases.
2. Residual errors with and without the ESP tubes installed suggested a bias error leading to lower drag with the tubes installed.
3. Correction to the drag coefficient due to the model cavity pressure was a small contributor to the overall prediction and confidence intervals for the drag coefficient.
4. Much of the scatter in the lift and drag coefficients was associated with the balance measurement.
5. Residual errors as well as average values of the longitudinal force and moment coefficients show that there were small bias errors between the different tests.

NASA Langley Research Center
Hampton, VA 23681-2199
May 4, 1999

Appendix

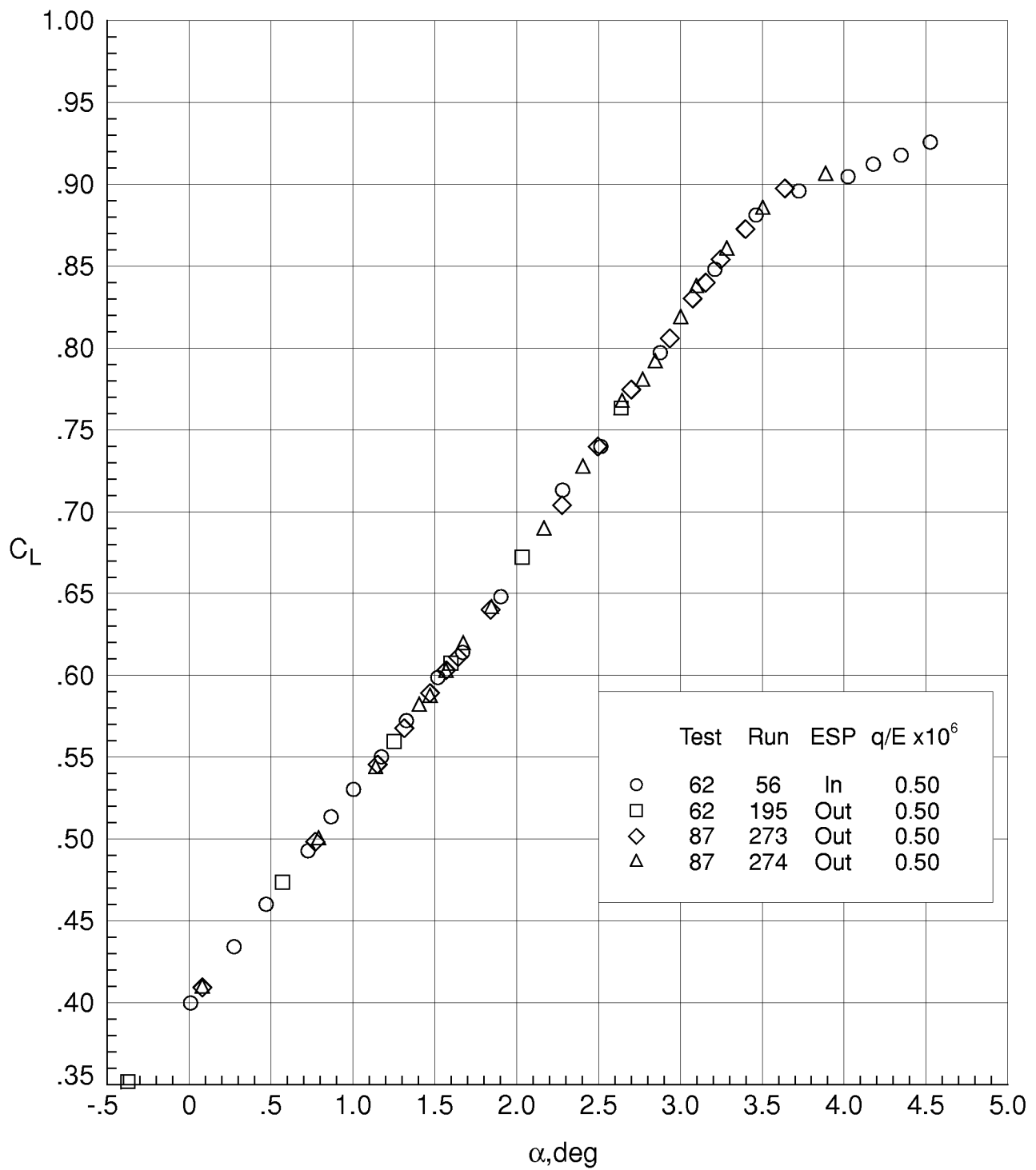
Results from the wing-body configuration from the different tests at Mach numbers of 0.80, 0.83, and 0.85 at a chord Reynolds number of 30×10^6 and for a Mach number of 0.85 at chord Reynolds numbers of 25×10^6 and 20×10^6 were selected for the repeatability analysis. Longitudinal force and moment coefficients are presented in figures A1 to A3. Model cavity pressure measurements used to correct the axial force and drag measurements are presented in figure A4. For the scales used to present the test results, all the balance longitudinal force and moment coefficients and the cavity pressure coefficients display detectable scatter.

Direct comparison of the measured chordwise pressure distributions from the different tests was not possible at the design lift coefficient. Rather, the variation of the pressure coefficient with angle of attack is presented in figure A5 at five chordwise location from $x/c = 0.05$ to $x/c = 1.00$ at a Mach number of 0.85 and a chord Reynolds number of 30×10^6 . Note that the trailing edge pressures ($x/c = 1.00$) were obtained from orifices facing downstream so the measurements will be for an unsteady flow. For the scales used, the scatter in the pressure coefficients is relatively small except where there is an abrupt change of pressure coefficient with angle of attack. This typically occurs when the shock location crosses a given location on the wing or, for the trailing edge pressures, when the boundary layer near the trailing edge is separated.



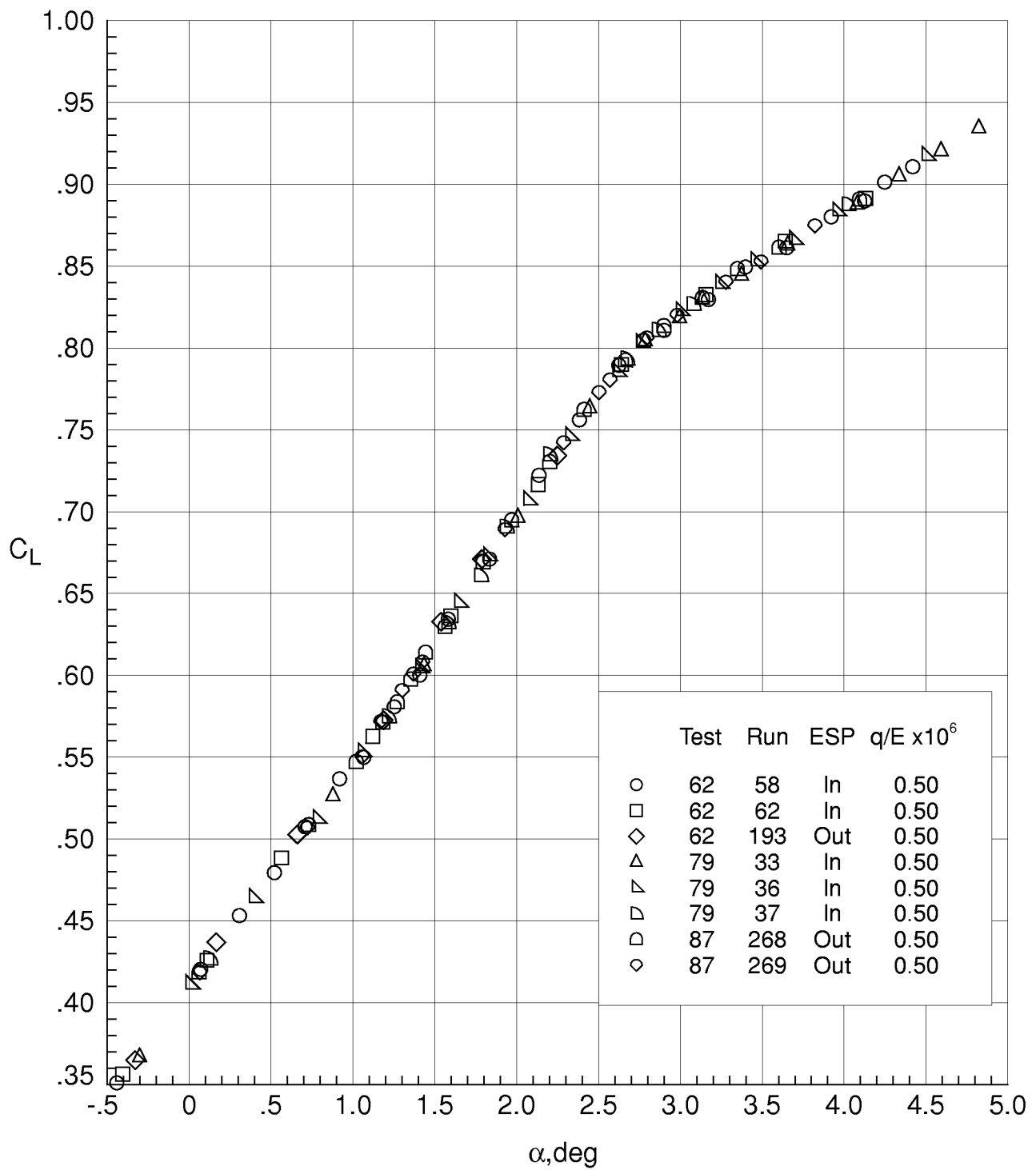
(a) $M_\infty = 0.80$. $R_{\bar{c}} = 30. \times 10^6$.

Figure A1. Comparison of the lift coefficient curves from the different tests.



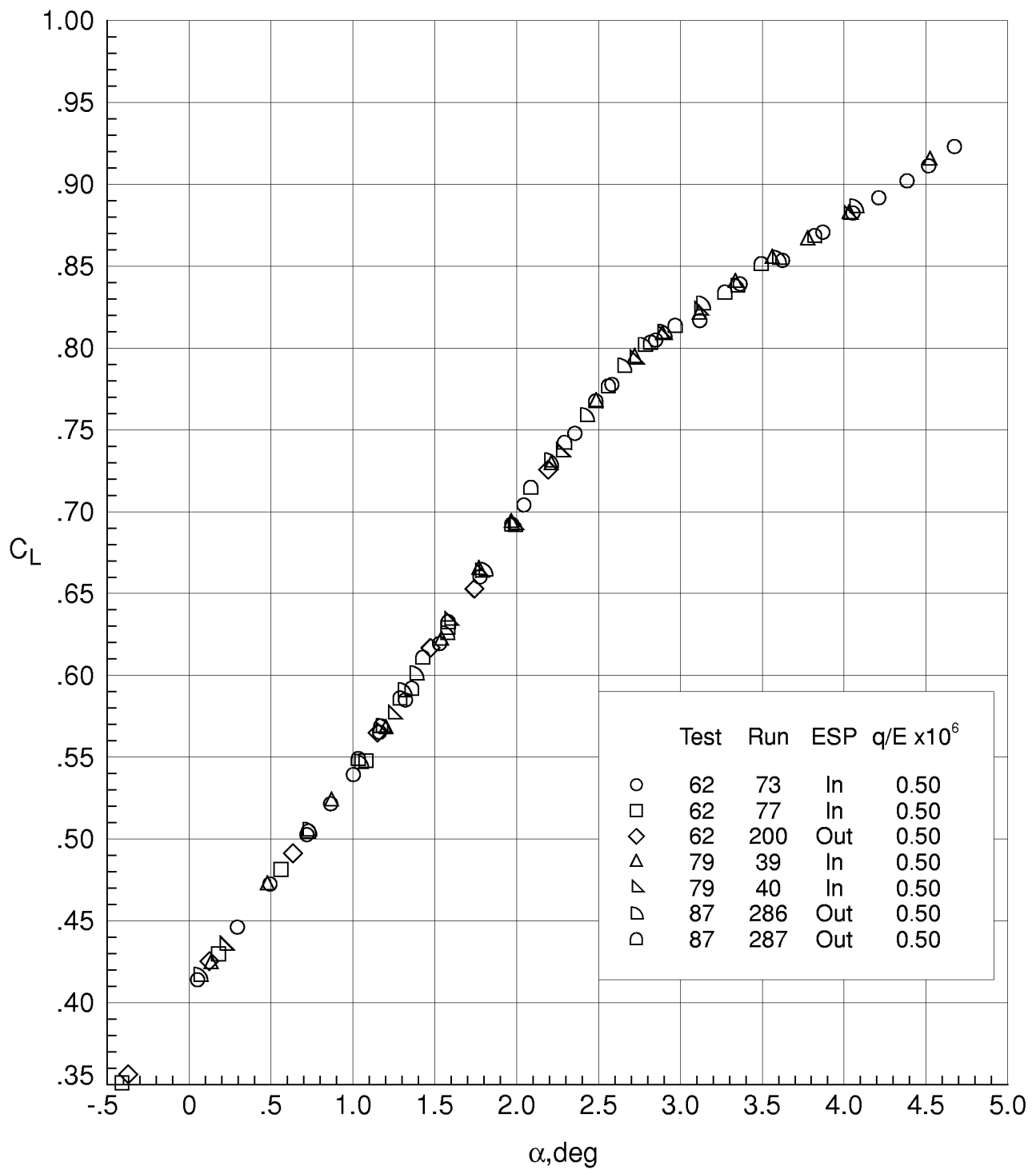
(b) $M_\infty = 0.83$. $R_{\bar{c}} = 30. \times 10^6$.

Figure A1. Continued.



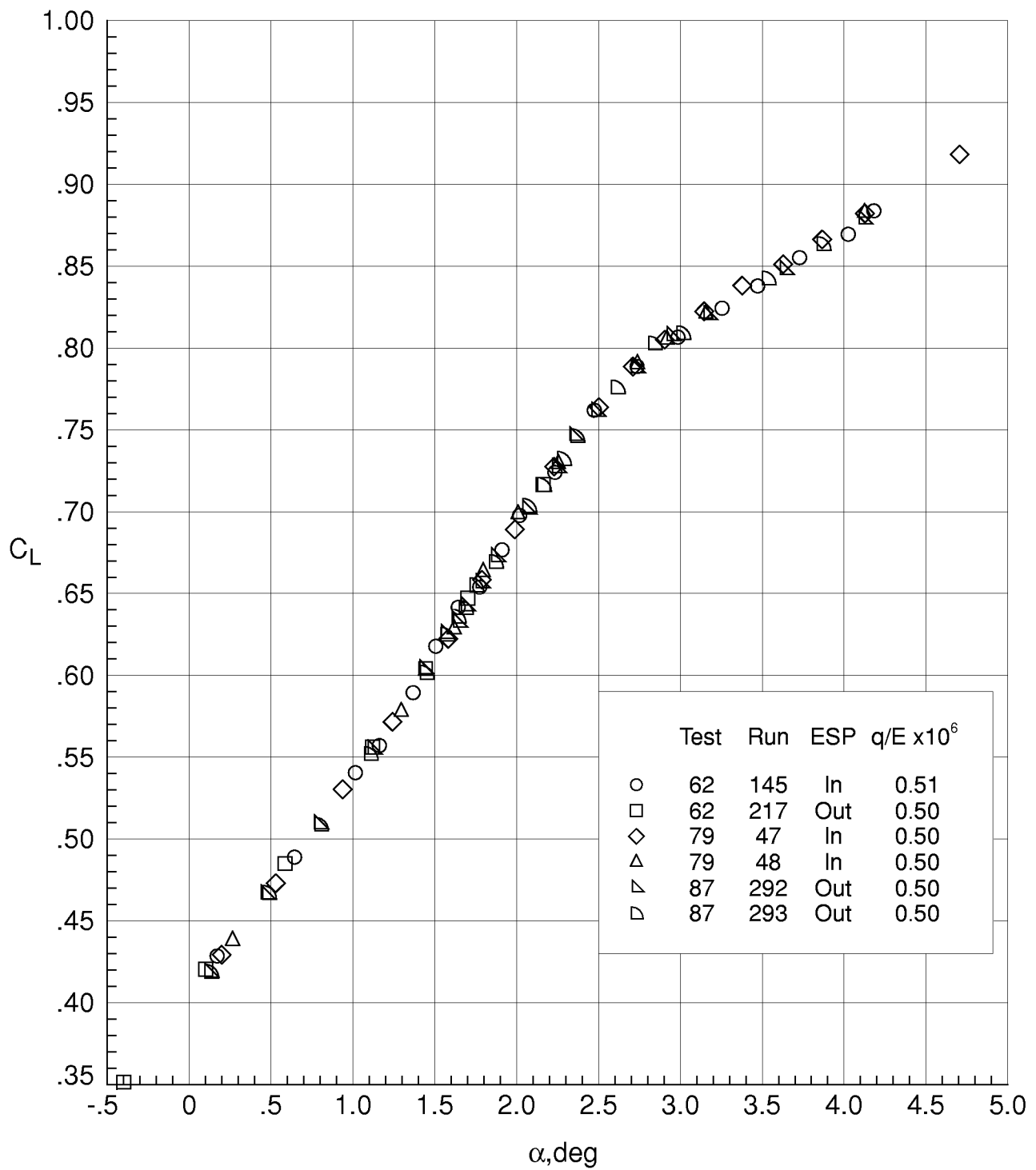
(c) $M_\infty = 0.85$. $R_{\bar{c}} = 30. \times 10^6$.

Figure A1. Continued.



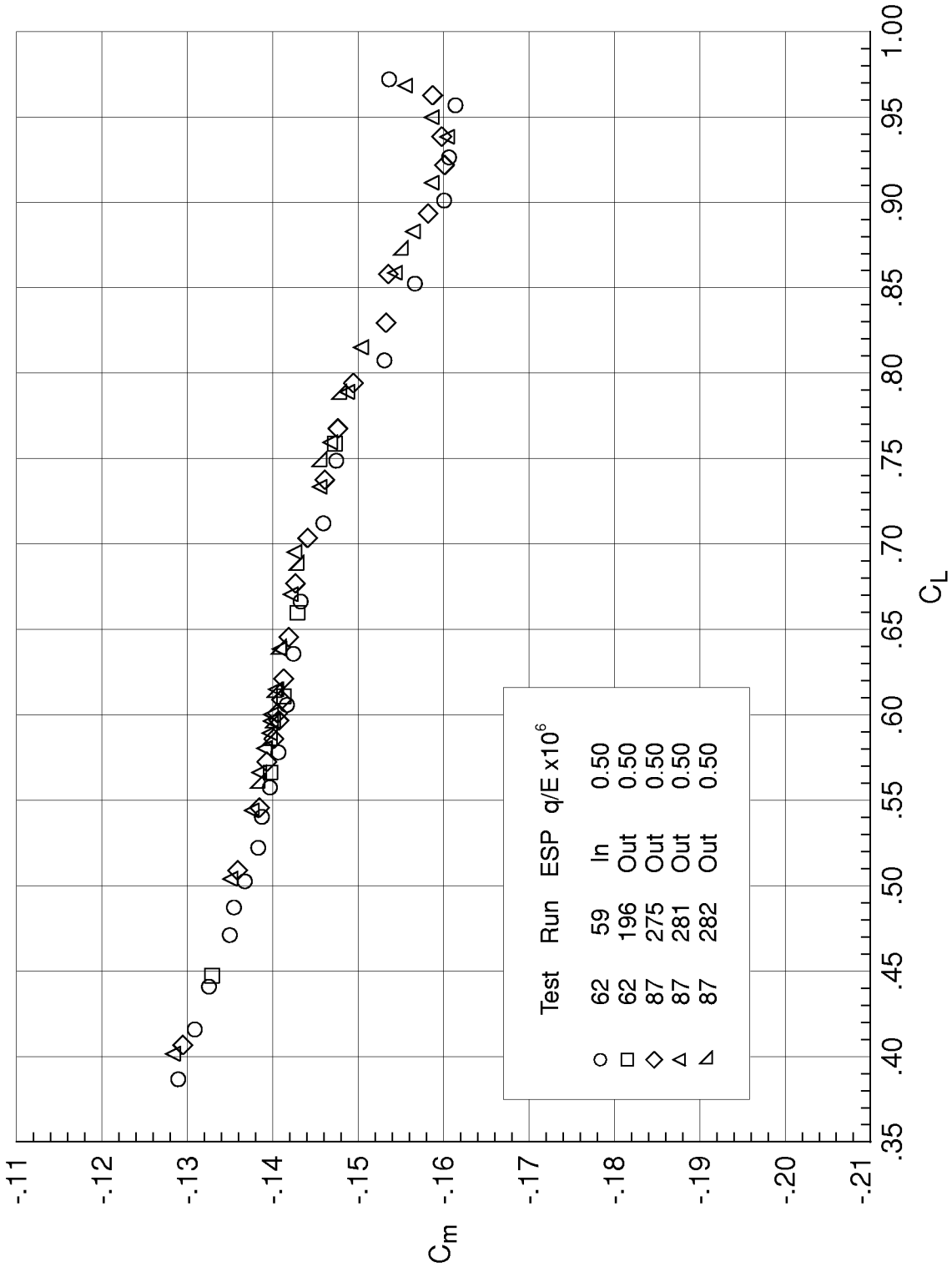
(d) $M_\infty = 0.85$. $R_{\bar{c}} = 25. \times 10^6$.

Figure A1. Continued.



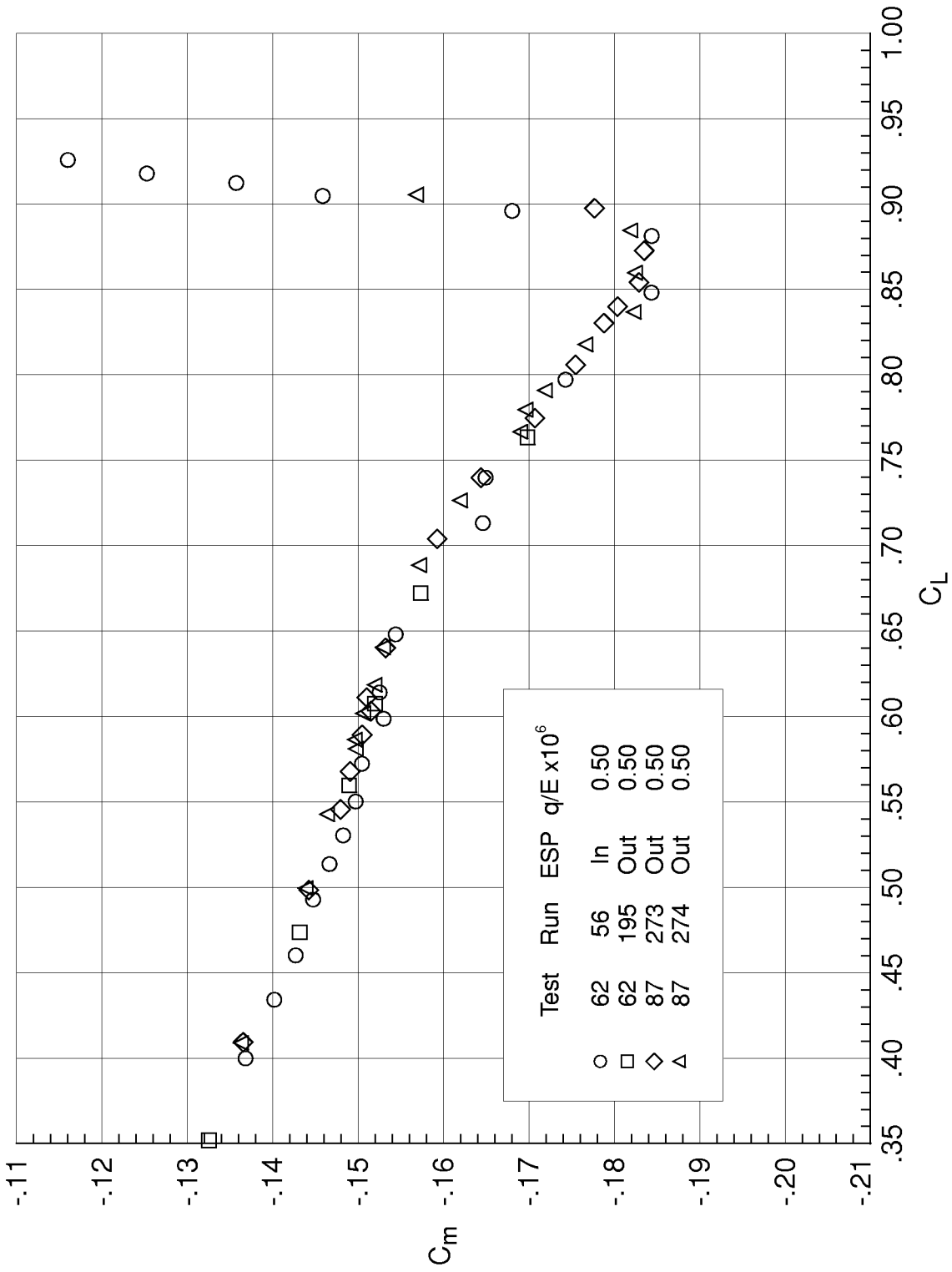
(e) $M_\infty = 0.85$. $R_{\bar{c}} = 20. \times 10^6$.

Figure A1. Concluded.



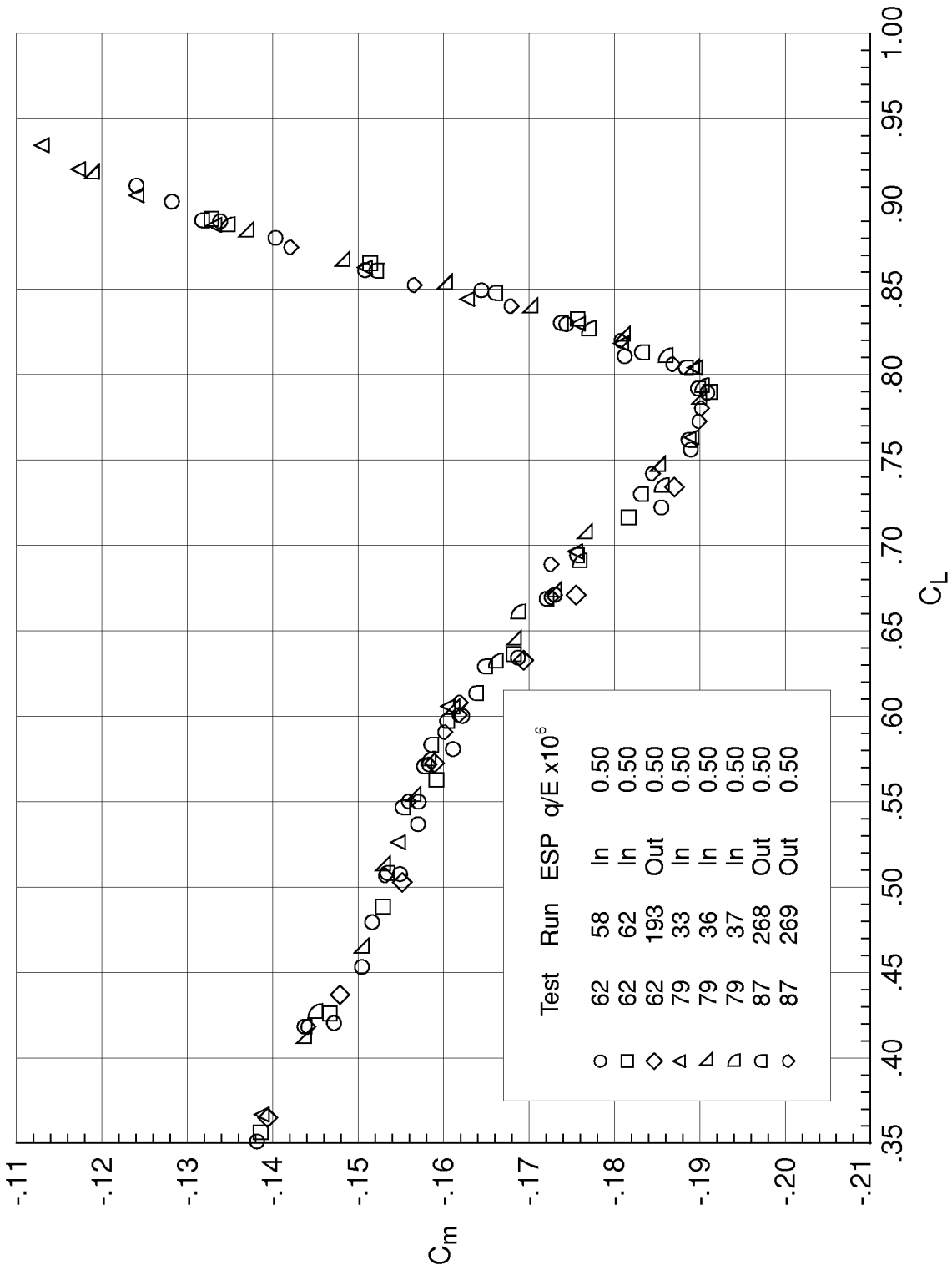
(a) $M_\infty = 0.80$. $R_c = 30. \times 10^6$.

Figure A2. Comparison of the pitching-moment coefficient curves from the different tests.



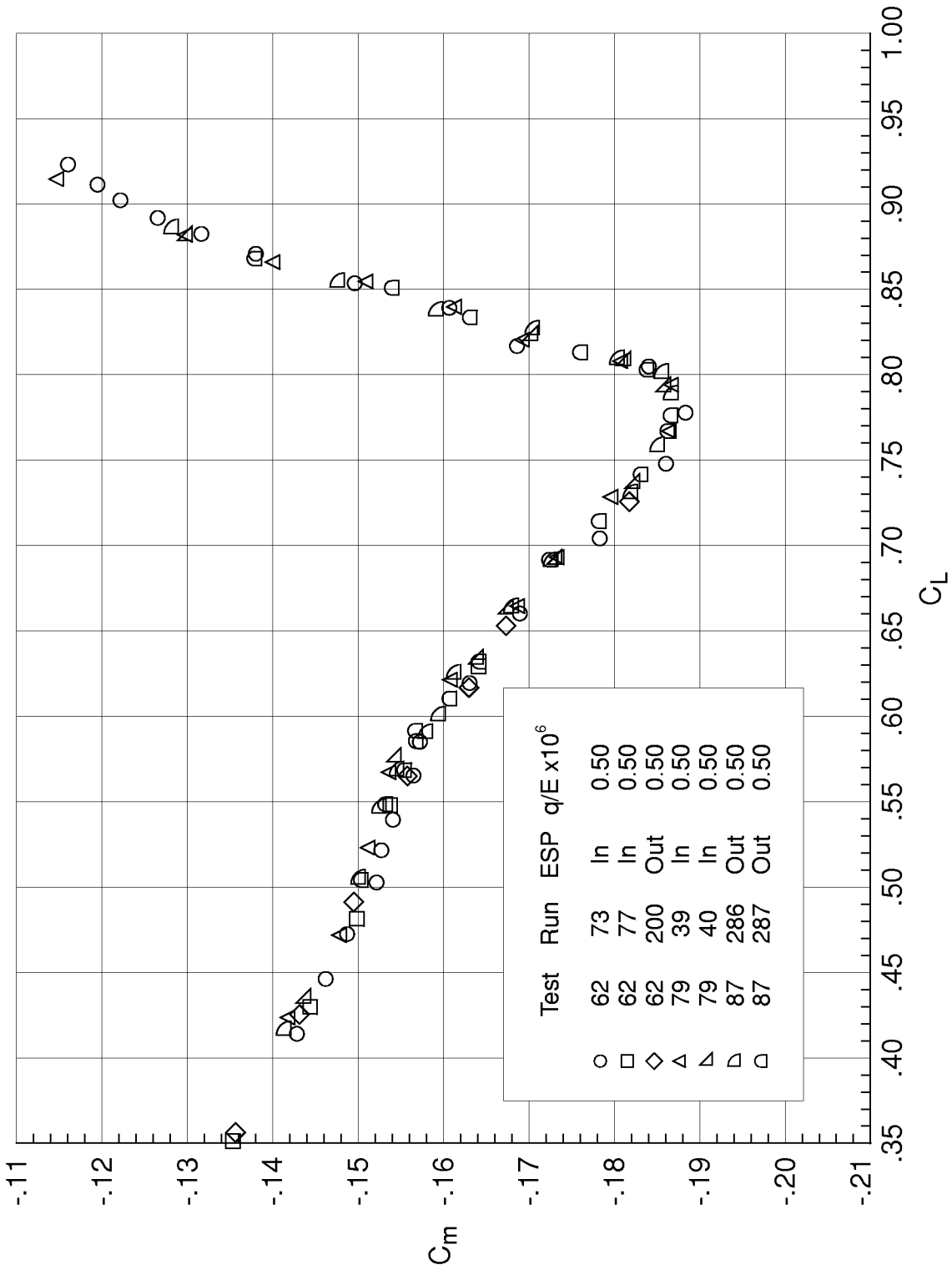
(b) $M_\infty = 0.83$. $R_c = 30. \times 10^6$.

Figure A2. Continued.



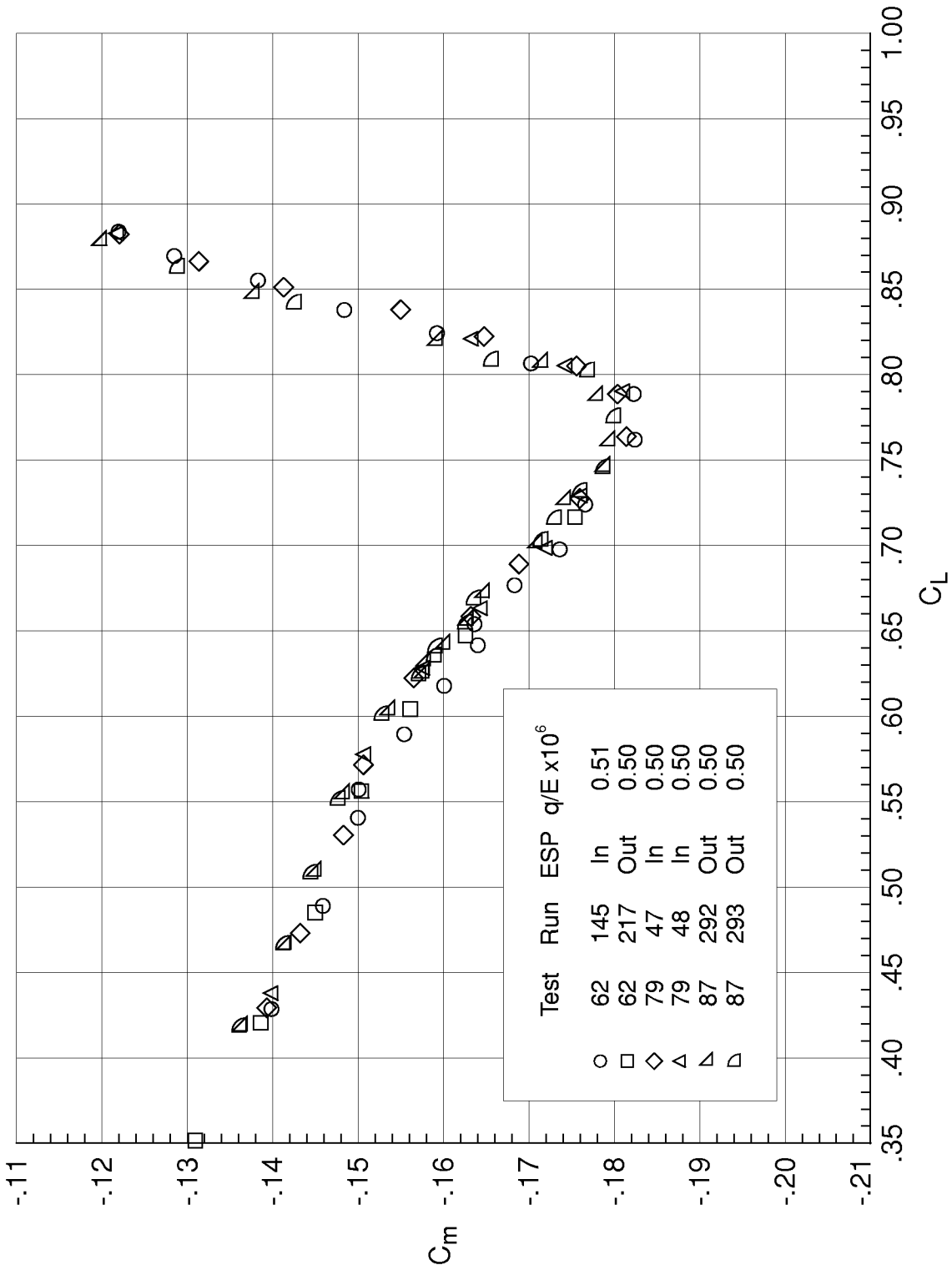
(c) $M_\infty = 0.85$, $R_c = 30. \times 10^6$.

Figure A2. Continued.



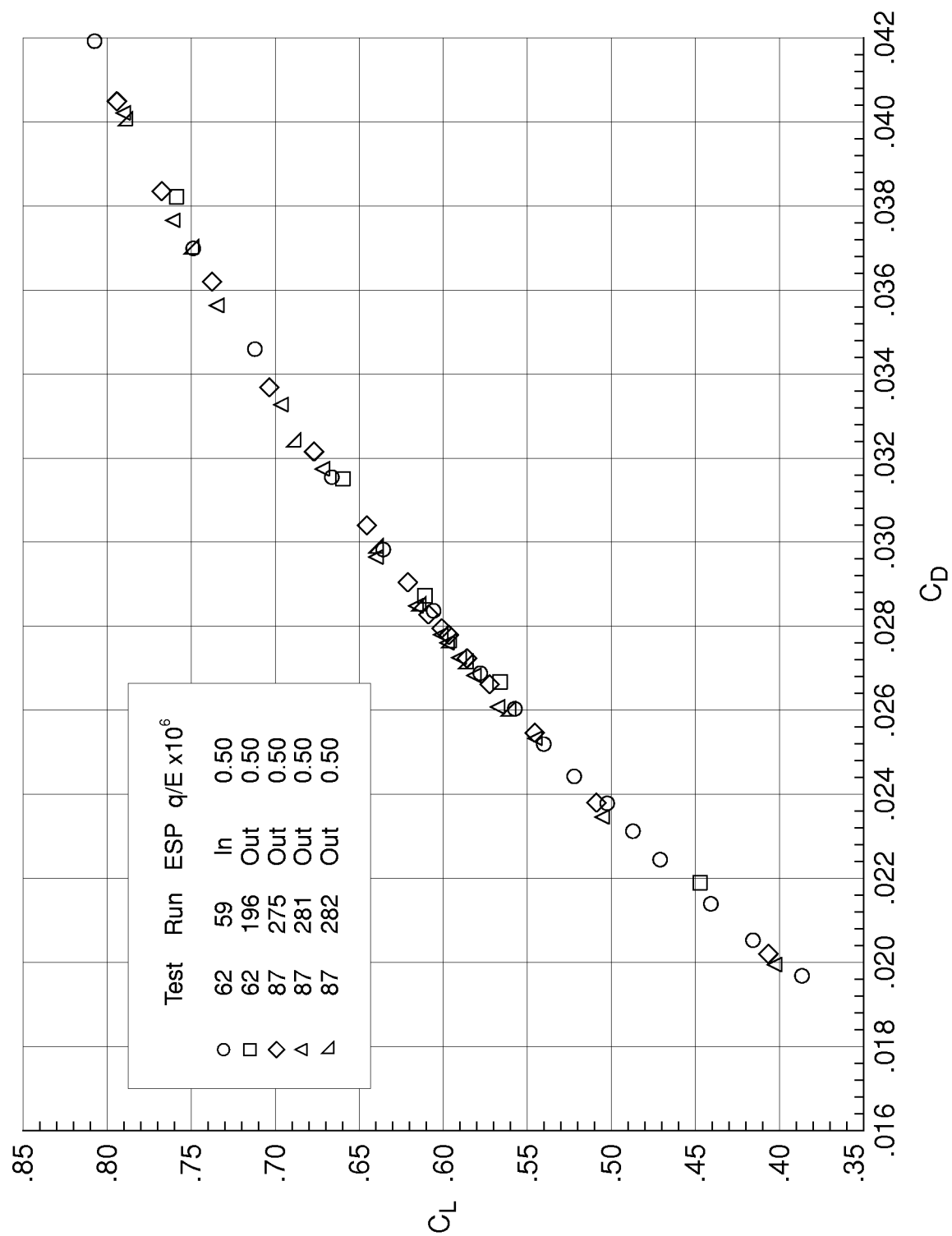
(d) $M_\infty = 0.85$. $R_c = 25. \times 10^6$.

Figure A2. Continued.



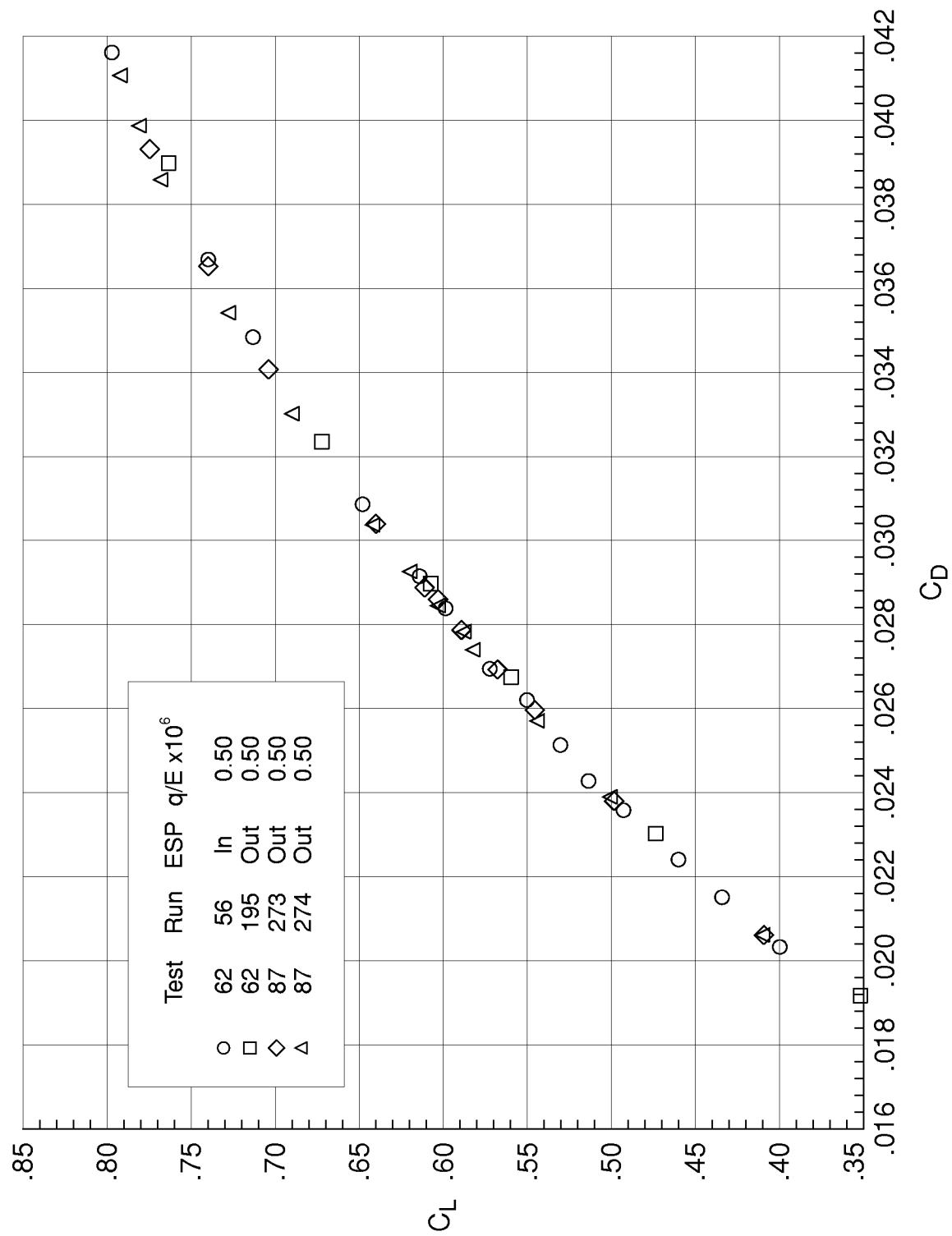
(e) $M_\infty = 0.85$. $R_c = 20. \times 10^6$.

Figure A2. Concluded.



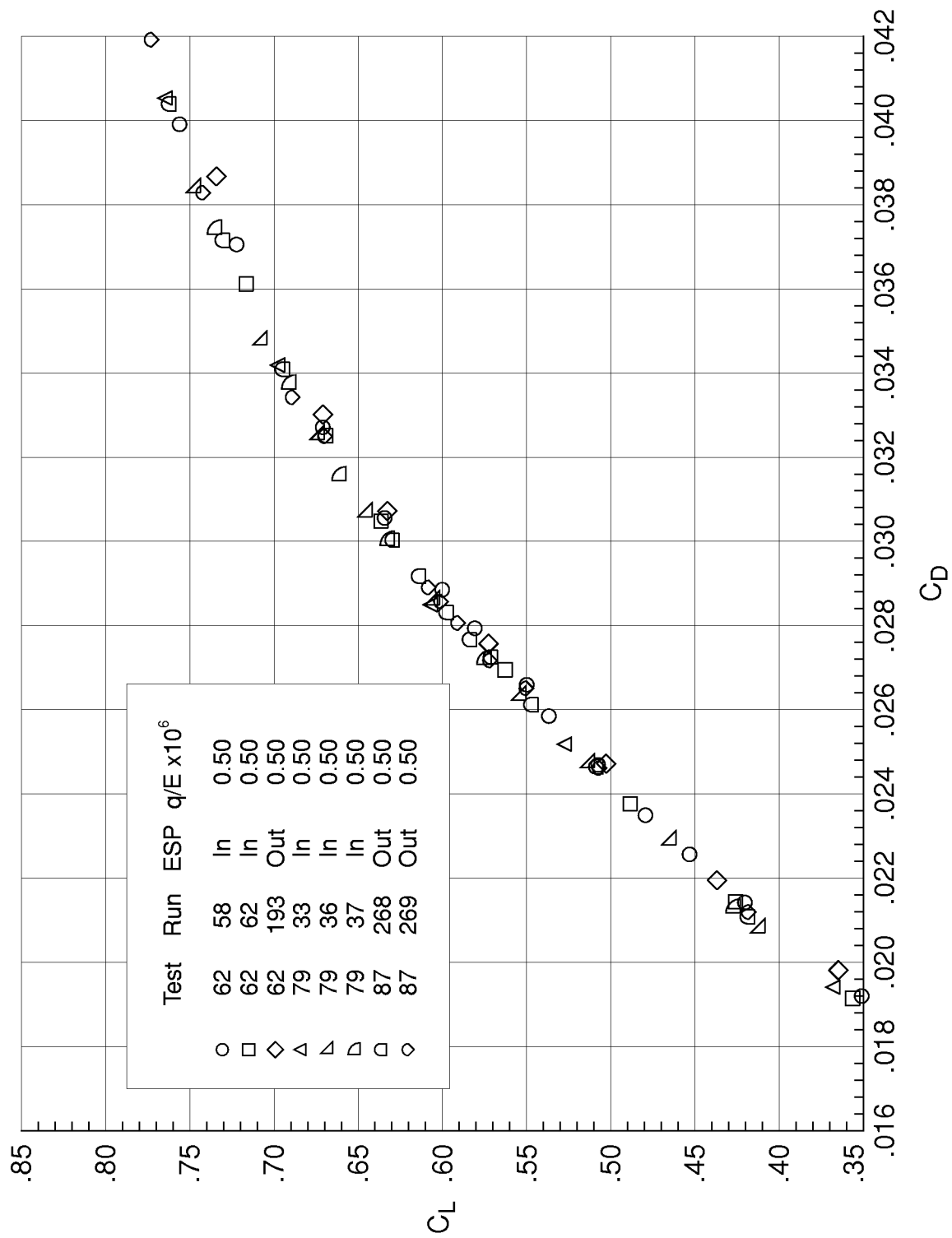
(a) $M_\infty = 0.80$. $R_c = 30. \times 10^6$.

Figure A3. Comparison of the drag coefficient curves from the different tests.



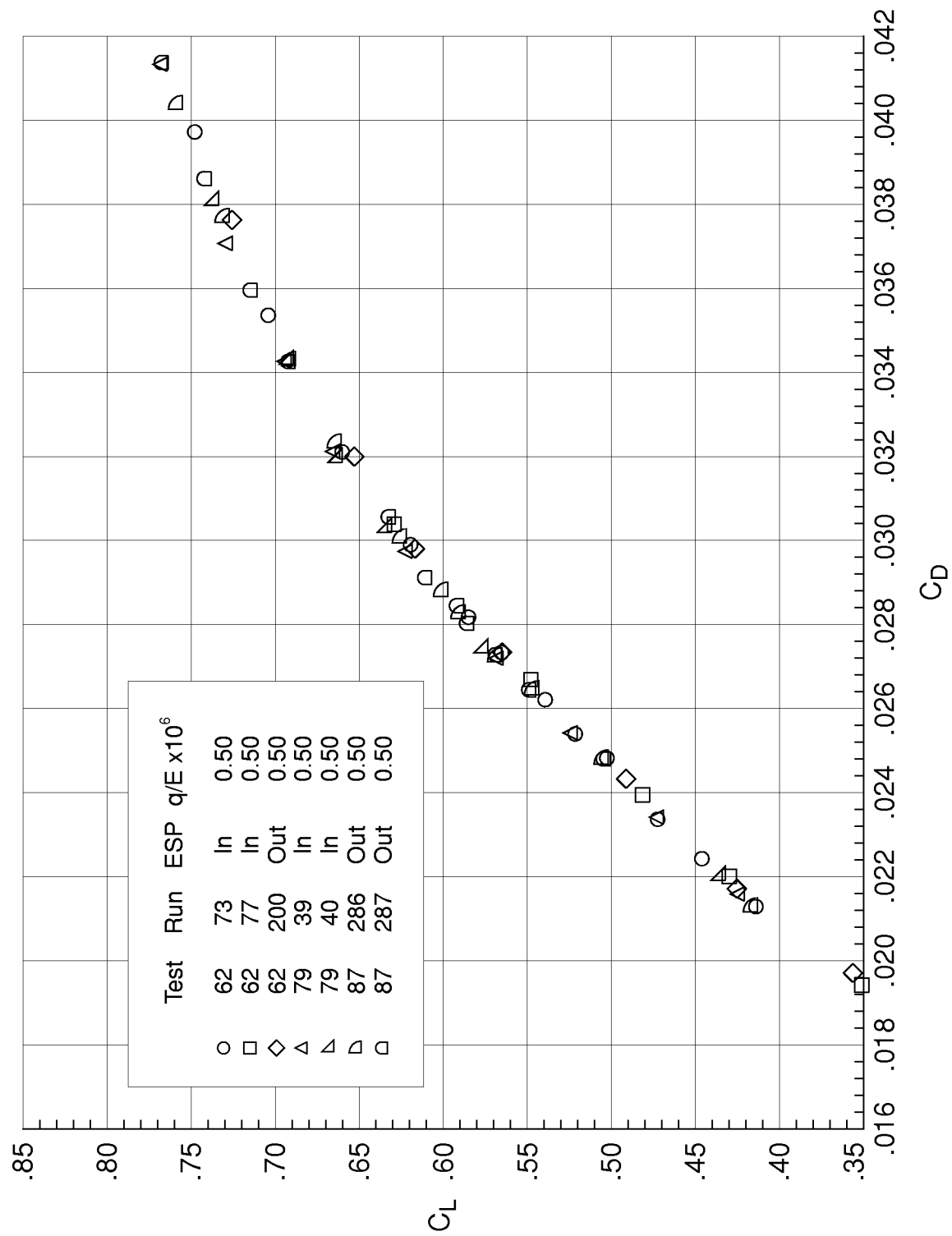
(b) $M_\infty = 0.83$. $R_c = 30. \times 10^6$.

Figure A3. Continued.



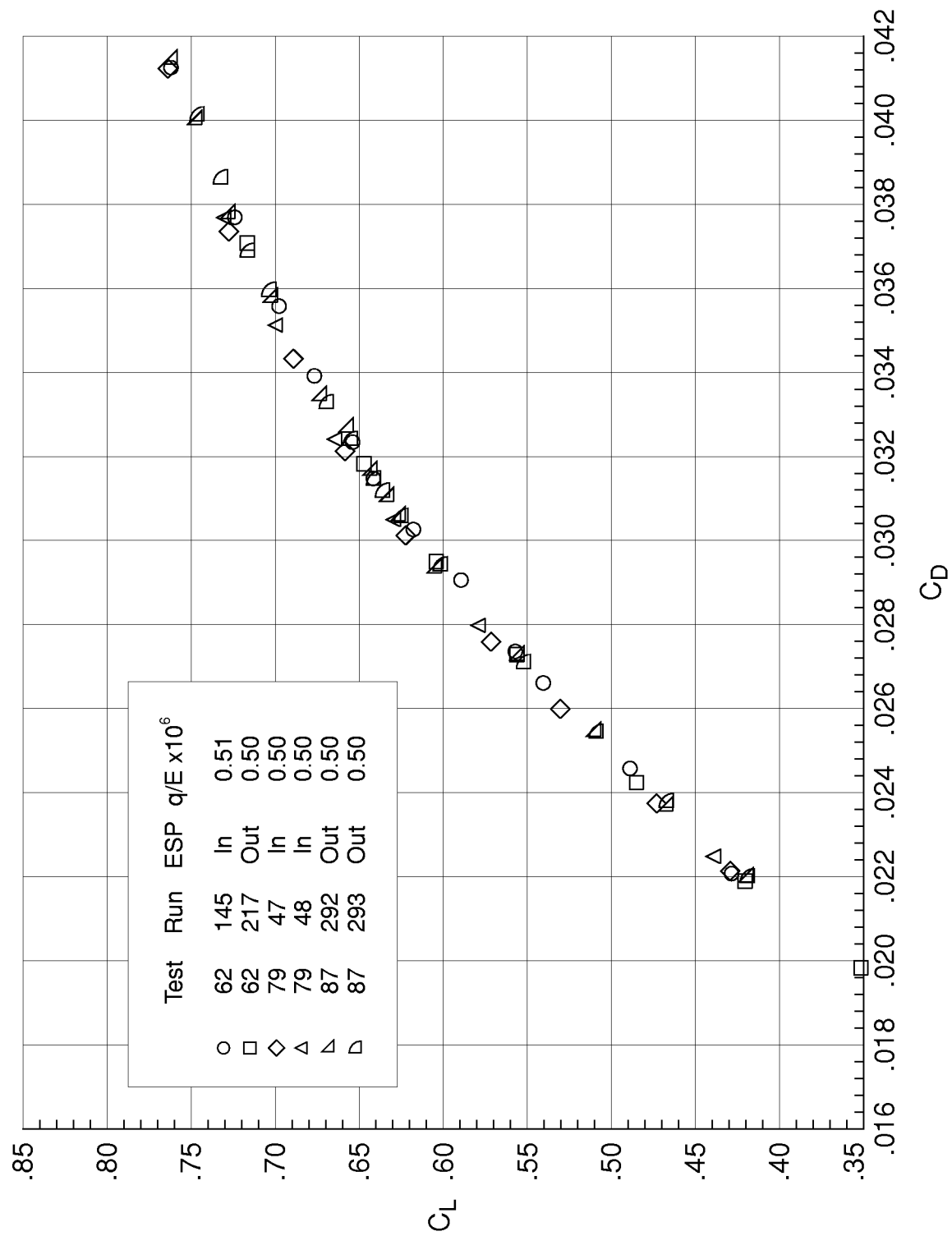
(c) $M_\infty = 0.85$, $R_c = 30. \times 10^6$.

Figure A3. Continued.



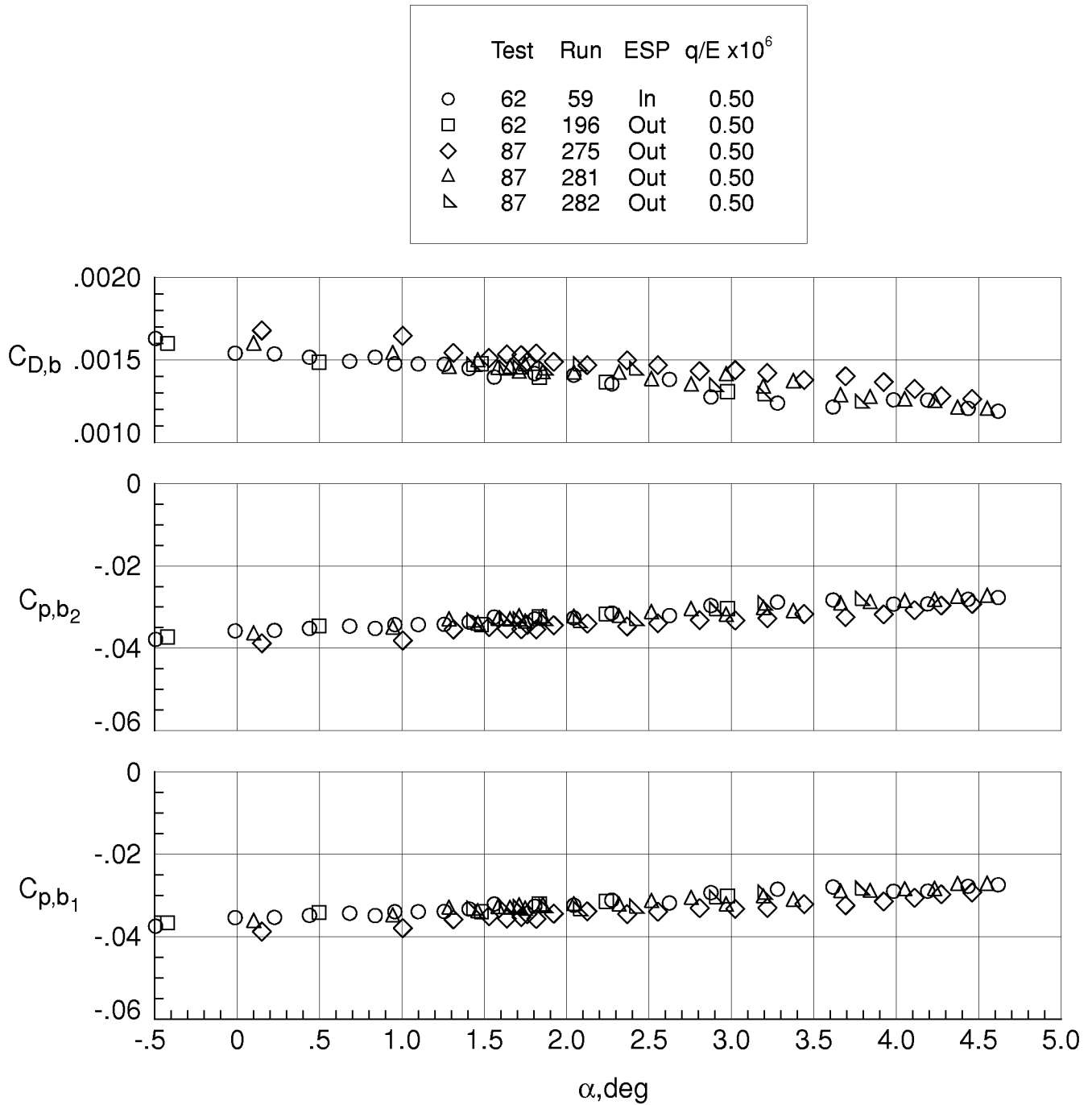
(d) $M_\infty = 0.85$. $R_c = 25 \times 10^6$.

Figure A3. Continued.



(e) $M_\infty = 0.85$. $R_c = 20. \times 10^6$.

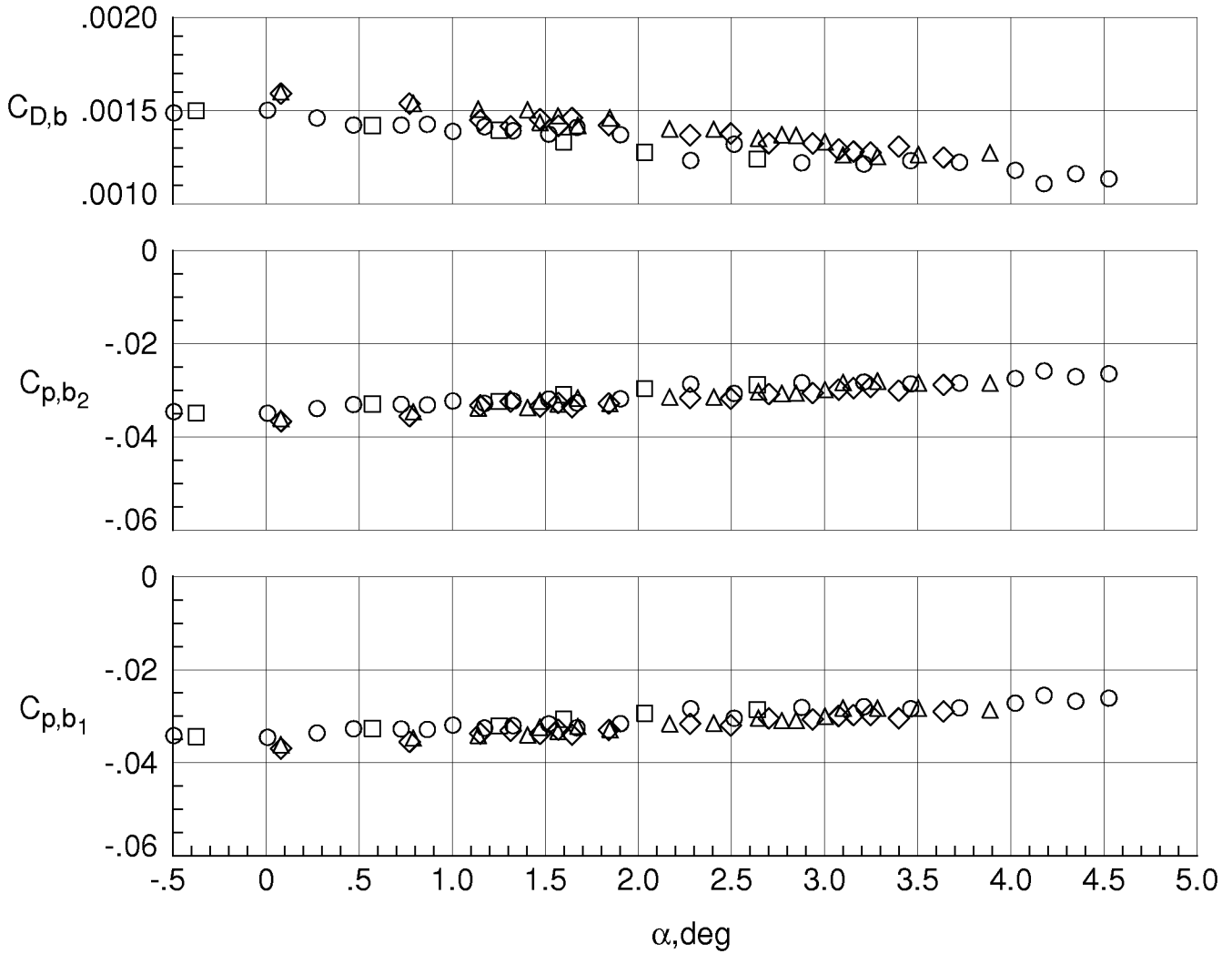
Figure A3. Concluded.



(a) $M_\infty = 0.80$. $R_{\bar{c}} = 30. \times 10^6$.

Figure A4. Comparison of the base-pressure coefficients and drag coefficient correction from the different tests.

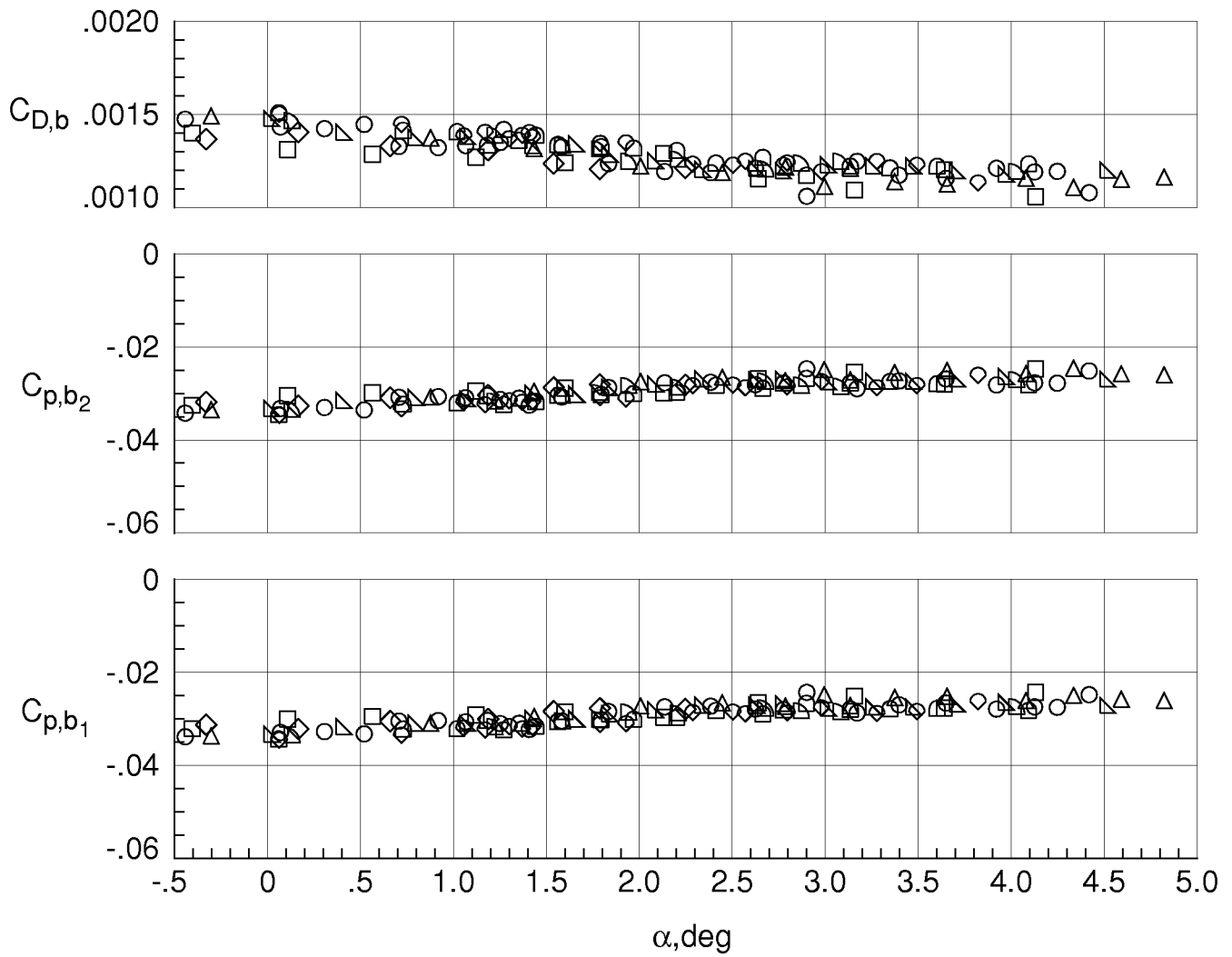
	Test	Run	ESP	$q/E \times 10^6$
○	62	56	In	0.50
□	62	195	Out	0.50
◇	87	273	Out	0.50
△	87	274	Out	0.50



(b) $M_\infty = 0.83$. $R_{\bar{c}} = 30. \times 10^6$.

Figure A4. Continued.

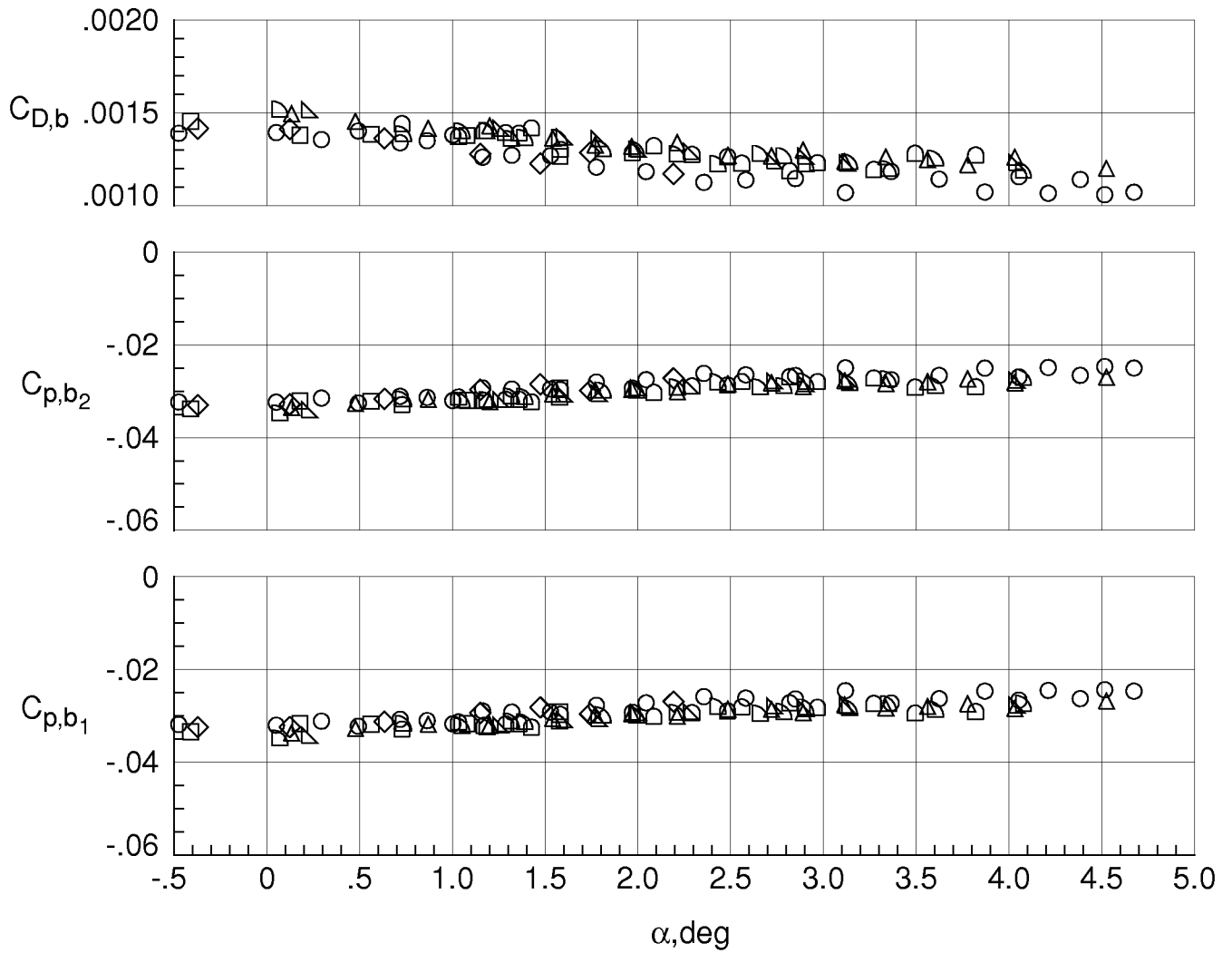
	Test	Run	ESP	$q/E \times 10^6$
○	62	58	In	0.50
□	62	62	In	0.50
◇	62	193	Out	0.50
△	79	33	In	0.50
▴	79	36	In	0.50
▷	79	37	In	0.50
◻	87	268	Out	0.50
◊	87	269	Out	0.50



(c) $M_\infty = 0.85$. $R_c = 30. \times 10^6$.

Figure A4. Continued.

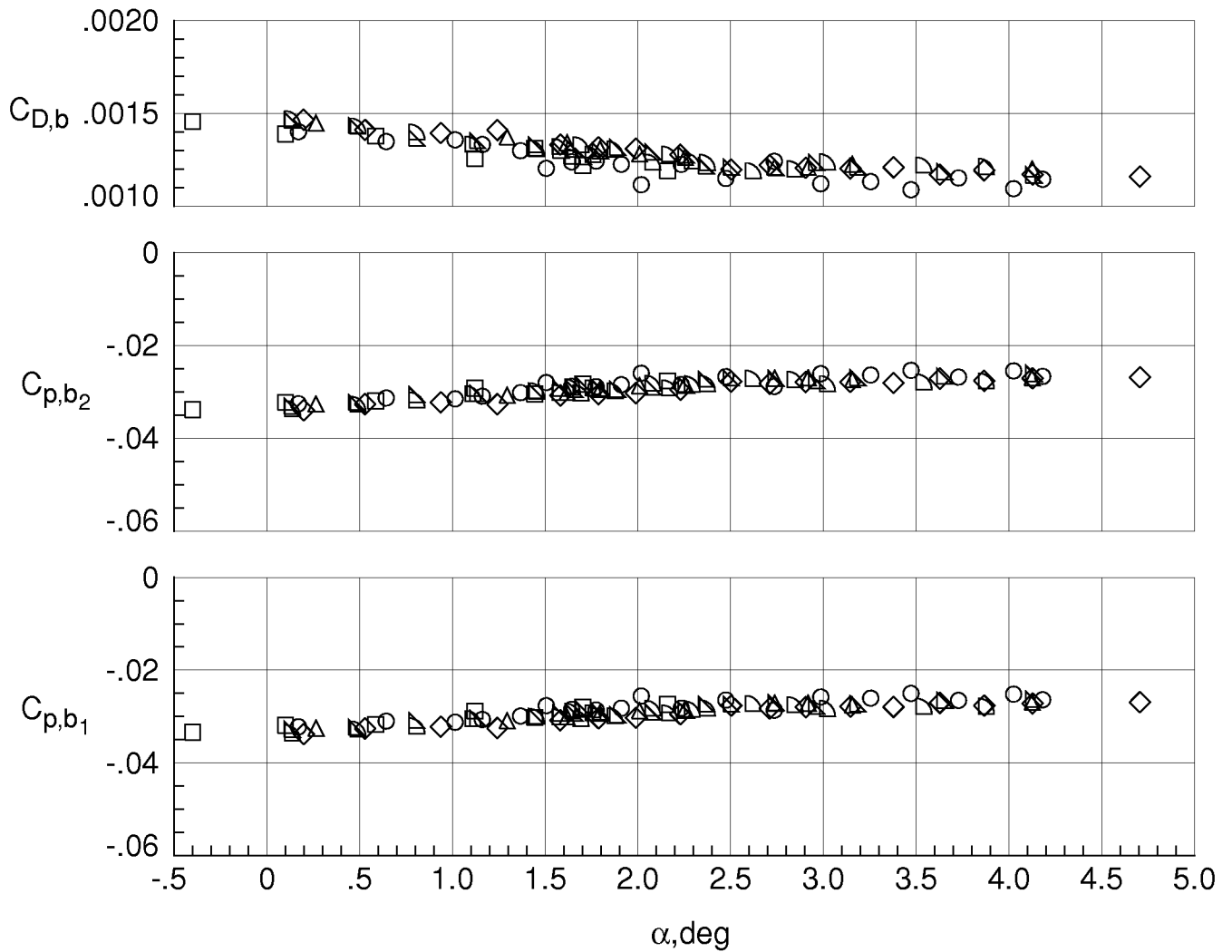
	Test	Run	ESP	$q/E \times 10^6$
○	62	73	In	0.50
□	62	77	In	0.50
◇	62	200	Out	0.50
△	79	39	In	0.50
▴	79	40	In	0.50
▾	87	286	Out	0.50
◻	87	287	Out	0.50



(d) $M_\infty = 0.85$. $R_{\bar{c}} = 25$. $\times 10^6$.

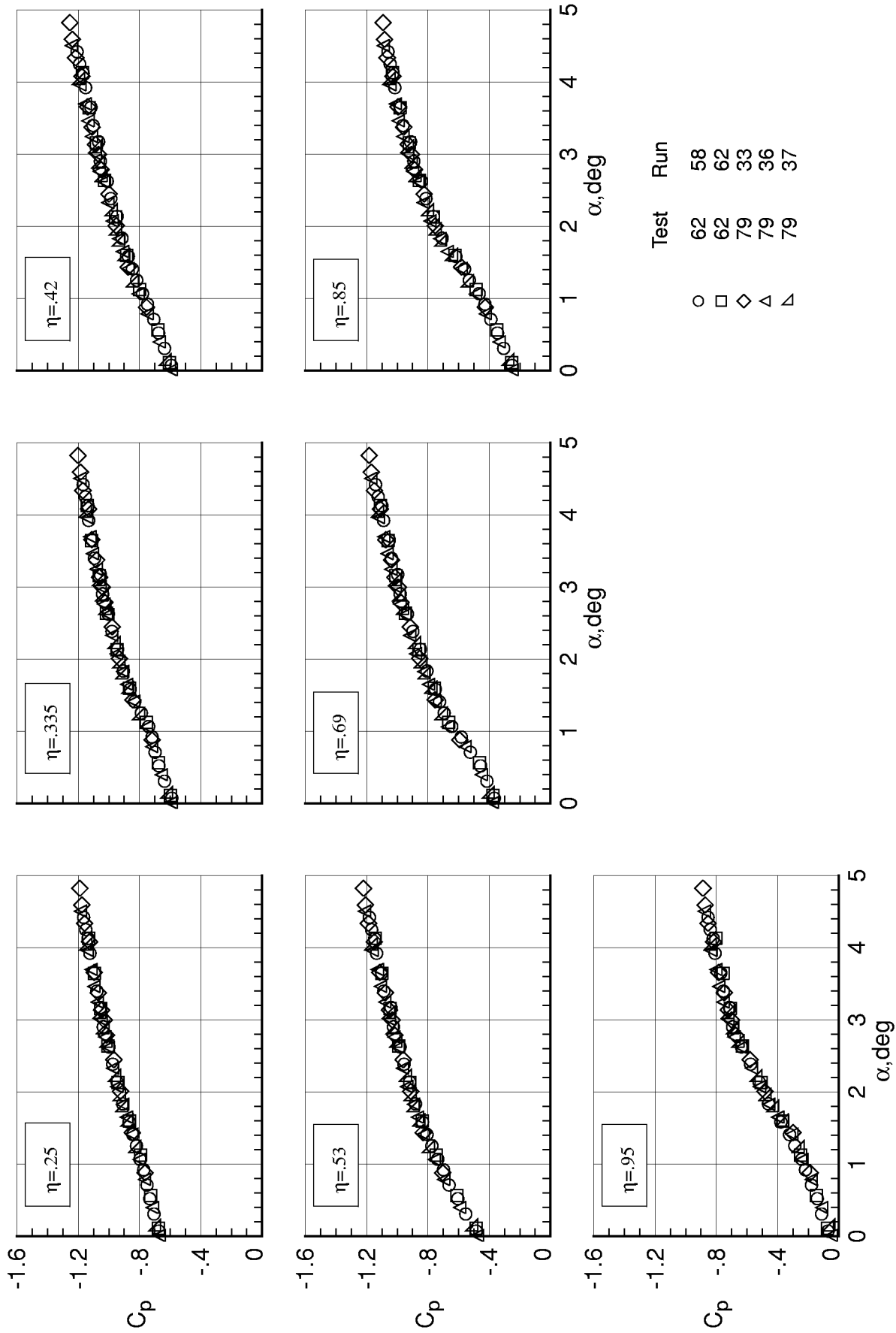
Figure A4. Continued.

	Test	Run	ESP	$q/E \times 10^6$
○	62	145	In	0.51
□	62	217	Out	0.50
◇	79	47	In	0.50
△	79	48	In	0.50
▵	87	292	Out	0.50
▾	87	293	Out	0.50



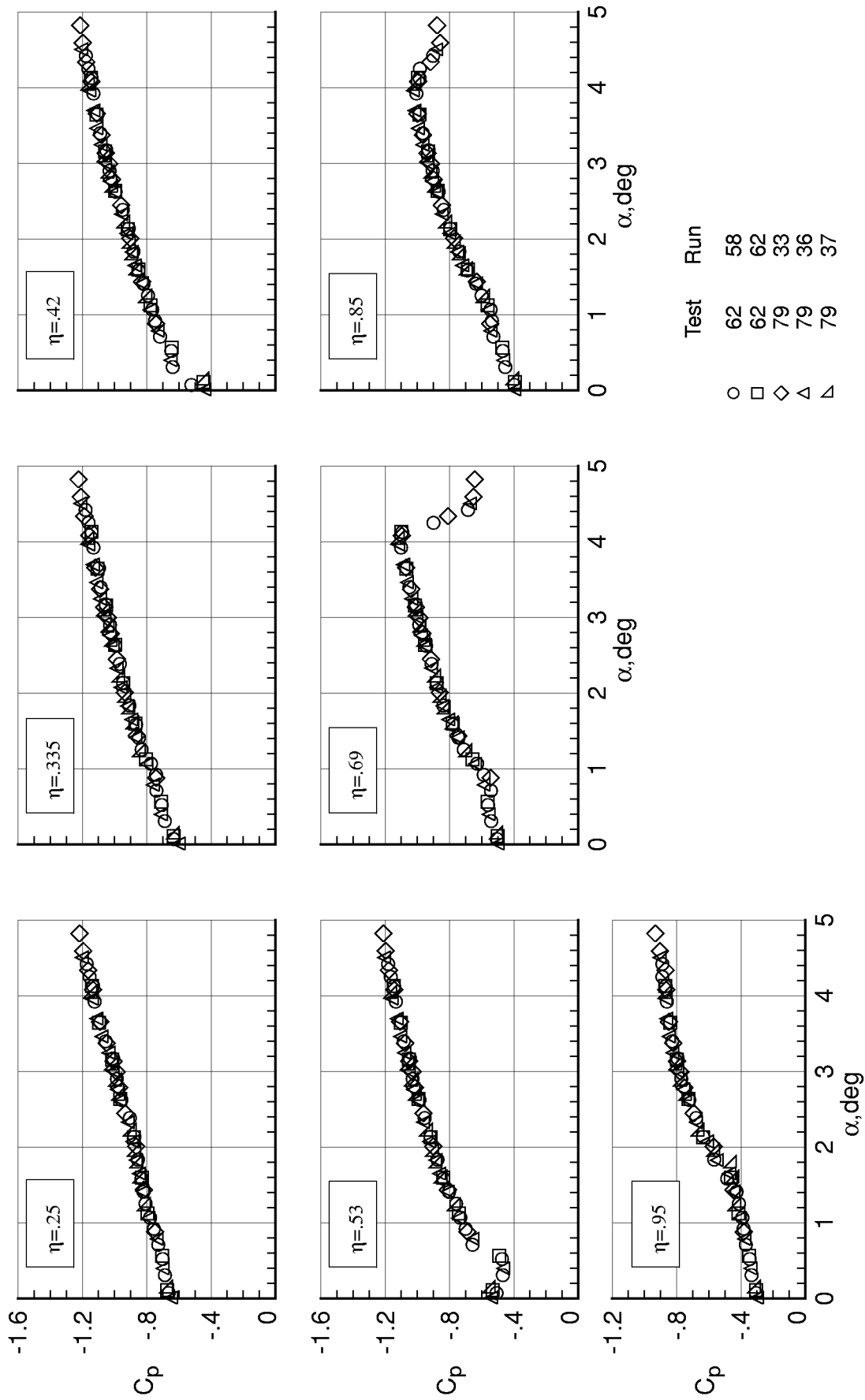
(e) $M_\infty = 0.85$. $R_{\bar{c}} = 20. \times 10^6$.

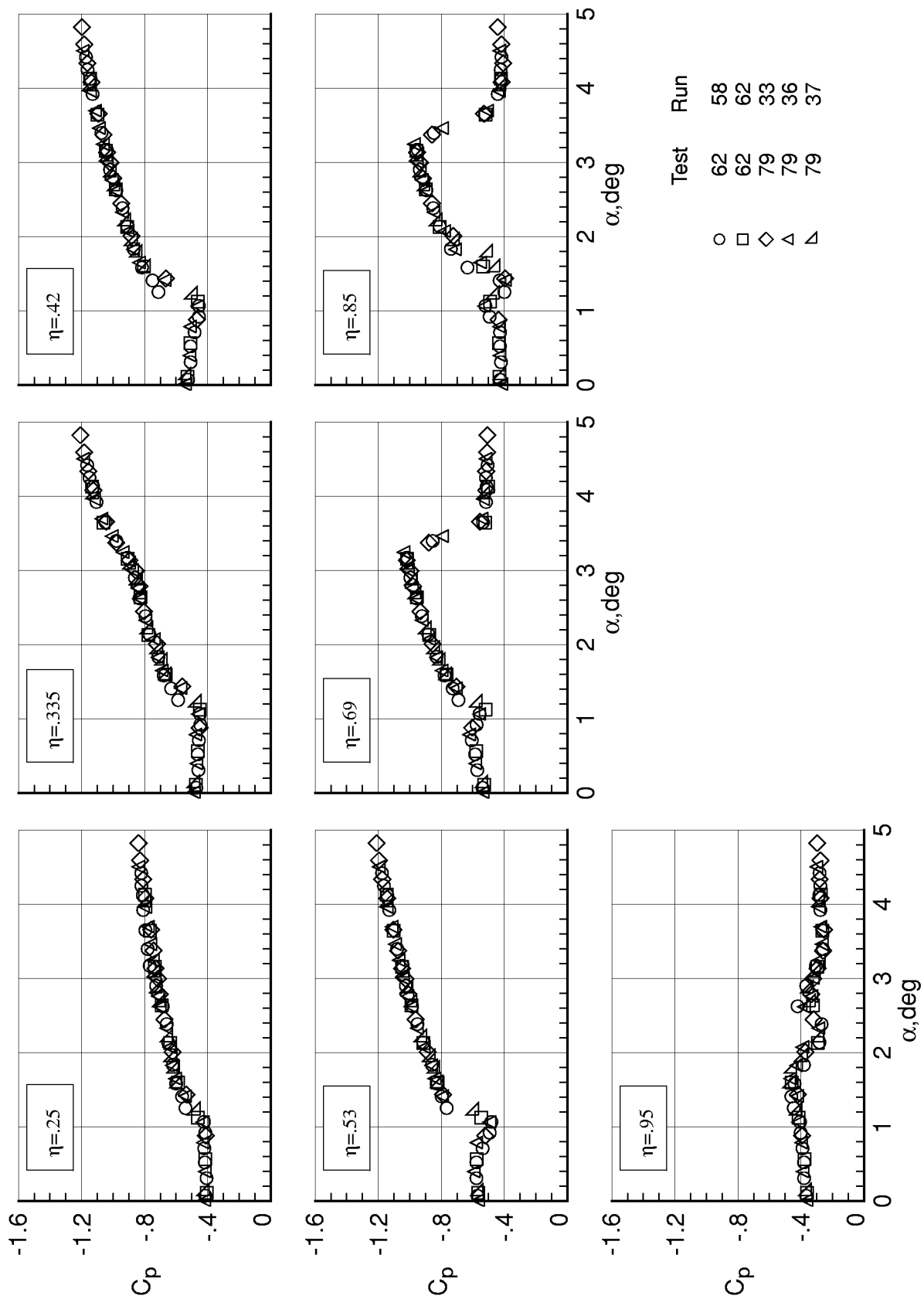
Figure A4. Concluded.



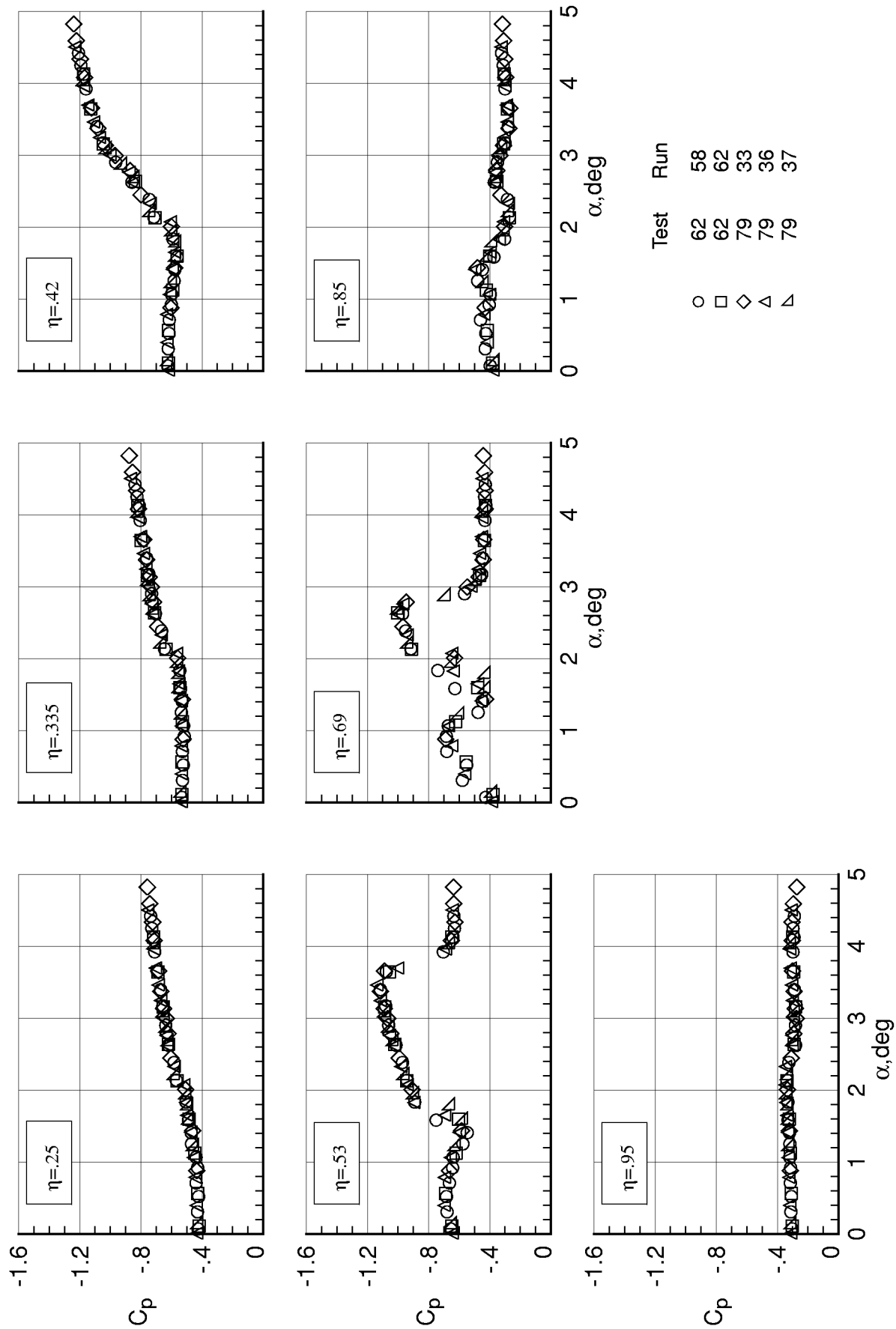
(a) $x/c = 0.05$.

Figure A5. Comparison of the pressure coefficients from the different tests. $M_\infty = 0.85$. $R_c = 30 \cdot 10^6$.

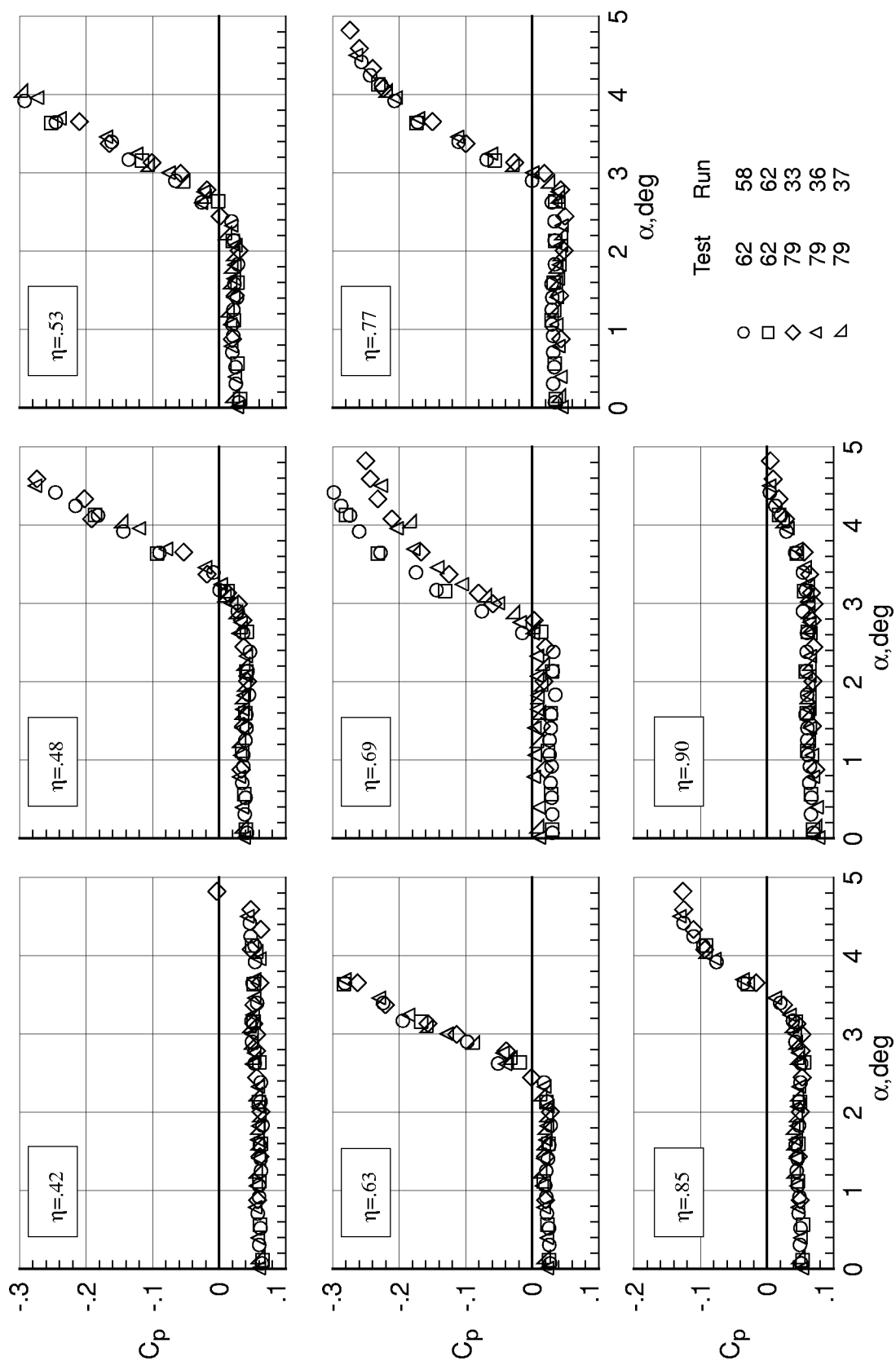




(c) $x/c = 0.45$.
Figure A5. Continued.



(d) $x/c = 0.62$.
Figure A5. Continued.



References

1. Wahls, R. A.; Adcock, J. B.; Witkowski, D. P.; and Wright, F. L.: *A Longitudinal Aerodynamic Data Repeatability Study for a Commercial Transport Model Test in the National Transonic Facility*. NASA TP-3522, 1995.
2. Al-Saadi, Jassim A.: *Effect of Reynolds Number, Boundary-Layer Transition, and Aeroelasticity on Longitudinal Aerodynamic Characteristics of a Subsonic Transport Wing*. NASA TP-3655, 1997.
3. Fuller, D. E.; Gloss, B. B.; and Nystrom, D.: *Guide to Users of the National Transonic Facility*. NASA TM-83124, 1981.
4. Igoe, William B.: *Analysis of Fluctuating Static Pressure Measurements in the National Transonic Facility*. NASA TP-3475, 1996. (Also available as *Analysis of Fluctuating Static Pressure Measurements of a Large High Reynolds Number Transonic Cryogenic Wind Tunnel*. Ph.D Dissertation, George Washington University, May 1993.)
5. Henne, P. A.: Innovation With Computational Aerodynamics—The Divergent Trailing-Edge Airfoil. *Applied Computational Aerodynamics*, AIAA, 1990, pp. 221–261.
6. Jacobs, Peter F.; and Gloss, Blair B.: *Longitudinal Aerodynamic Characteristics of a Subsonic, Energy-Efficient Transport Configuration in the National Transonic Facility*. NASA TP-2922, 1989.
7. Finley, Tom D.; and Tcheng, Ping: Model Attitude Measurements at NASA Langley Research Center. AIAA-92-0763, Jan. 1992.
8. Foster, Jean M.; and Adcock, Jerry B.: *User's Guide for the National Transonic Facility Data System*. NASA TM-100511, 1987
9. Coleman, Hugh W; and Steele, W. Glenn: *Experimentation and Uncertainty Analysis for Engineers*. John Wiley and Sons, 1989.

TABLES

Table 1. Description of the Model.

Body:	
maximum diameter.	5.75 in.
length	60.5 in.
Wing:	
aspect ratio	9.0
taper ratio	0.3
sweep, quarter chord	35.0°
dihedral.	3.0°
mean aerodynamic chord	7.485 in.
span	61.428 in.
reference area	419.262 in ²

Table 2. Balance Full-Scale Load and Worst Case Accuracy as a Percent of Full-Scale.

Component	Item	Balance/Test/Calibration-Date		
		NTF101B Test 62 2/5/93	NTF113C Test 79 12/8/94	NTF113A Test 87 9/6/95
Normal	Full scale	6500 lb	6500 lb	6500 lb
	Accuracy	±0.16%	±0.09%	±0.08%
Axial	Full scale	700 lb	400 lb	400 lb
	Accuracy	±0.21%	±0.40%	±0.49%
Pitch	Full scale	13,000 in-lb	13,000 in-lb	13,000 in-lb
	Accuracy	±0.15%	±0.08%	±0.06%

Table 3. Estimated Error Bands (worst case) for the Force and Moment Coefficients near the Design Lift Coefficient. $q/E = 0.5 \times 10^{-6}$.

Lift Coefficient			
M_∞	Test 62	Test 79	Test 87
0.80	±0.0019	*	±0.0010
0.83	±0.0019	*	±0.0010
0.85	±0.0019	±0.0011	±0.0010
Drag Coefficient			
M_∞	Test 62	Test 79	Test 87
0.80	±0.00034	*	±0.00040
0.83	±0.00034	*	±0.00040
0.85	±0.00034	±0.00035	±0.00040
Pitching-Moment Coefficient			
M_∞	Test 62	Test 79	Test 87
0.80	±0.0007	*	±0.0004
0.83	±0.0007	*	±0.0004
0.85	±0.0007	±0.0004	±0.0004
Pressure Coefficient			
M_∞	Test 62	Test 79	Test 87
0.85	±0.005	±0.005	*
* denotes no data at this test condition			

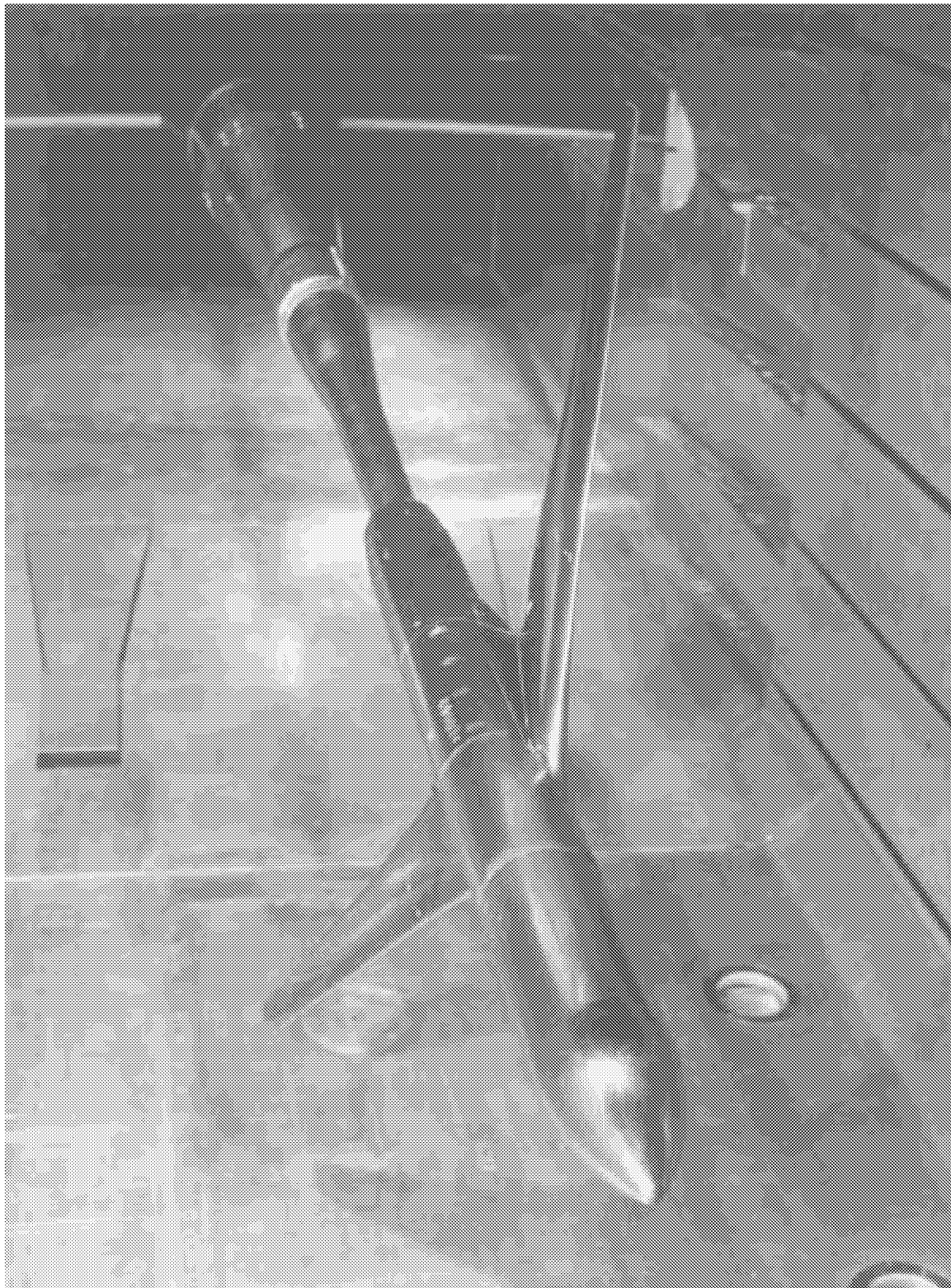
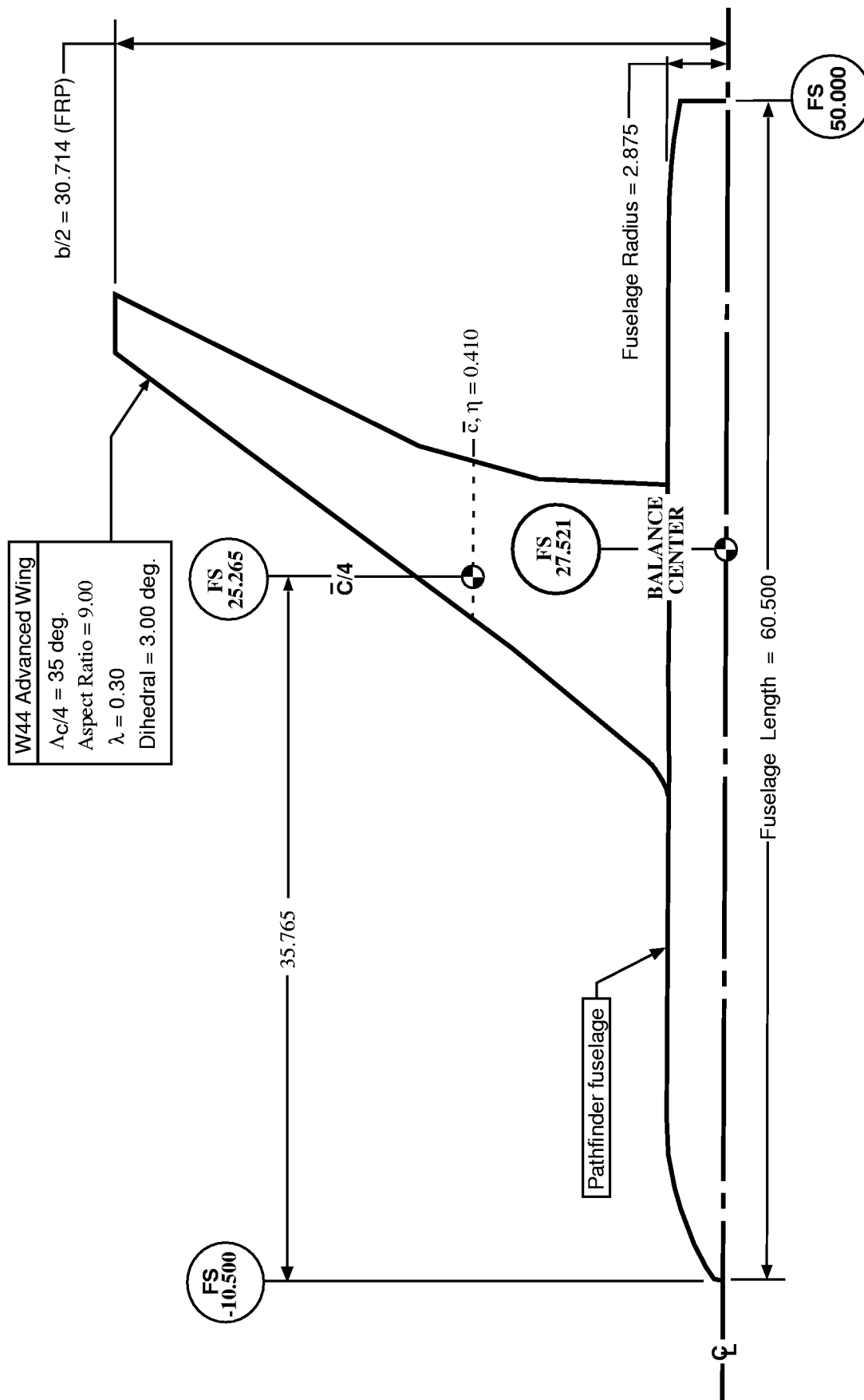


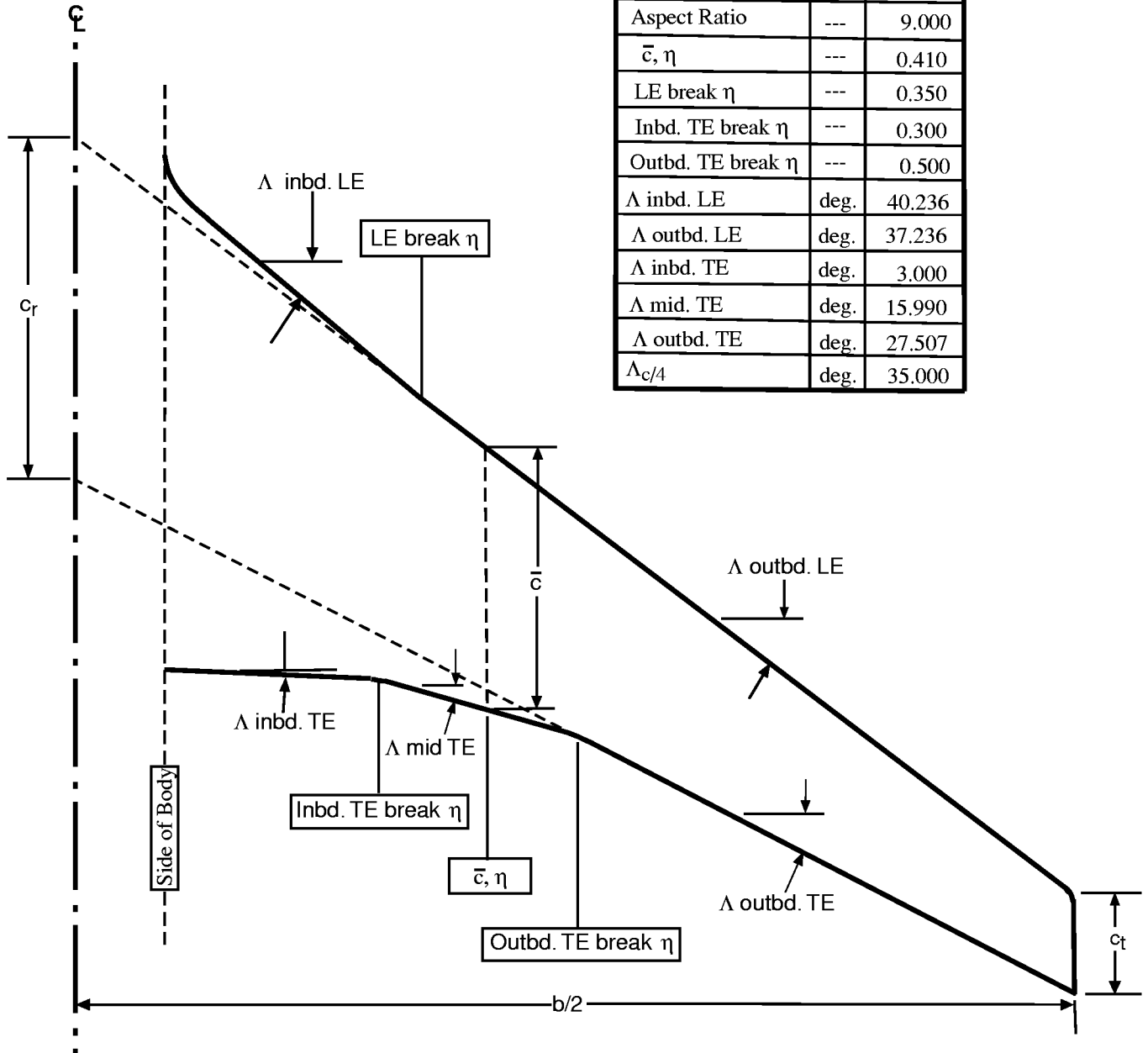
Figure 1. Photograph of the model installed in the National Transonic Facility test section



(a) Plan view of model showing general arrangement.

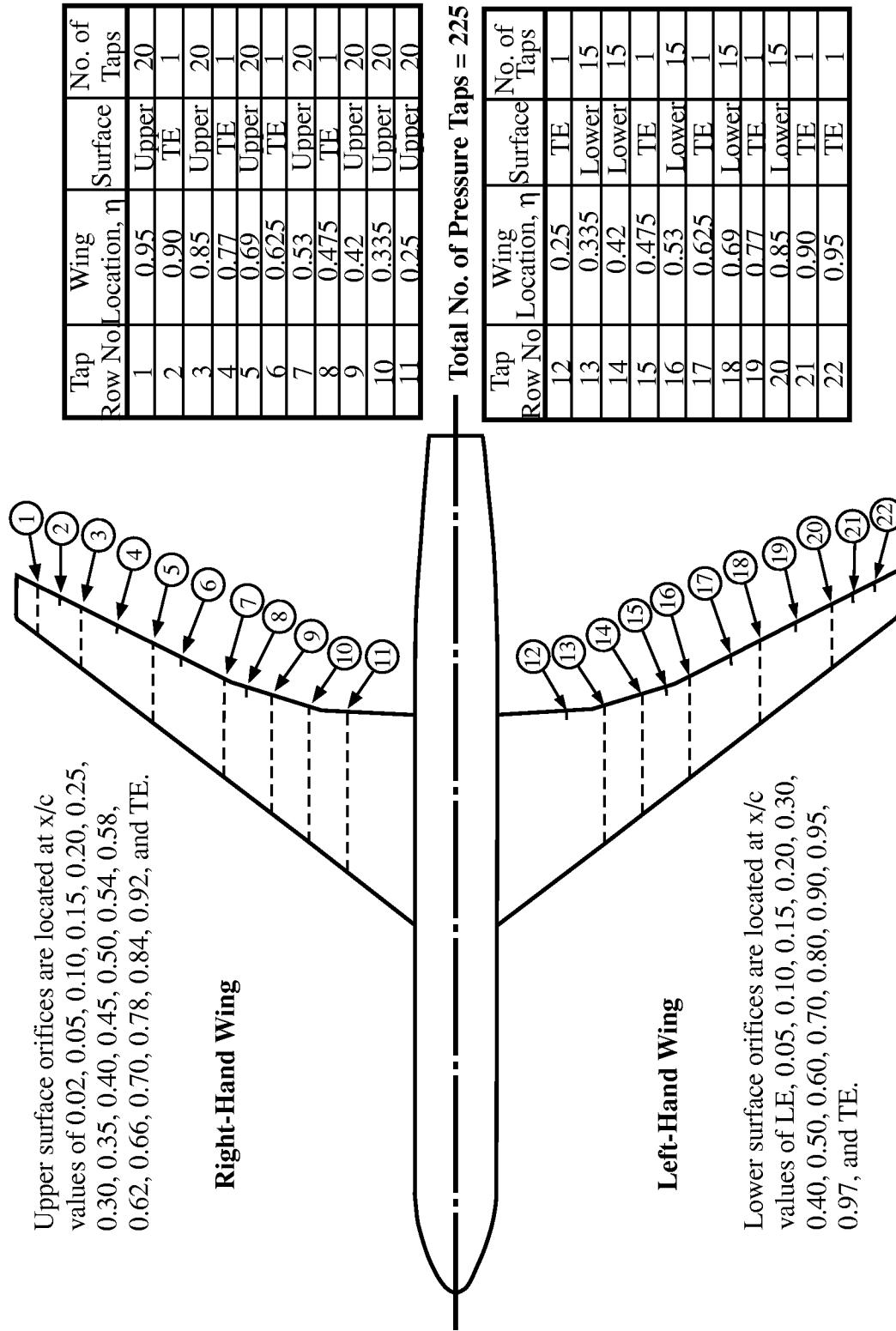
Figure 2. 2.426% scale W44 wing/NTF model arrangement, important wing dimensions, and pressure orifice locations. All linear dimensions are in inches.

FRP parameter	Unit	Value
Reference Area (Trapezoidal)	in. ²	419.262
b	in.	61.428
\bar{c} (mean)	in.	7.485
c_r	in.	10.500
c_t	in.	3.150
λ	---	0.300
Aspect Ratio	---	9.000
\bar{c}, η	---	0.410
LE break η	---	0.350
Inbd. TE break η	---	0.300
Outbd. TE break η	---	0.500
Λ inbd. LE	deg.	40.236
Λ outbd. LE	deg.	37.236
Λ inbd. TE	deg.	3.000
Λ mid. TE	deg.	15.990
Λ outbd. TE	deg.	27.507
$\Lambda_{c/4}$	deg.	35.000



(b) Details of the W44 wing geometry.

Figure 2. Continued.



(c) Static pressure instrumentation locations on the wing.

Figure 2. Concluded.

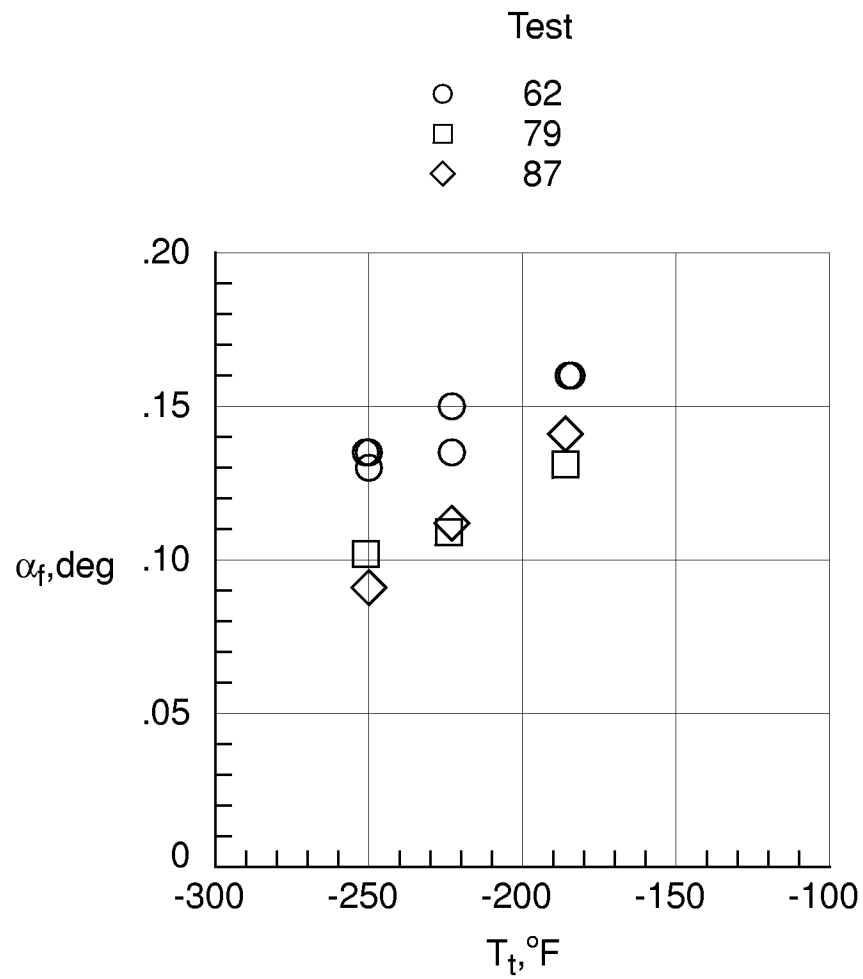
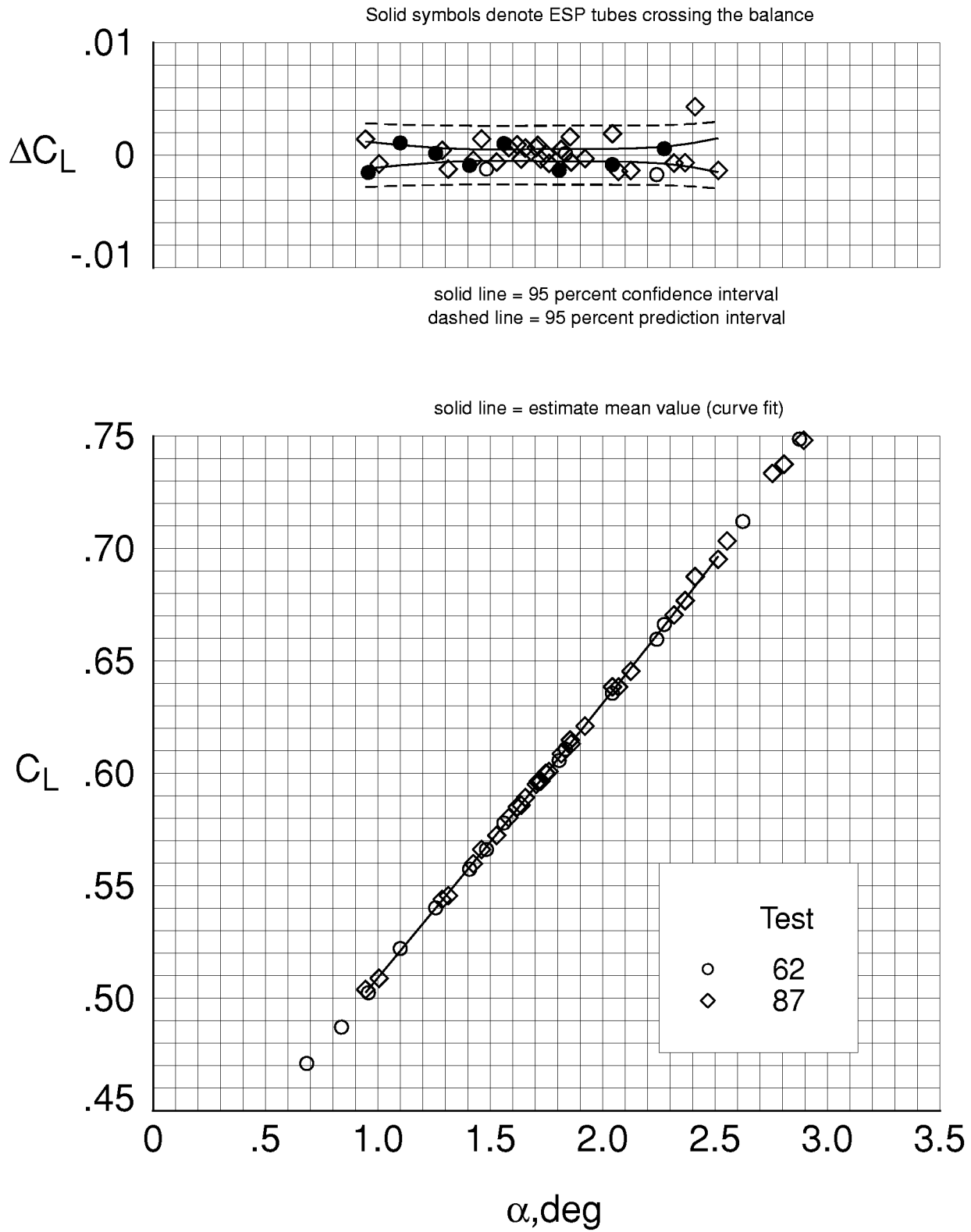
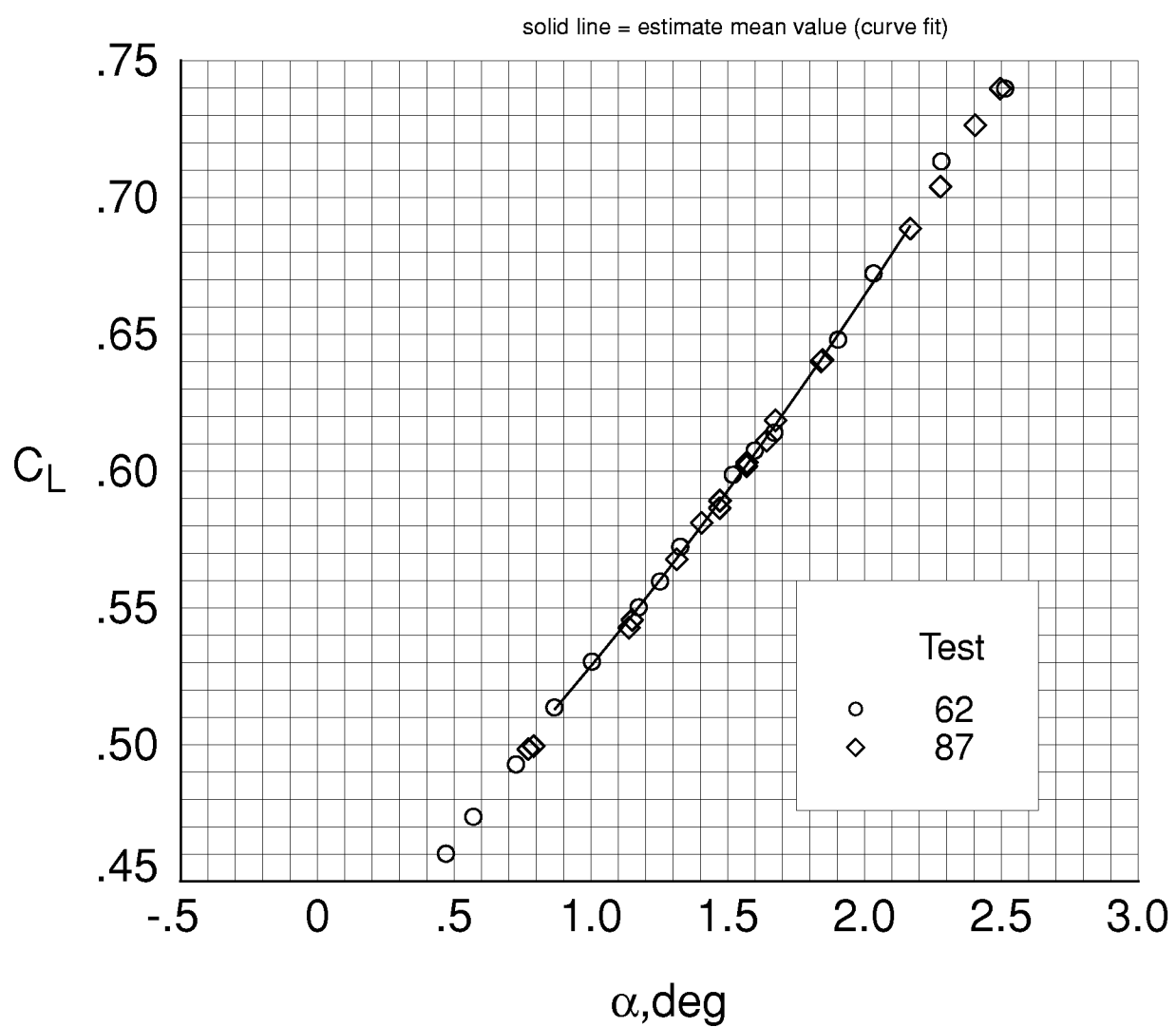
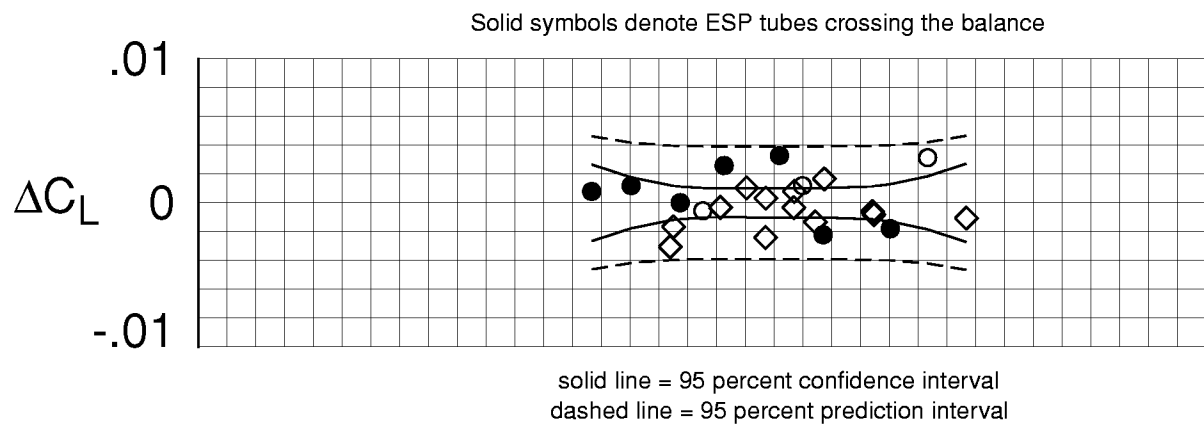


Figure 3. Calculated flow angularity from the different tests. $M_\infty = 0.85$

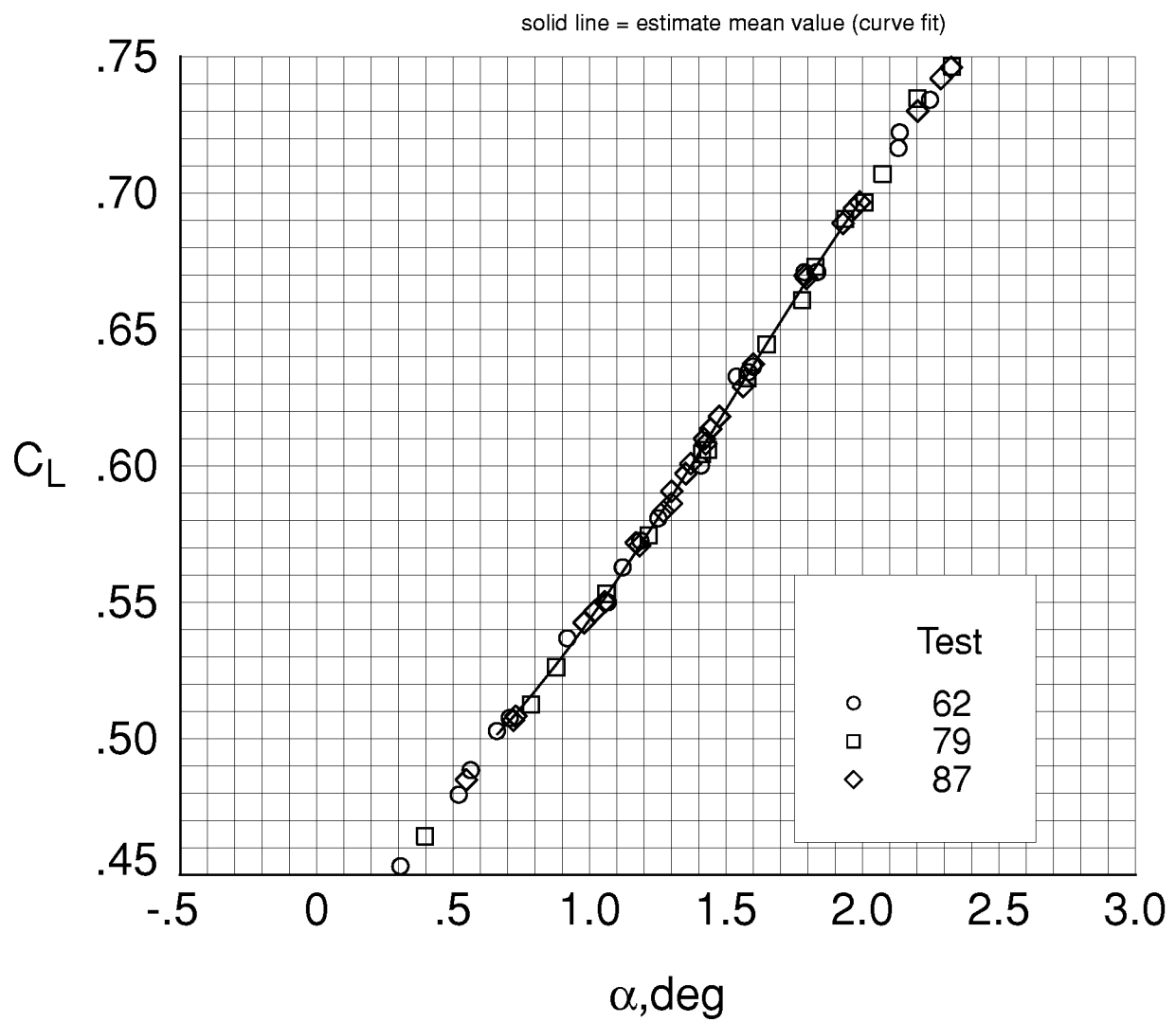
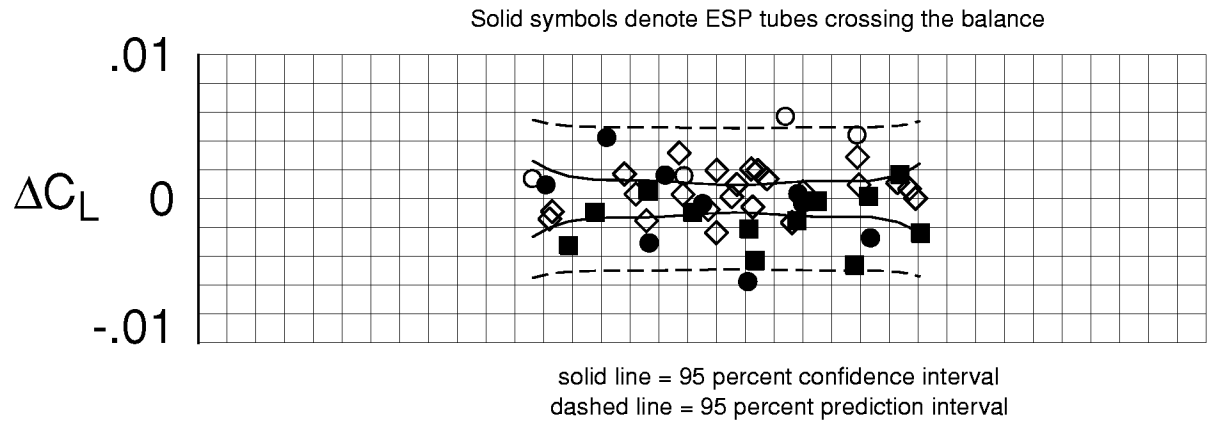


(a) $M_\infty = 0.80$, $R_c^- = 30. \times 10^6$.
Figure 4. Analysis of repeated C_L data.



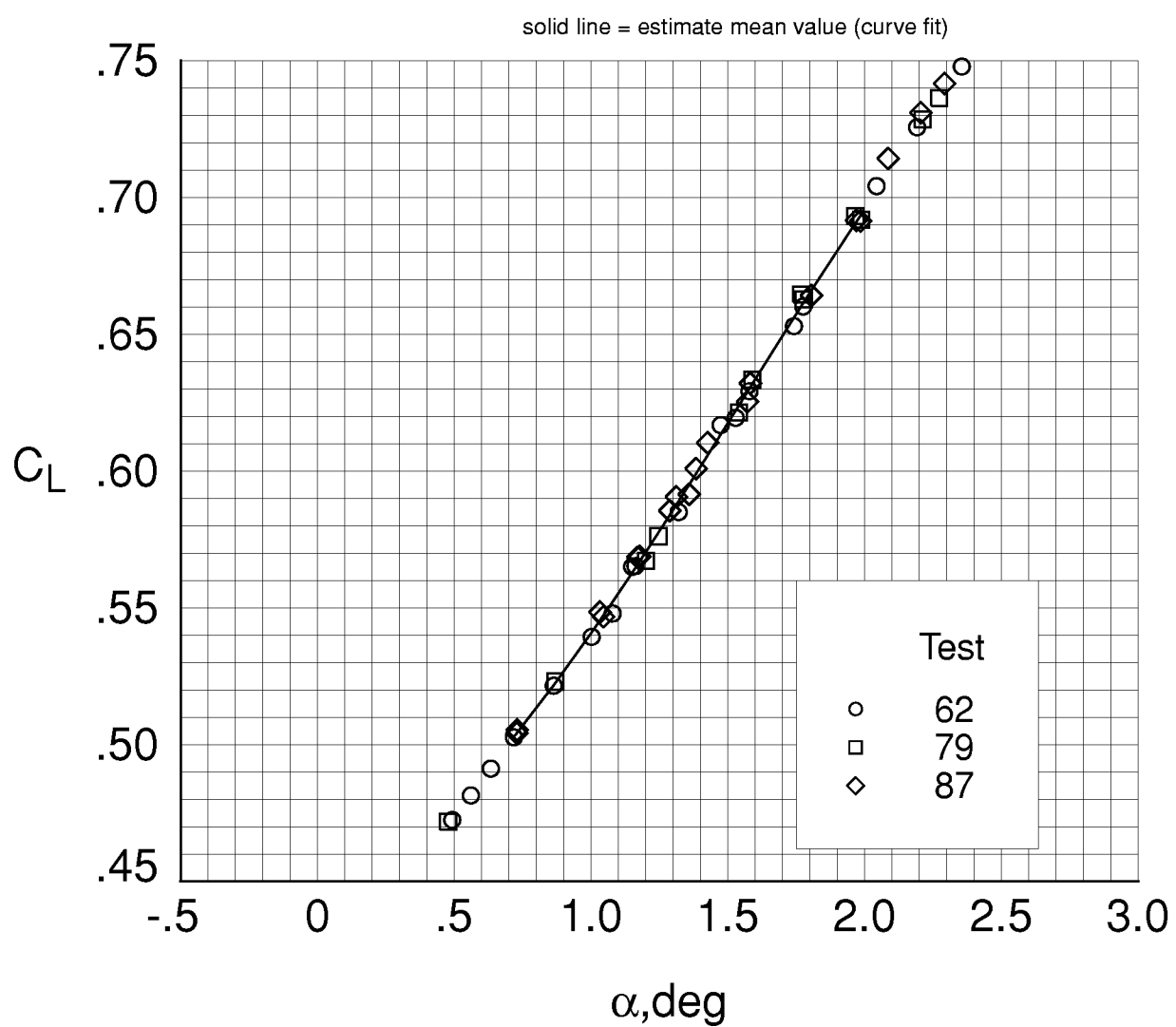
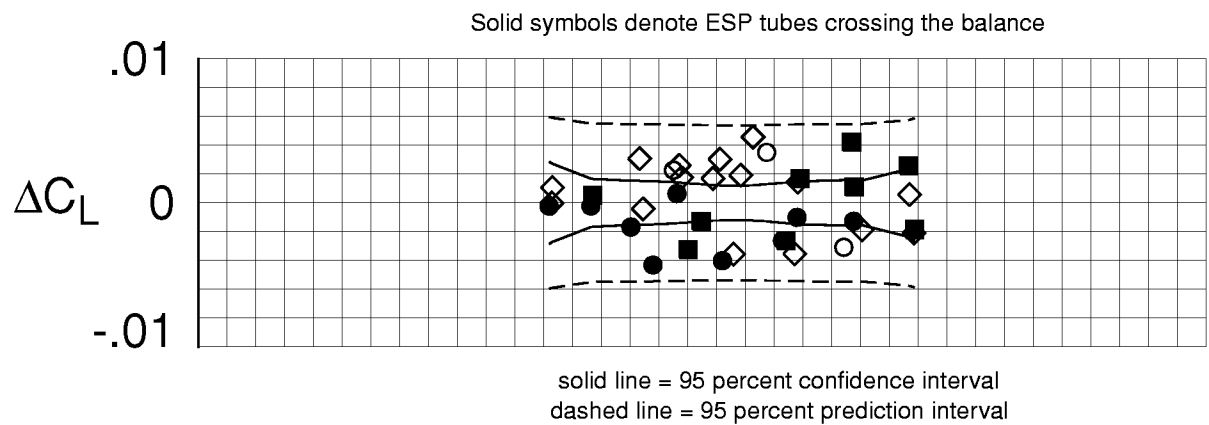
(b) $M_\infty = 0.83$, $R_c^- = 30. \times 10^6$.

Figure 4. Continued.



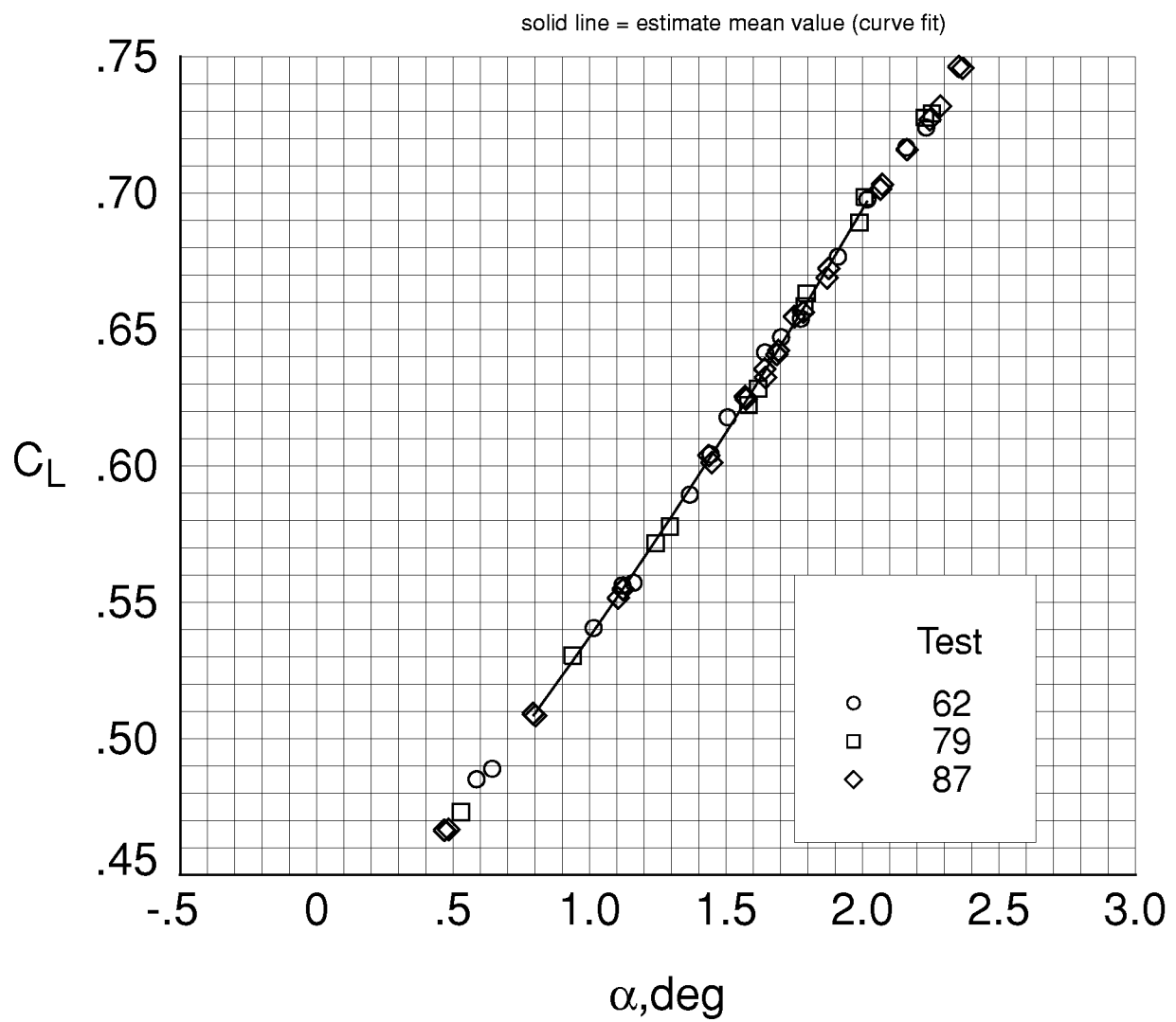
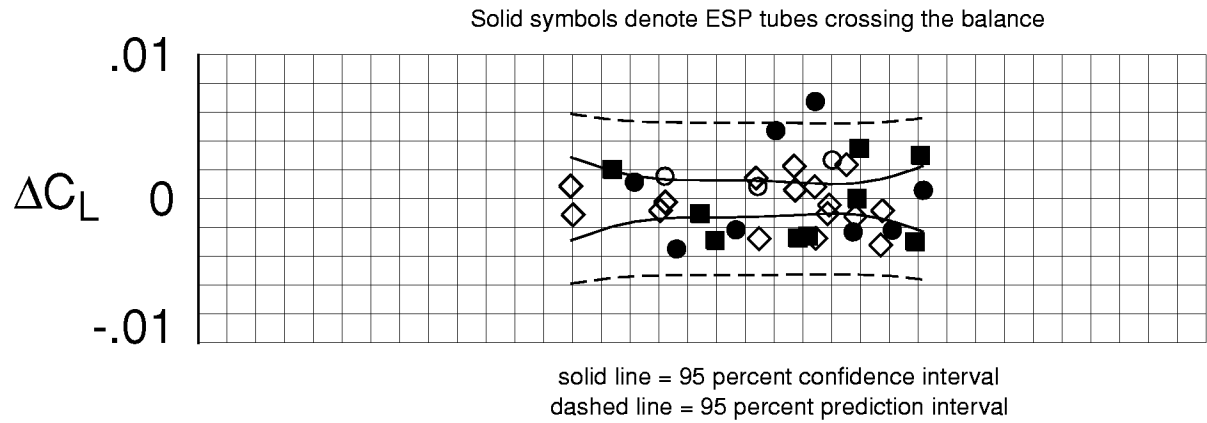
(c) $M_\infty = 0.85$, $R_C^- = 30. \times 10^6$.

Figure 4. Continued.



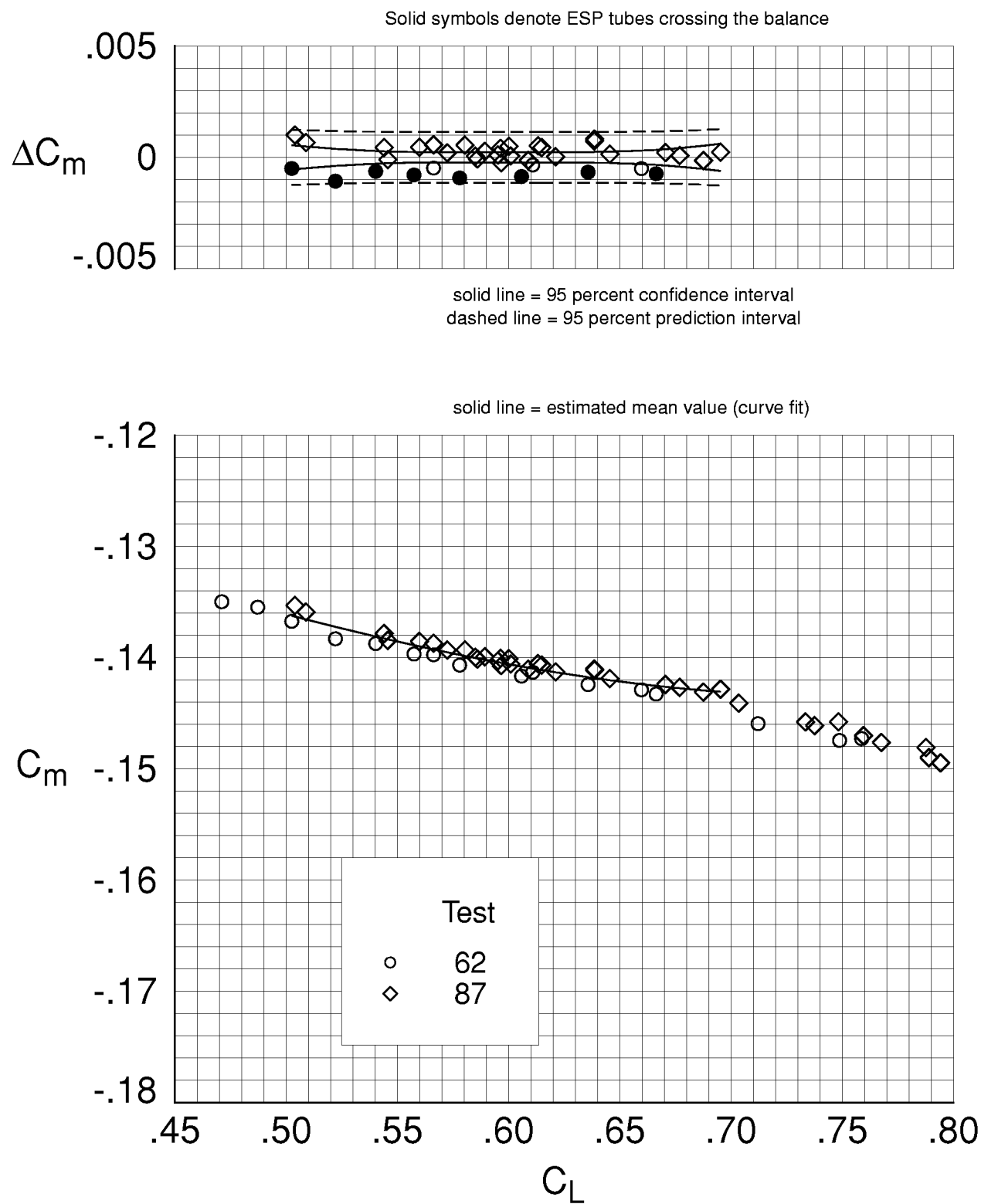
(d) $M_\infty = 0.85$, $R_{\bar{C}} = 25. \times 10^6$.

Figure 4. Continued.

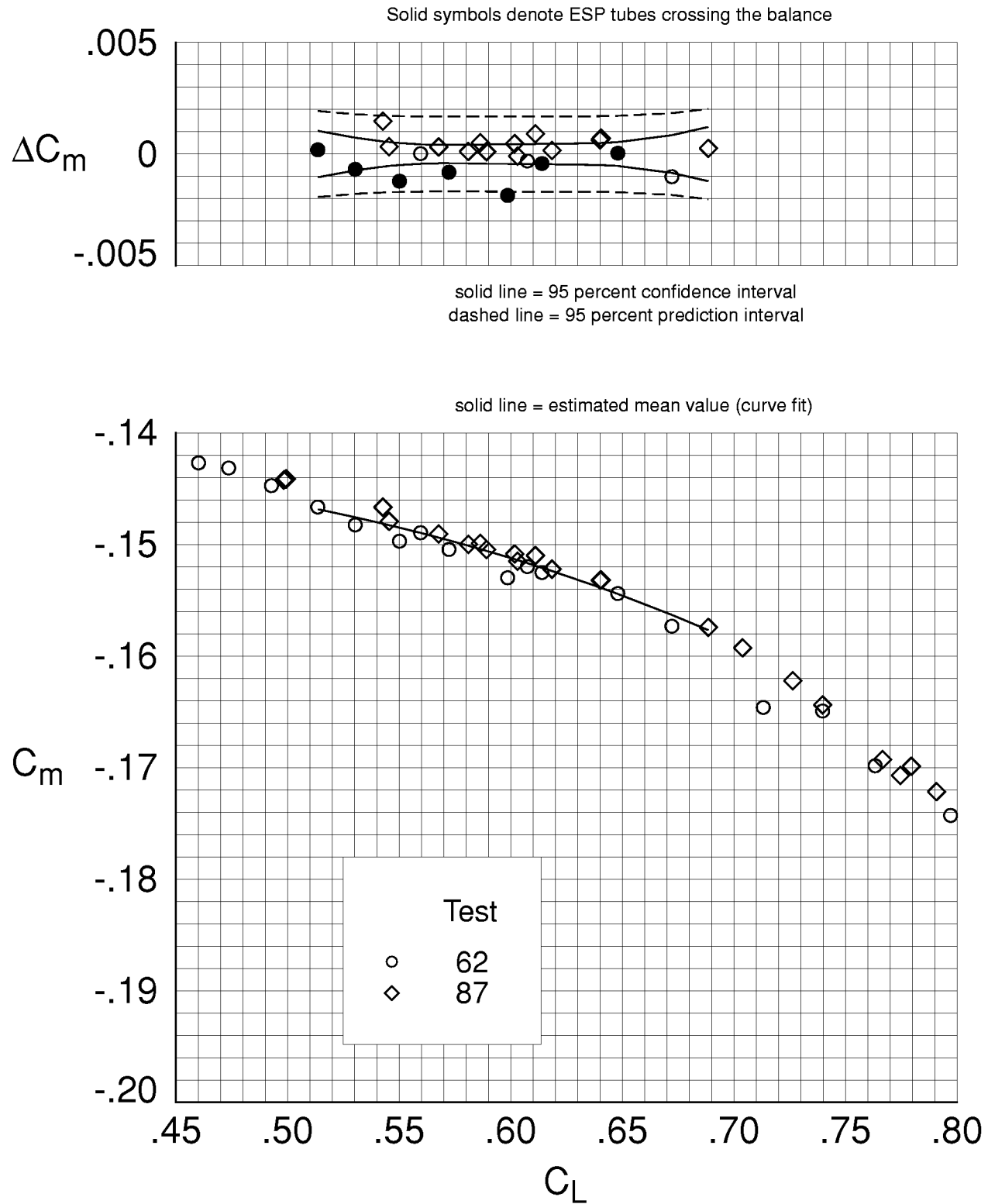


(e) $M_\infty = 0.85$, $R_c^- = 20. \times 10^6$.

Figure 4. Concluded.

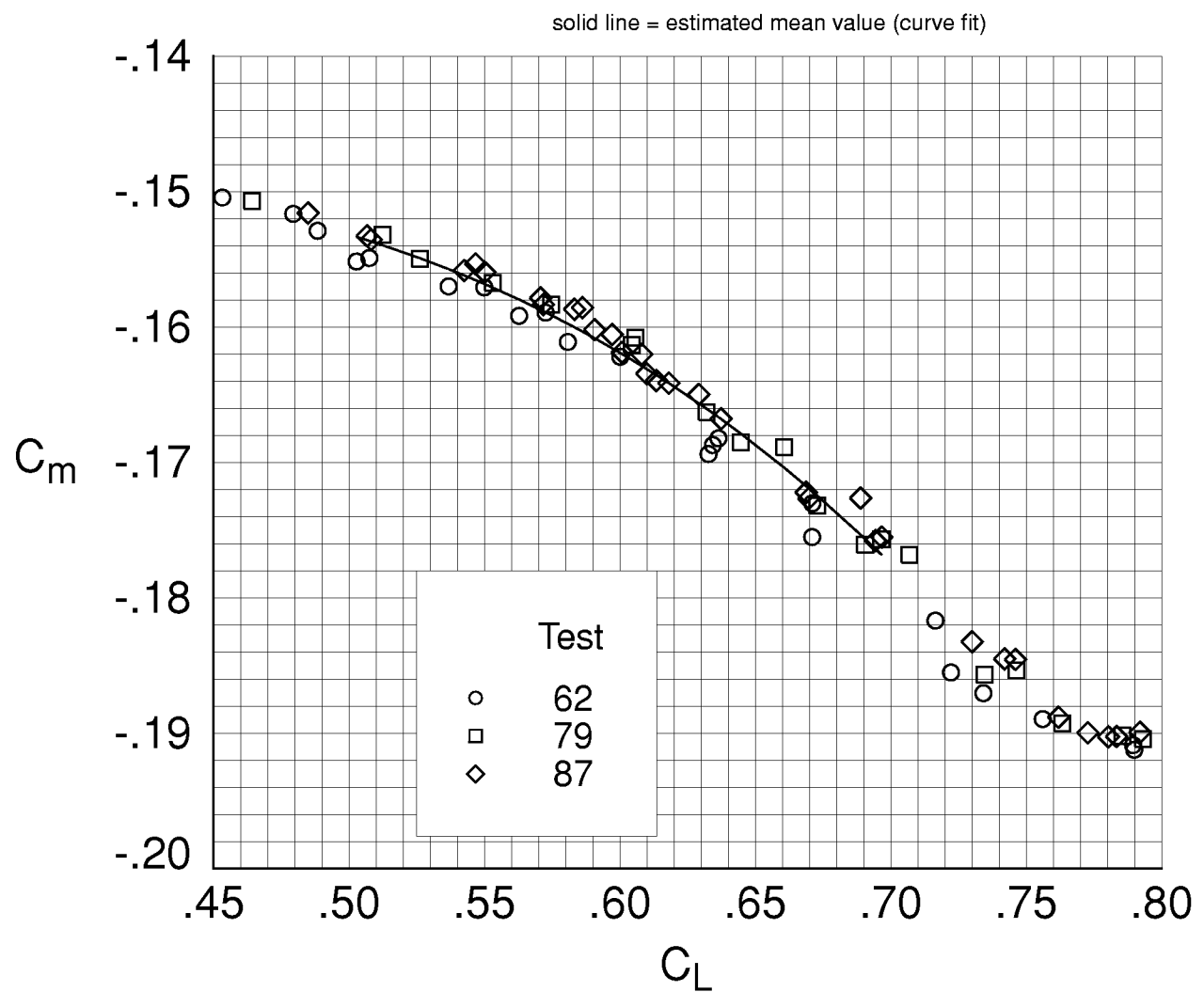
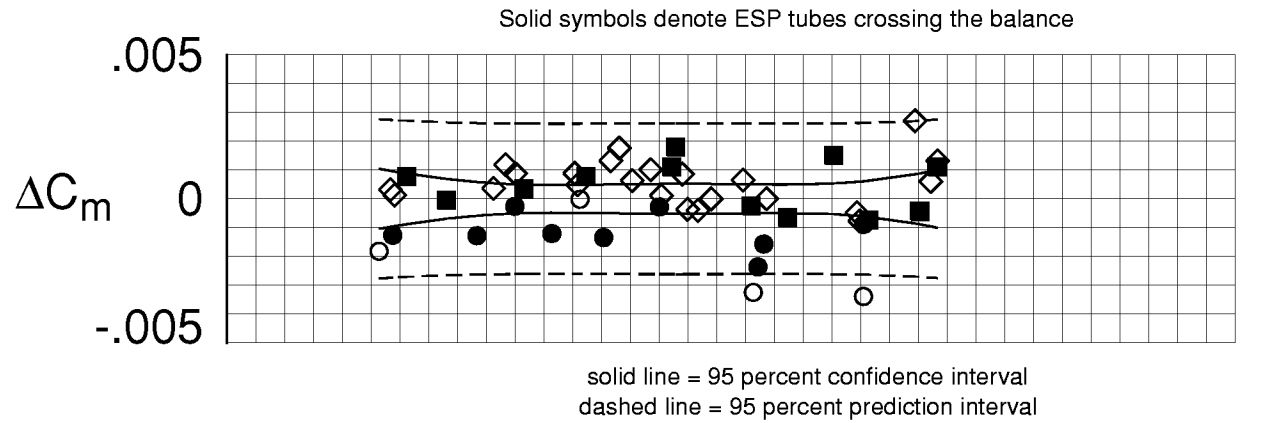


(a) $M_\infty = 0.80$, $R_c^- = 30. \times 10^6$.
Figure 5. Analysis of repeated C_m data.



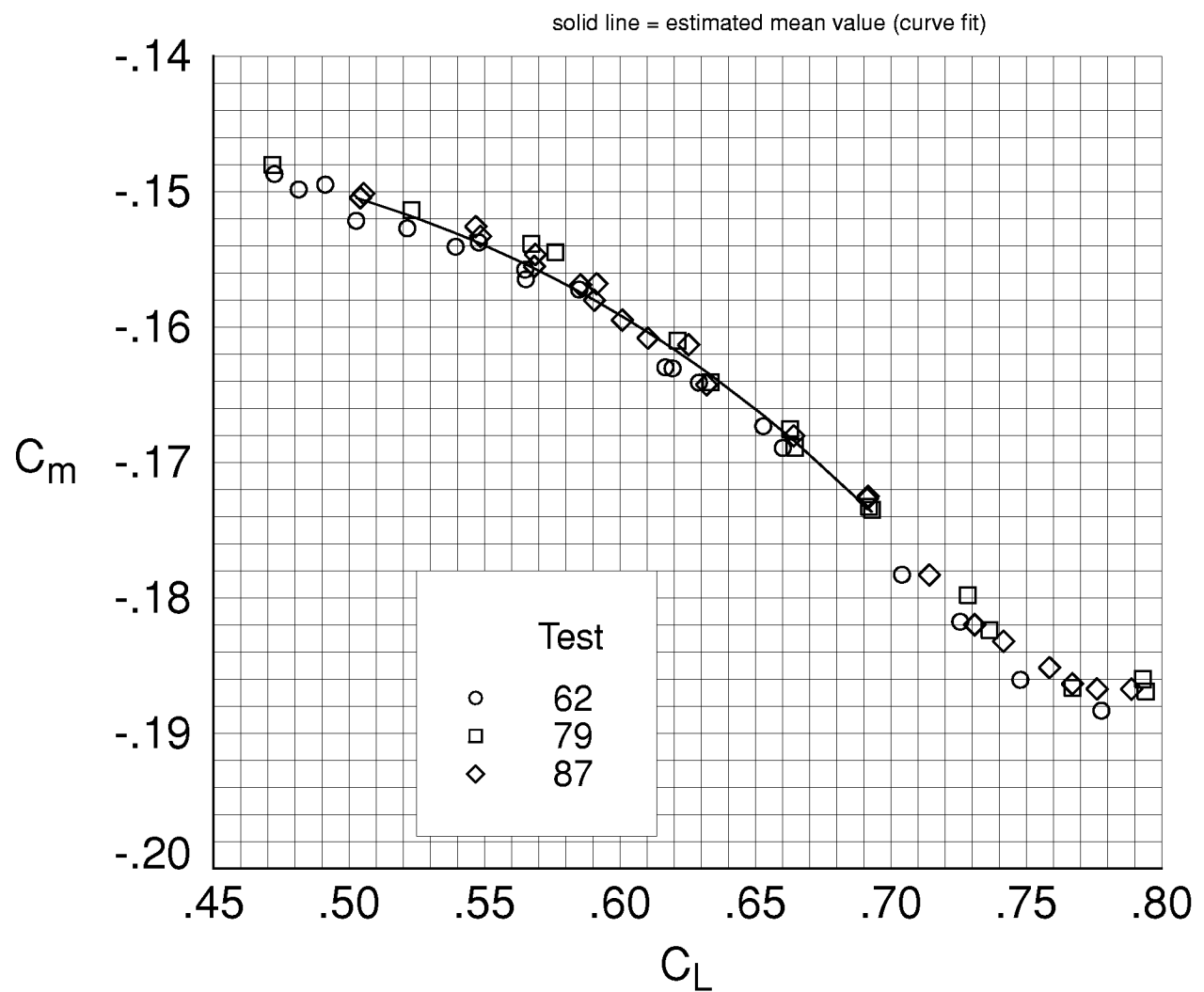
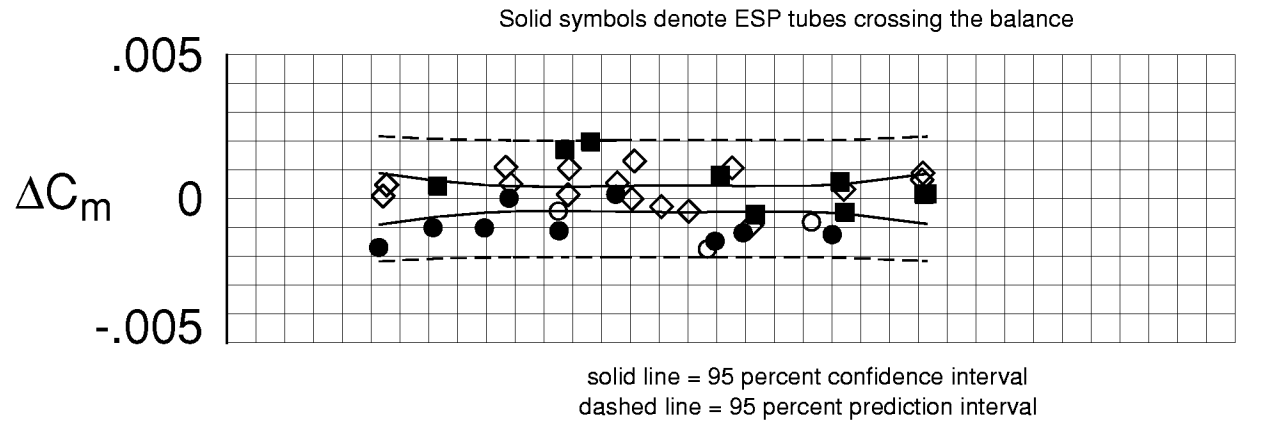
(b) $M_\infty = 0.83$, $R_c^- = 30. \times 10^6$.

Figure 5. Continued.



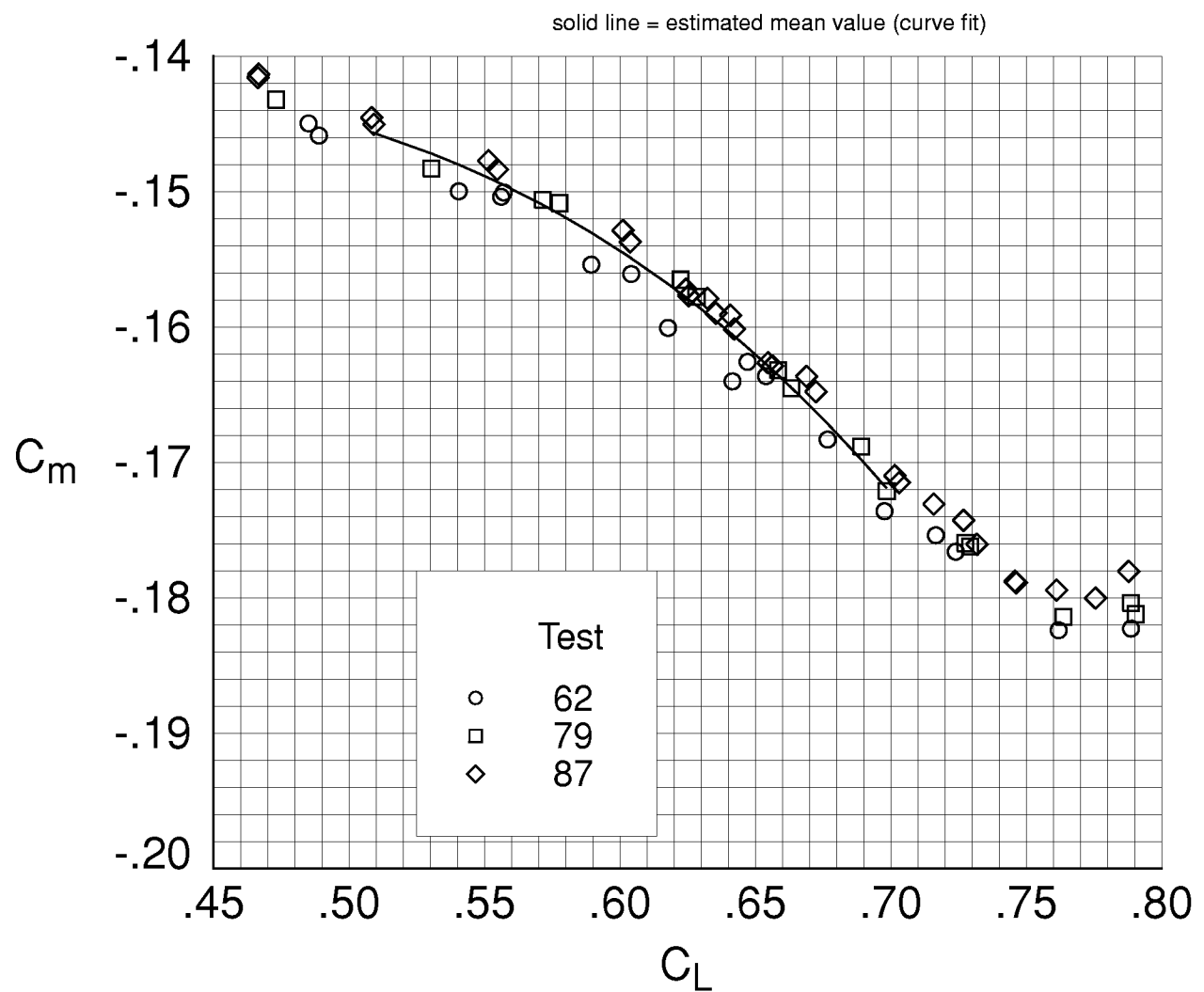
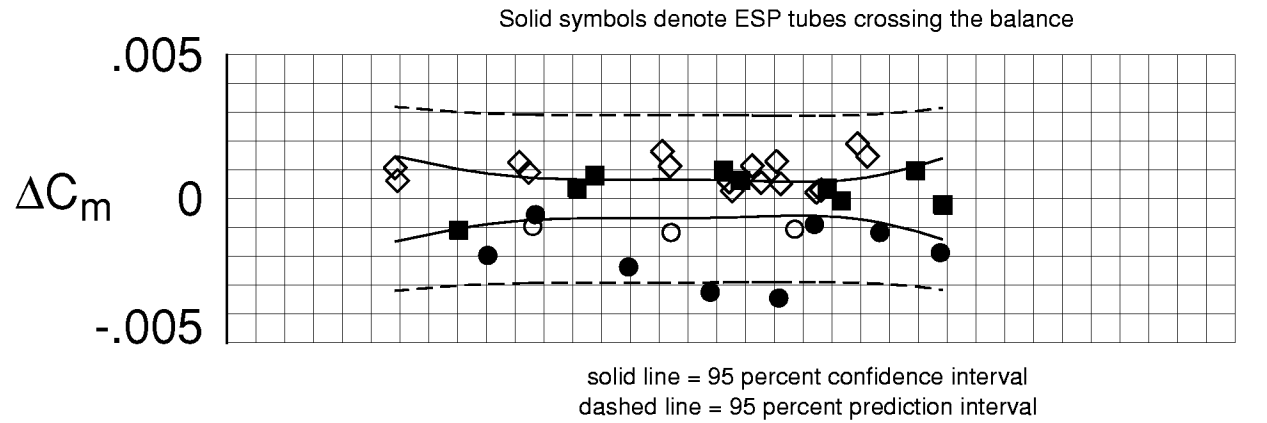
(c) $M_\infty = 0.85$, $R_c = 30. \times 10^6$.

Figure 5. Continued.



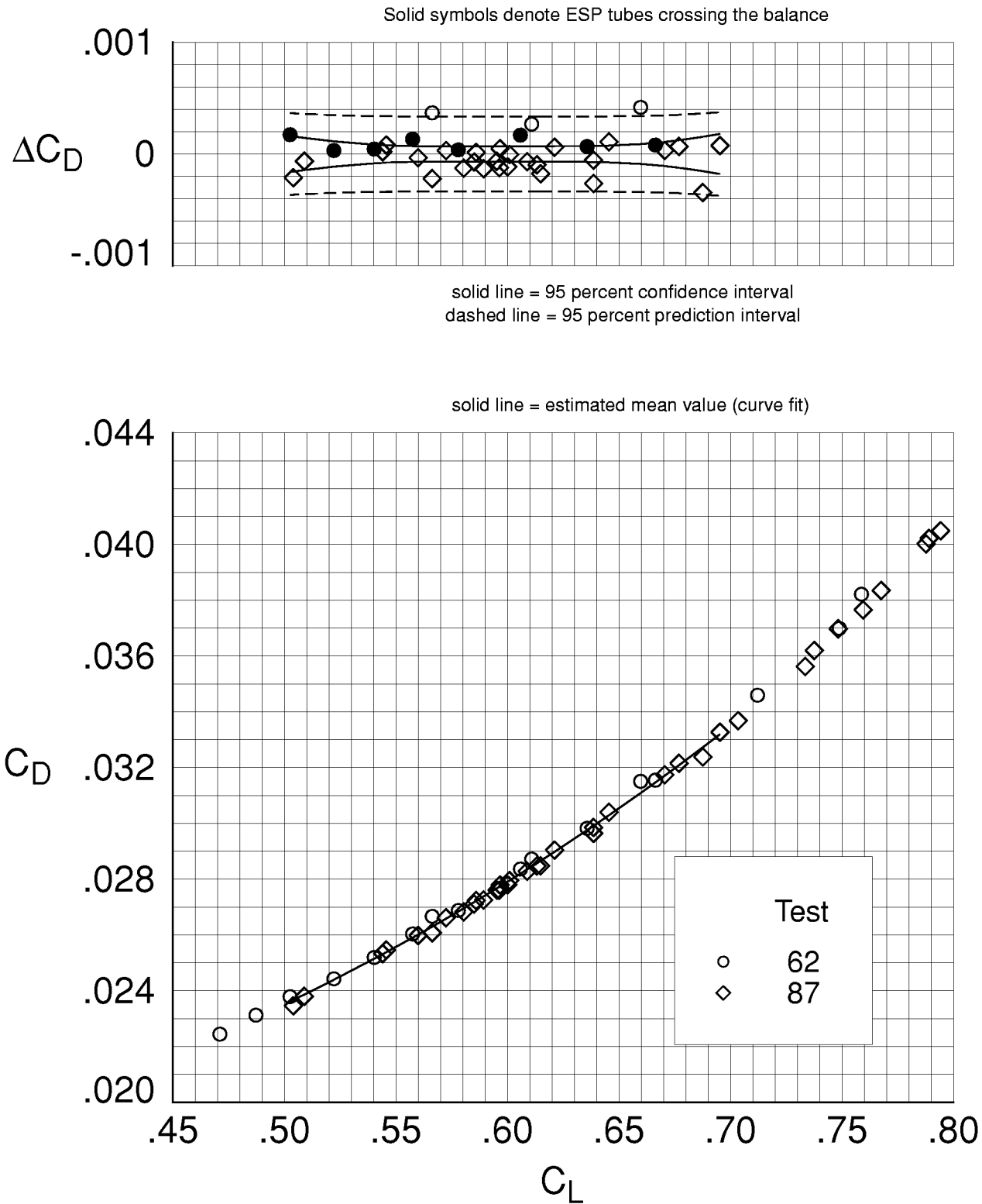
(d) $M_\infty = 0.85$, $R_c^- = 25. \times 10^6$.

Figure 5. Continued.

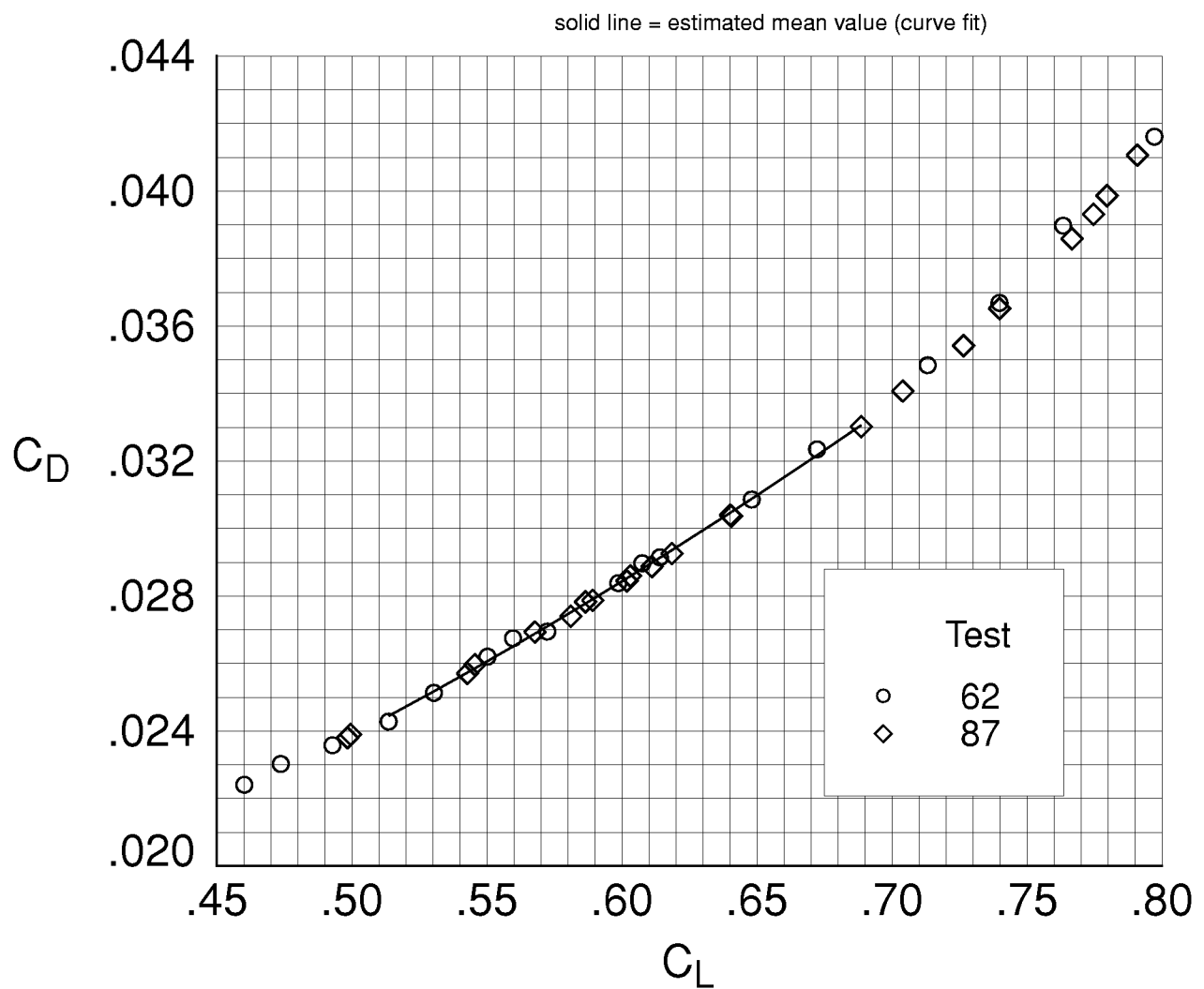
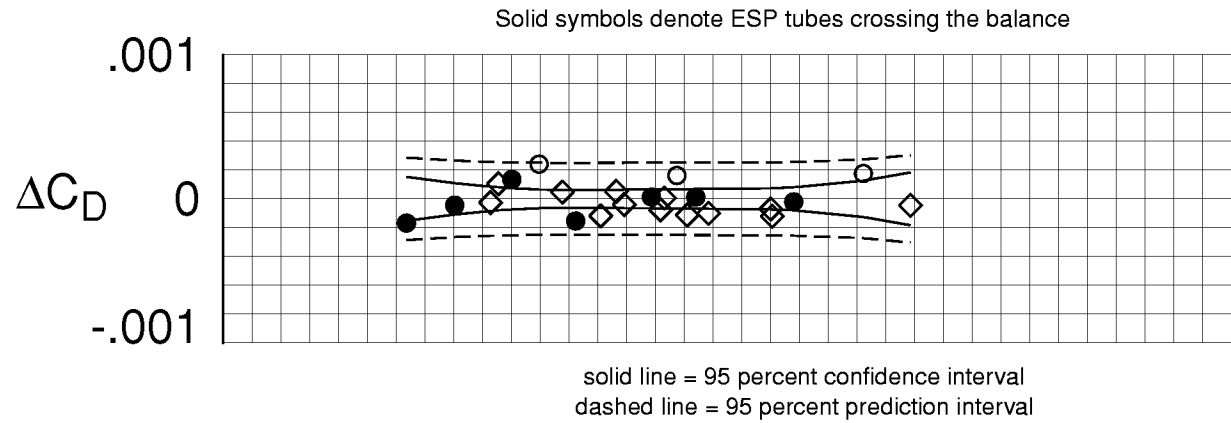


(e) $M_\infty = 0.85$, $R_c^- = 20. \times 10^6$.

Figure 5. Concluded.

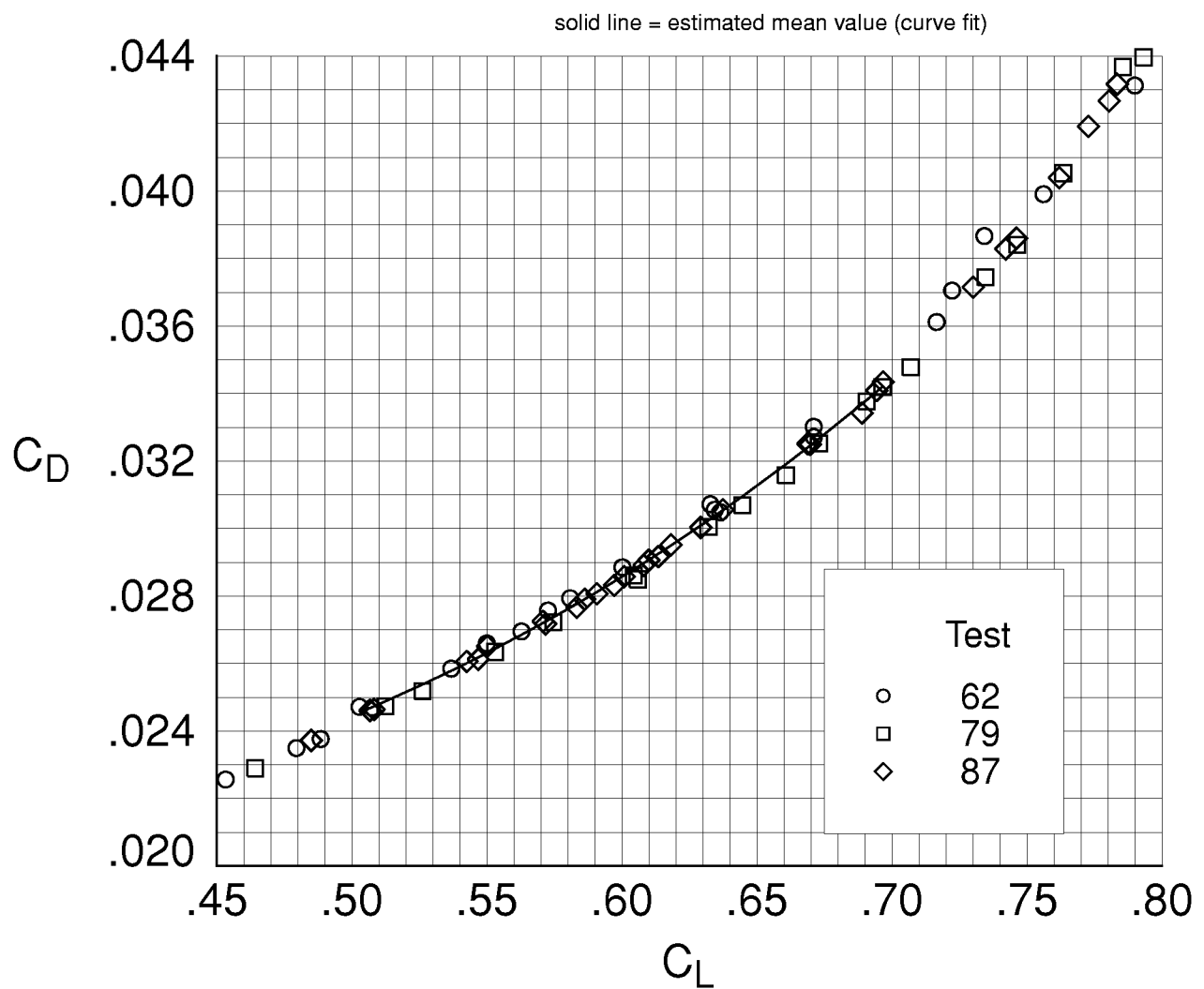
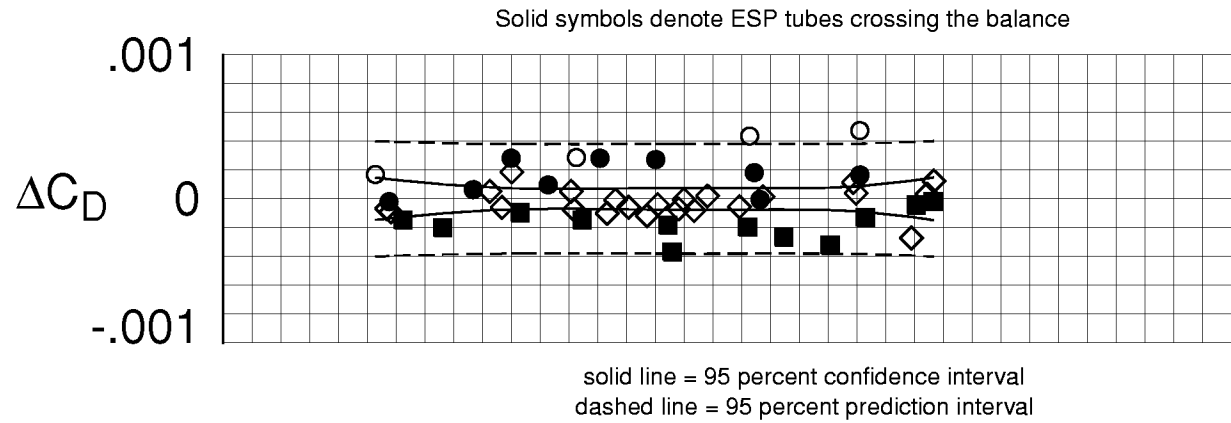


(a) $M_\infty = 0.80$, $R_c = 30. \times 10^6$.
Figure 6. Analysis of repeated C_D data.



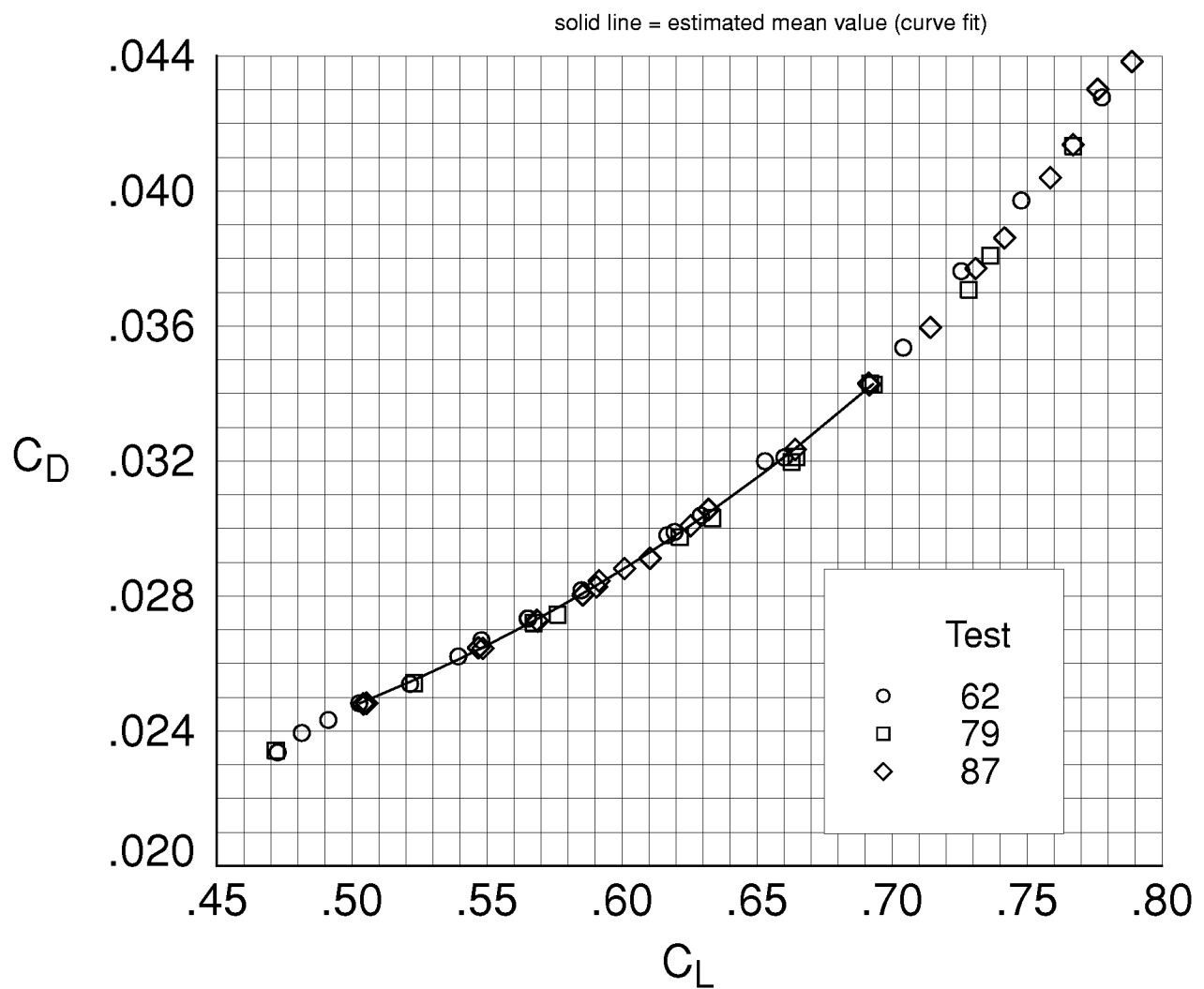
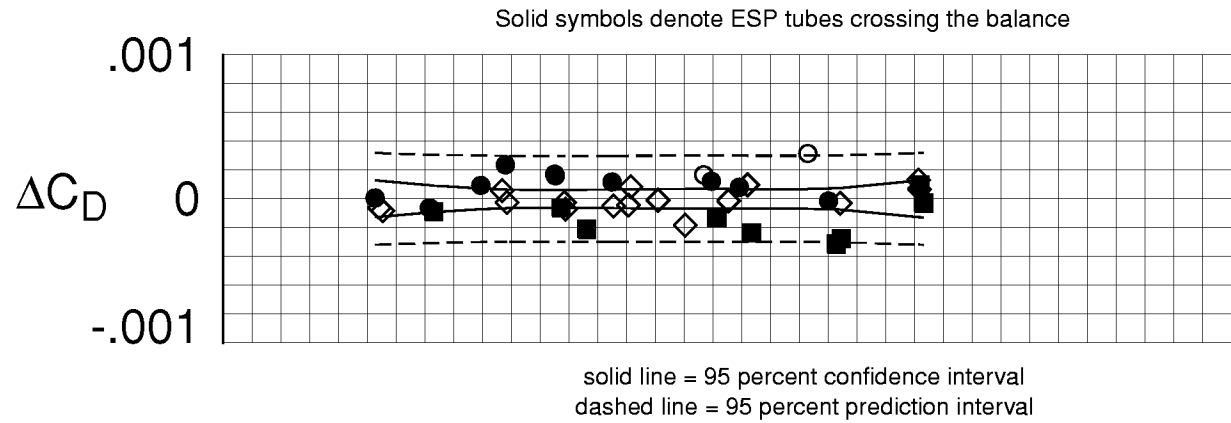
(b) $M_\infty = 0.83$, $R_c^- = 30. \times 10^6$.

Figure 6. Continued.



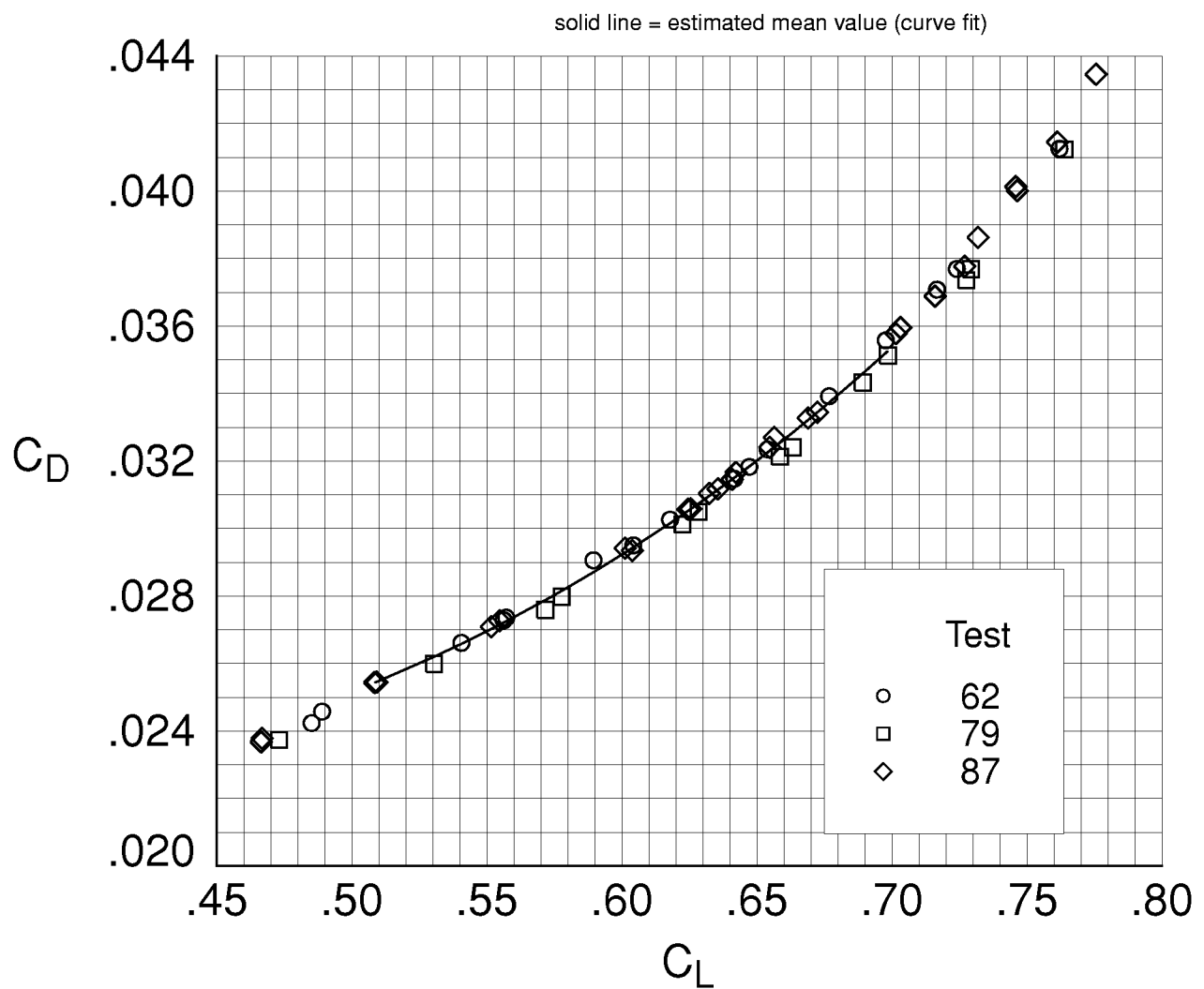
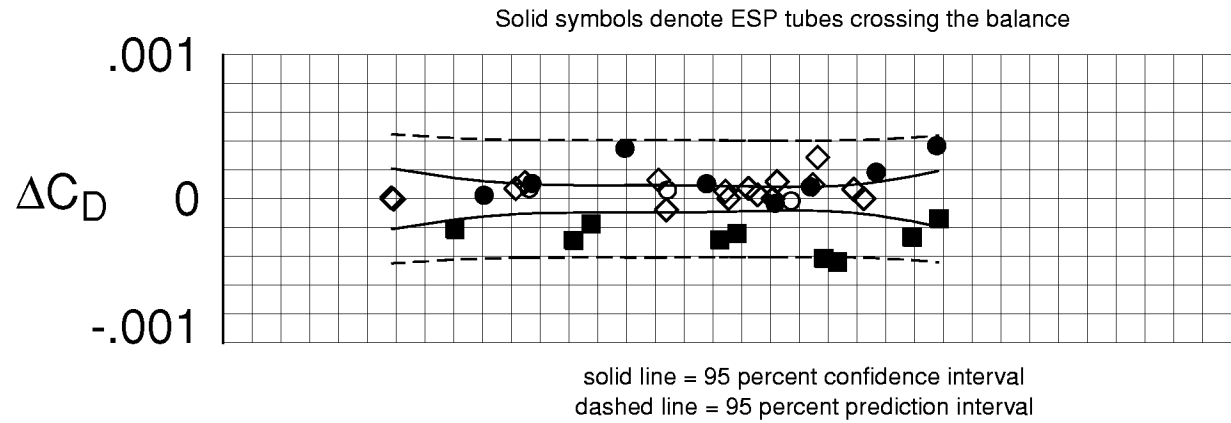
(c) $M_\infty = 0.85$, $R_c^- = 30. \times 10^6$.

Figure 6. Continued.



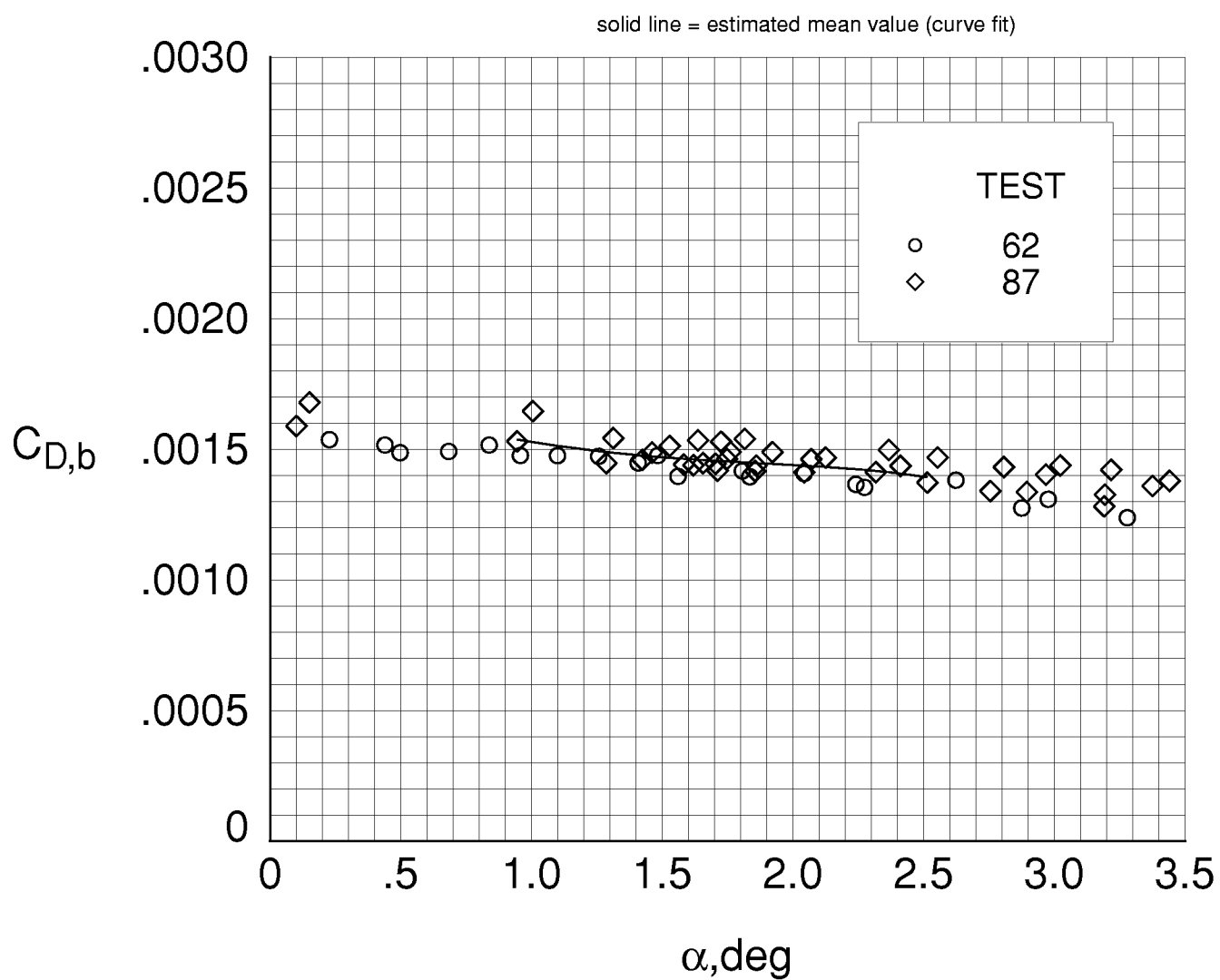
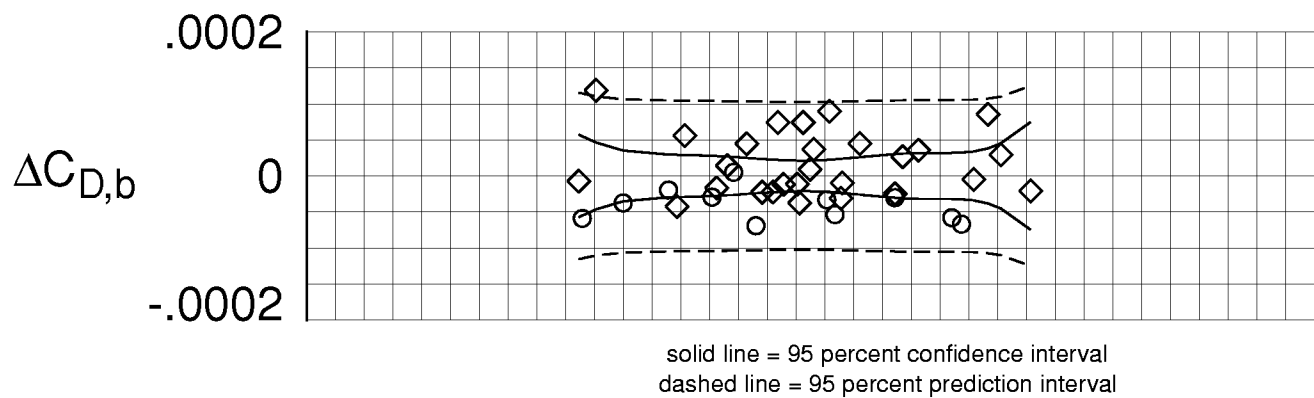
(d) $M_\infty = 0.85$, $R_c^- = 25. \times 10^6$.

Figure 6. Continued.



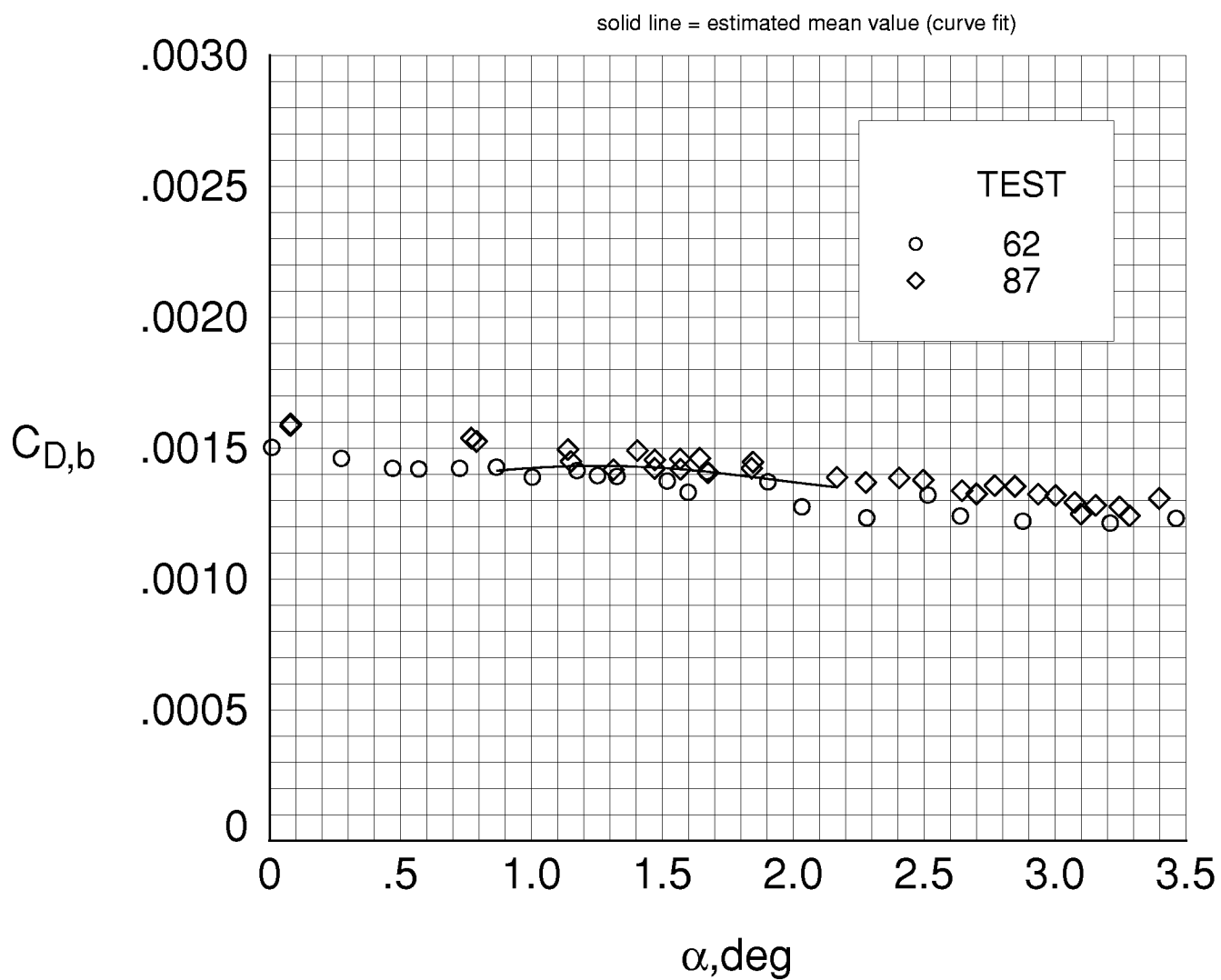
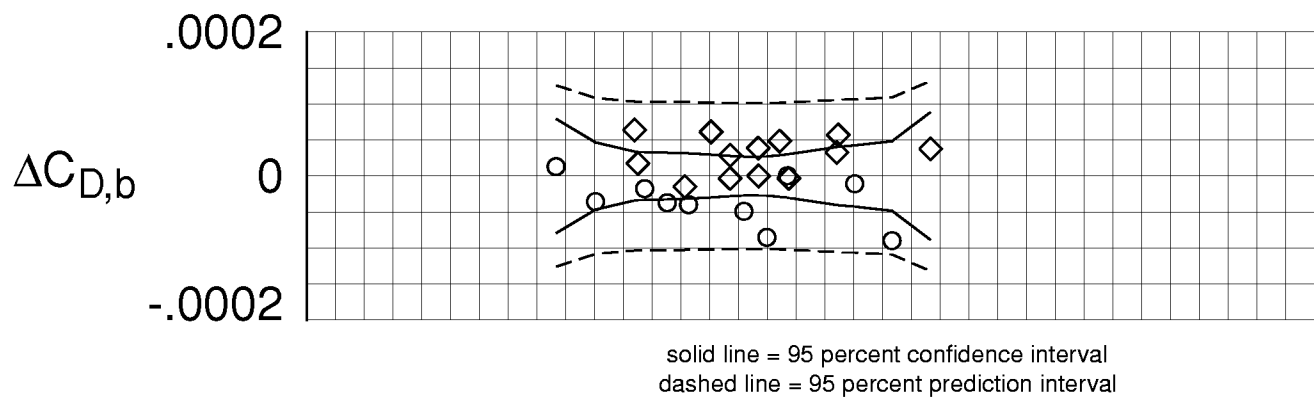
(e) $M_\infty = 0.85$, $R_c^- = 20. \times 10^6$.

Figure 6. Concluded.



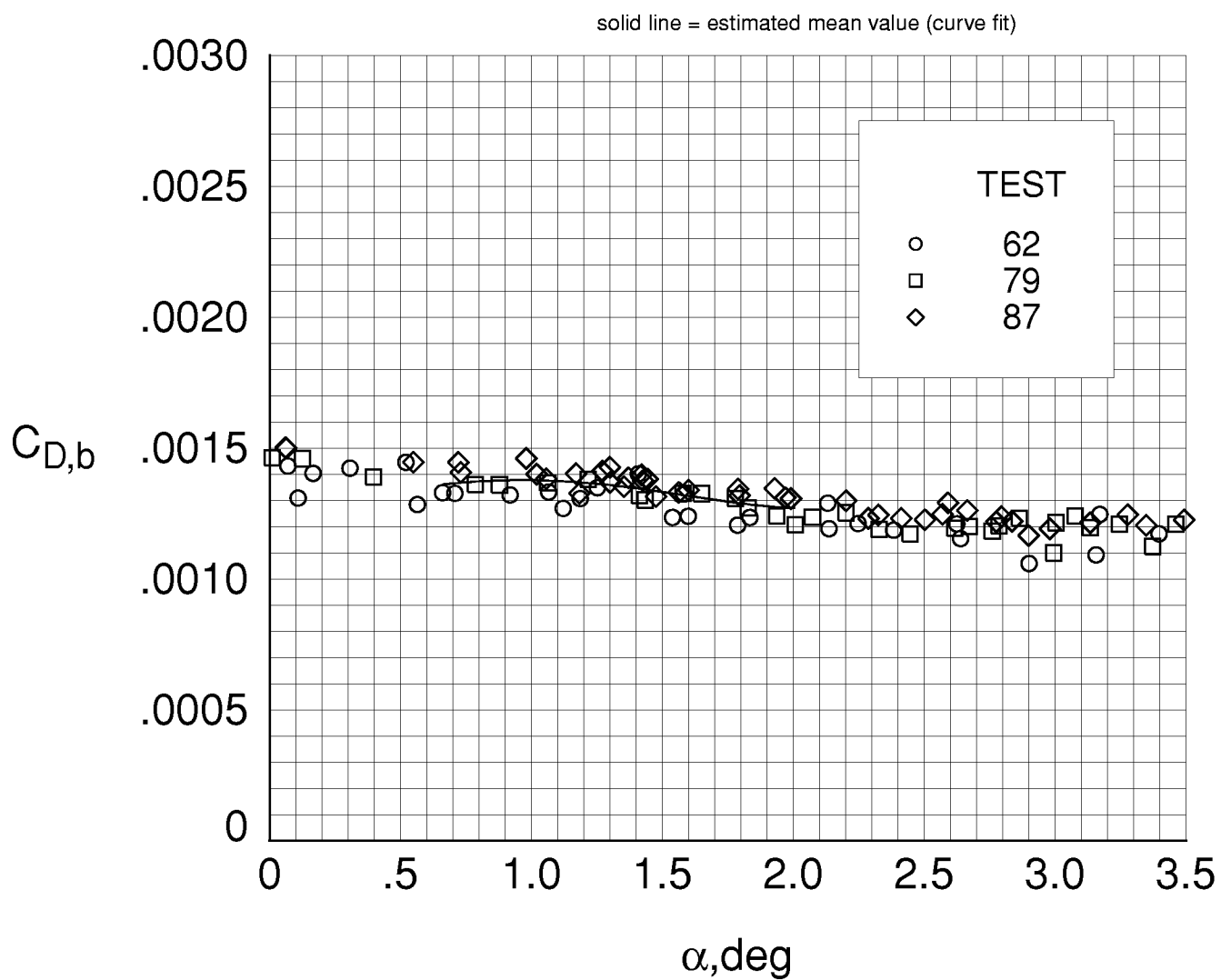
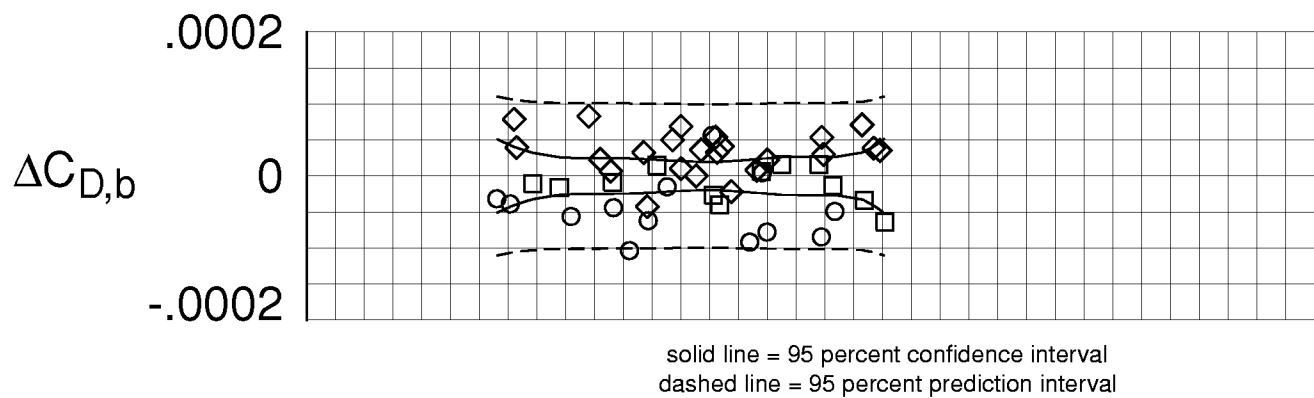
(a) $M_\infty = 0.80$, $R_c = 30. \times 10^6$.

Figure 7. Analysis of repeated $C_{D,b}$ data.



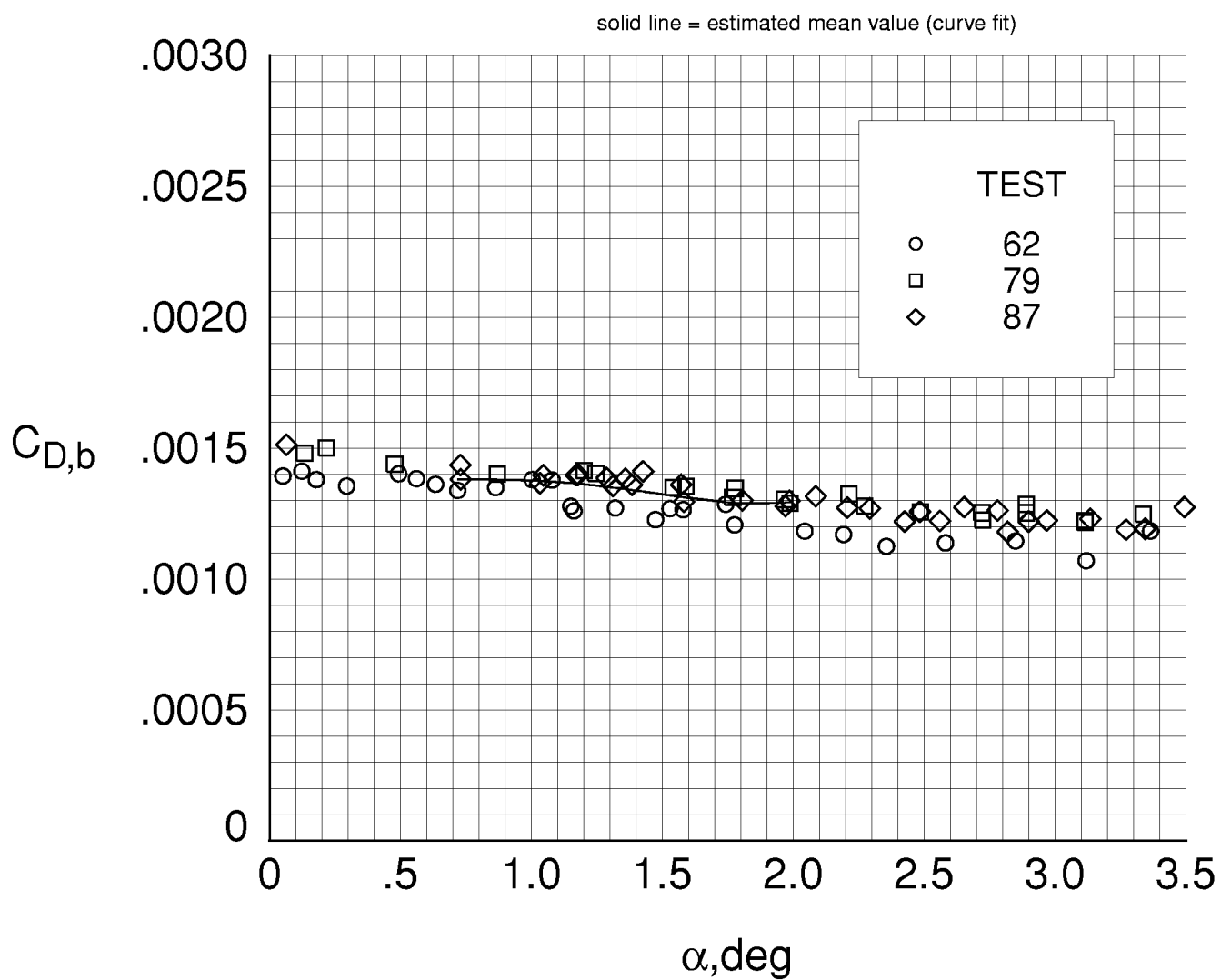
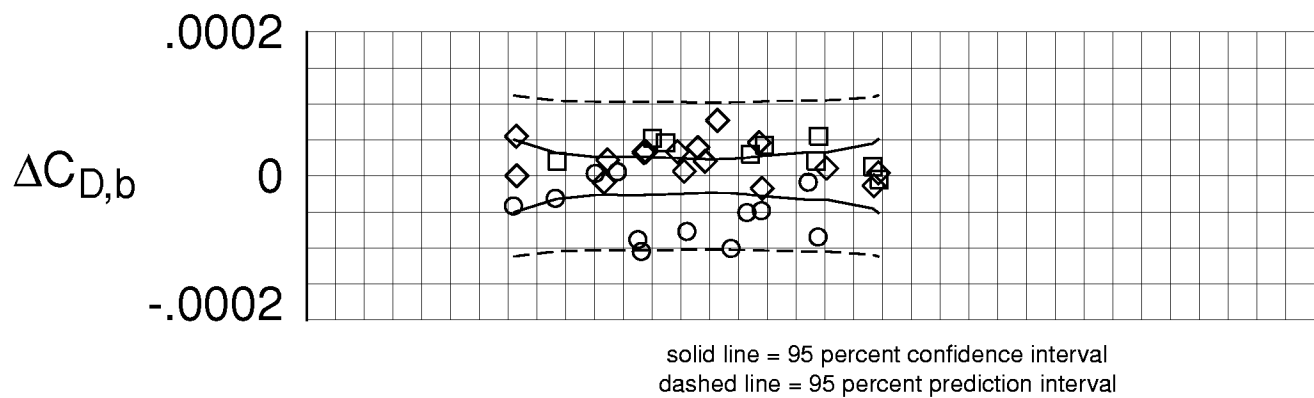
(b) $M_\infty = 0.83$, $R_c^- = 30. \times 10^6$.

Figure 7. Continued.



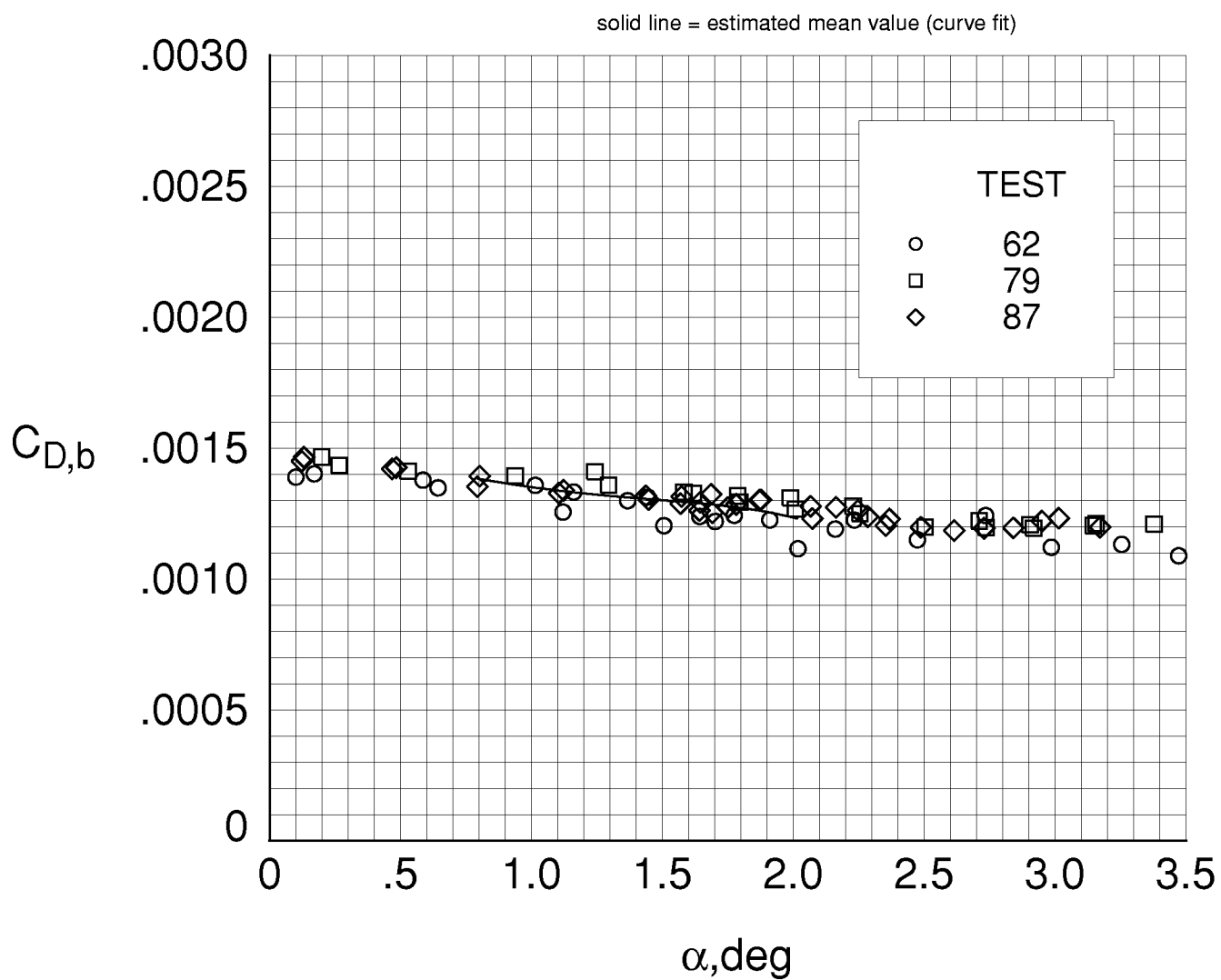
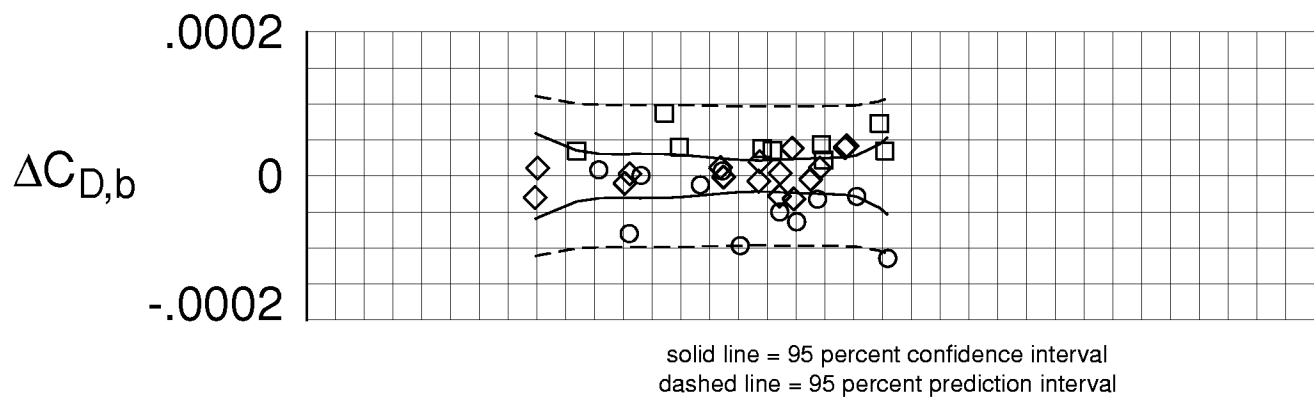
(c) $M_\infty = 0.85$, $R_c^- = 30. \times 10^6$.

Figure 7. Continued.



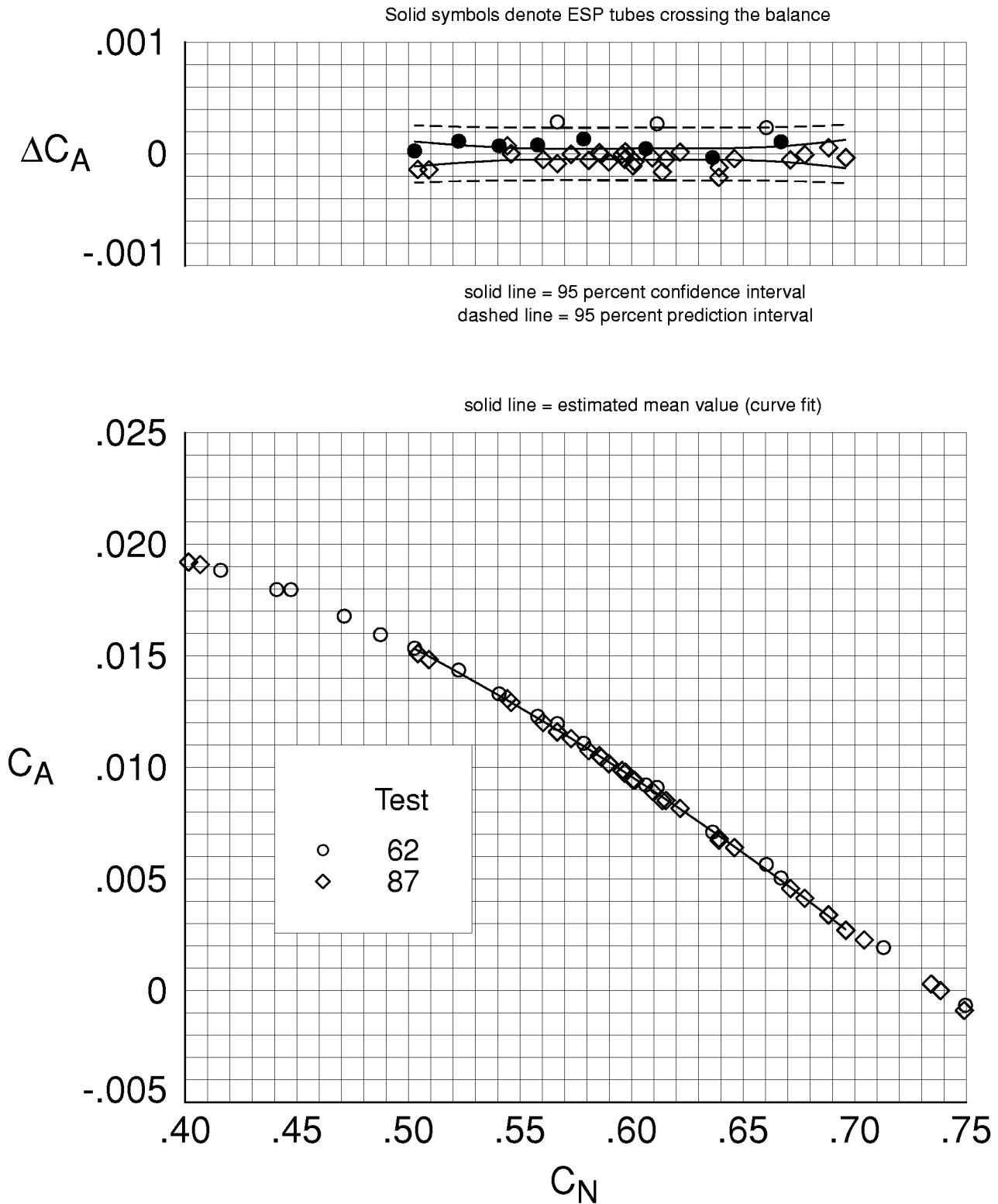
(d) $M_\infty = 0.85$, $R_c^- = 25. \times 10^6$.

Figure 7. Continued.

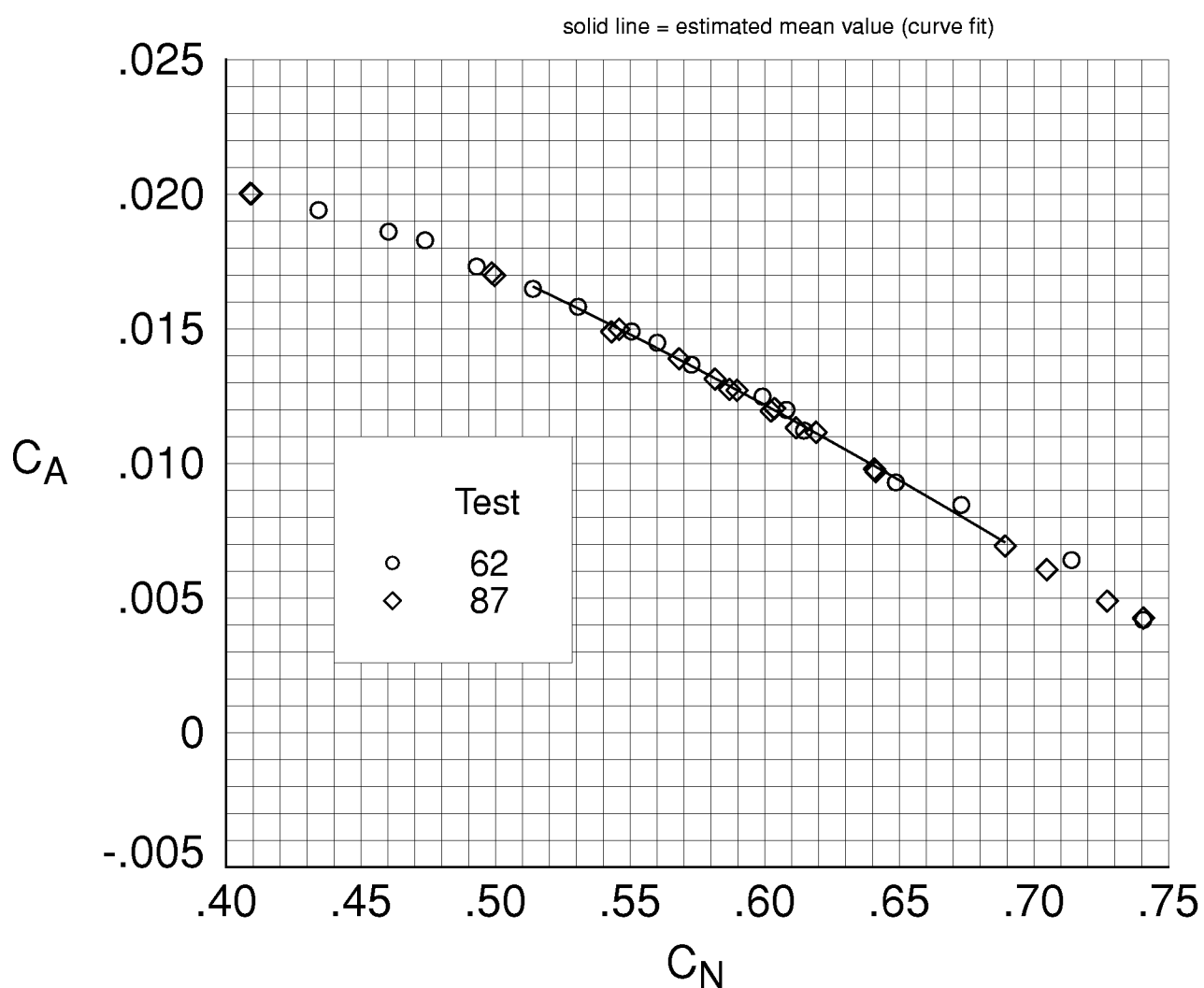
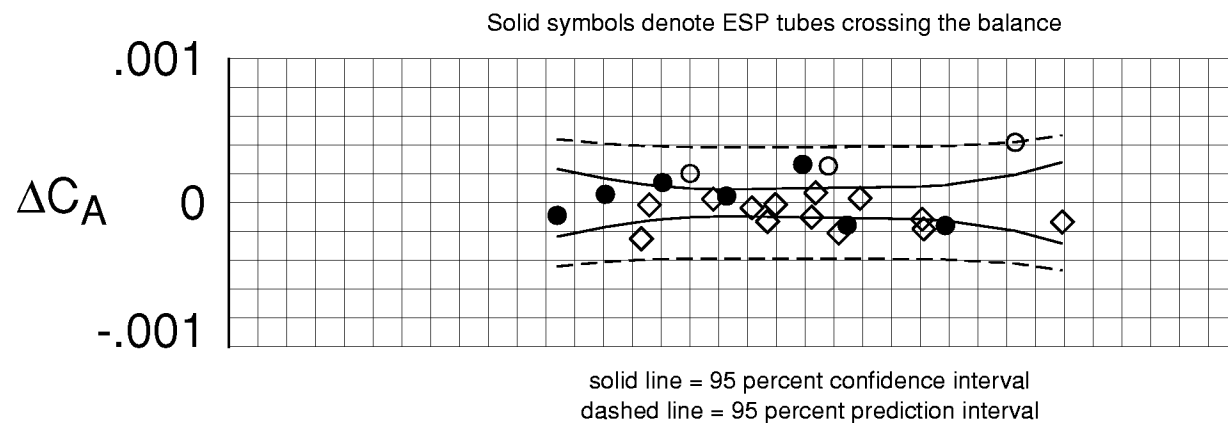


(e) $M_\infty = 0.85$, $R_c^- = 20. \times 10^6$.

Figure 7. Concluded.

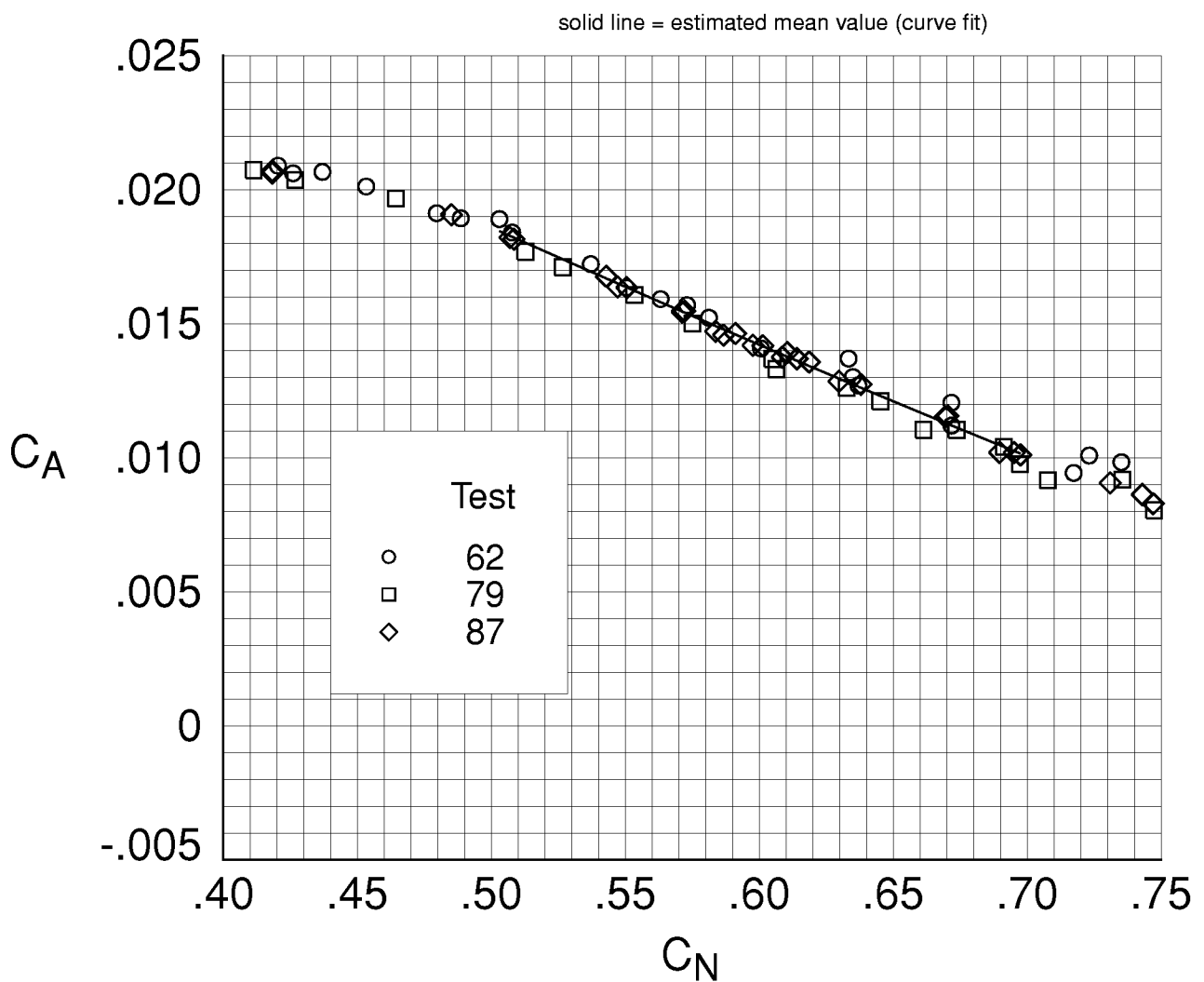
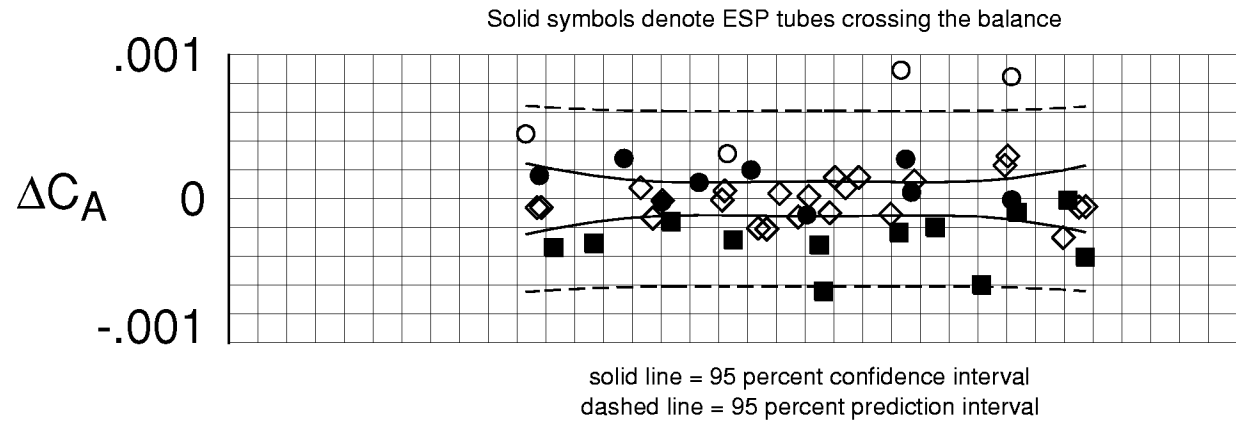


(a) $M_\infty = 0.80$, $R_C^- = 30. \times 10^6$.
Figure 8. Analysis of repeated C_A data.



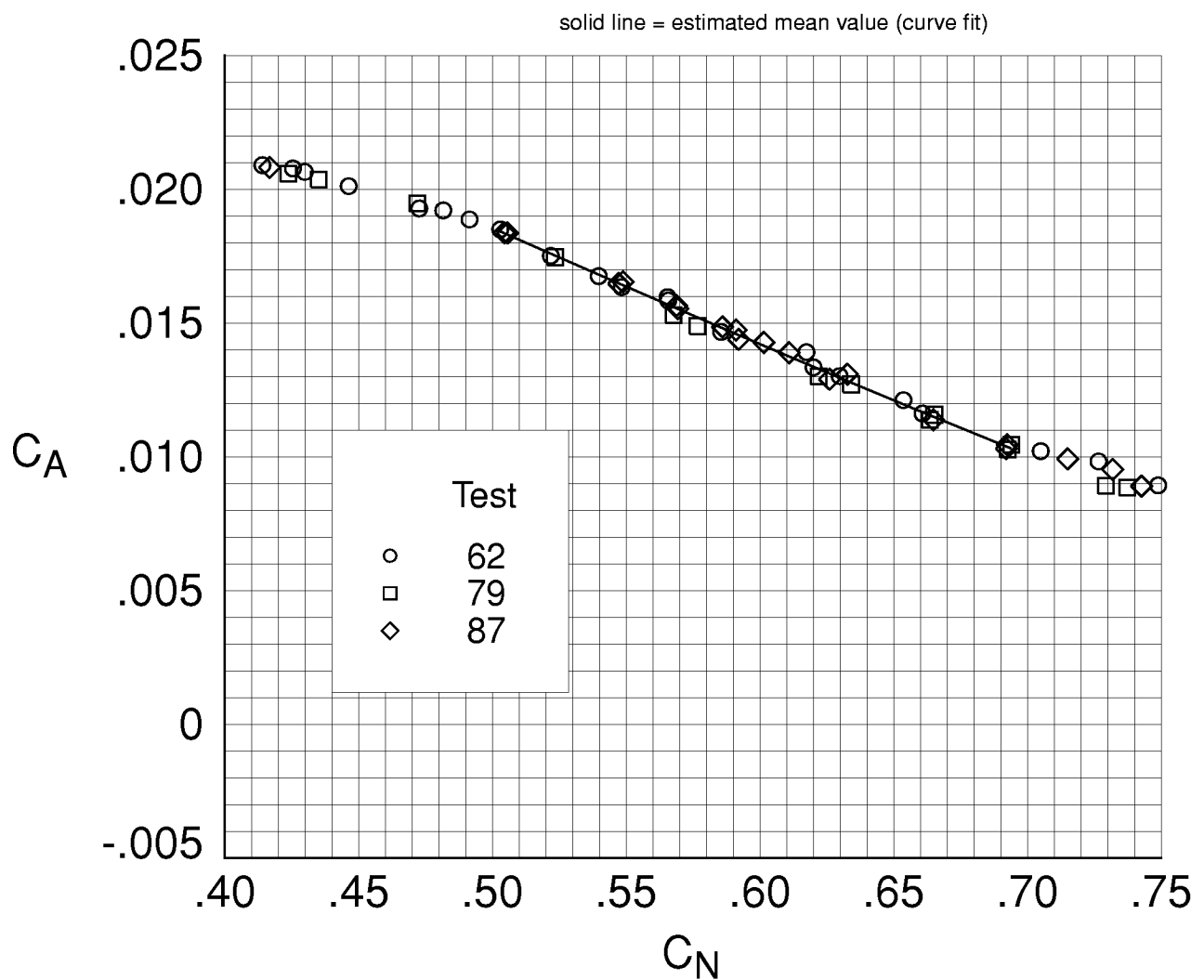
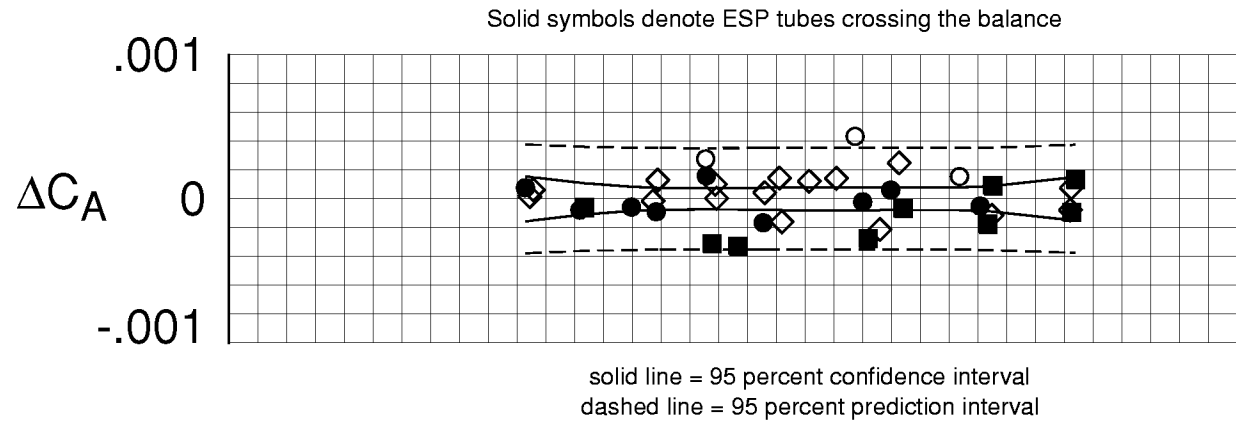
(b) $M_\infty = 0.83$, $R_C^- = 30. \times 10^6$.

Figure 8. Continued.



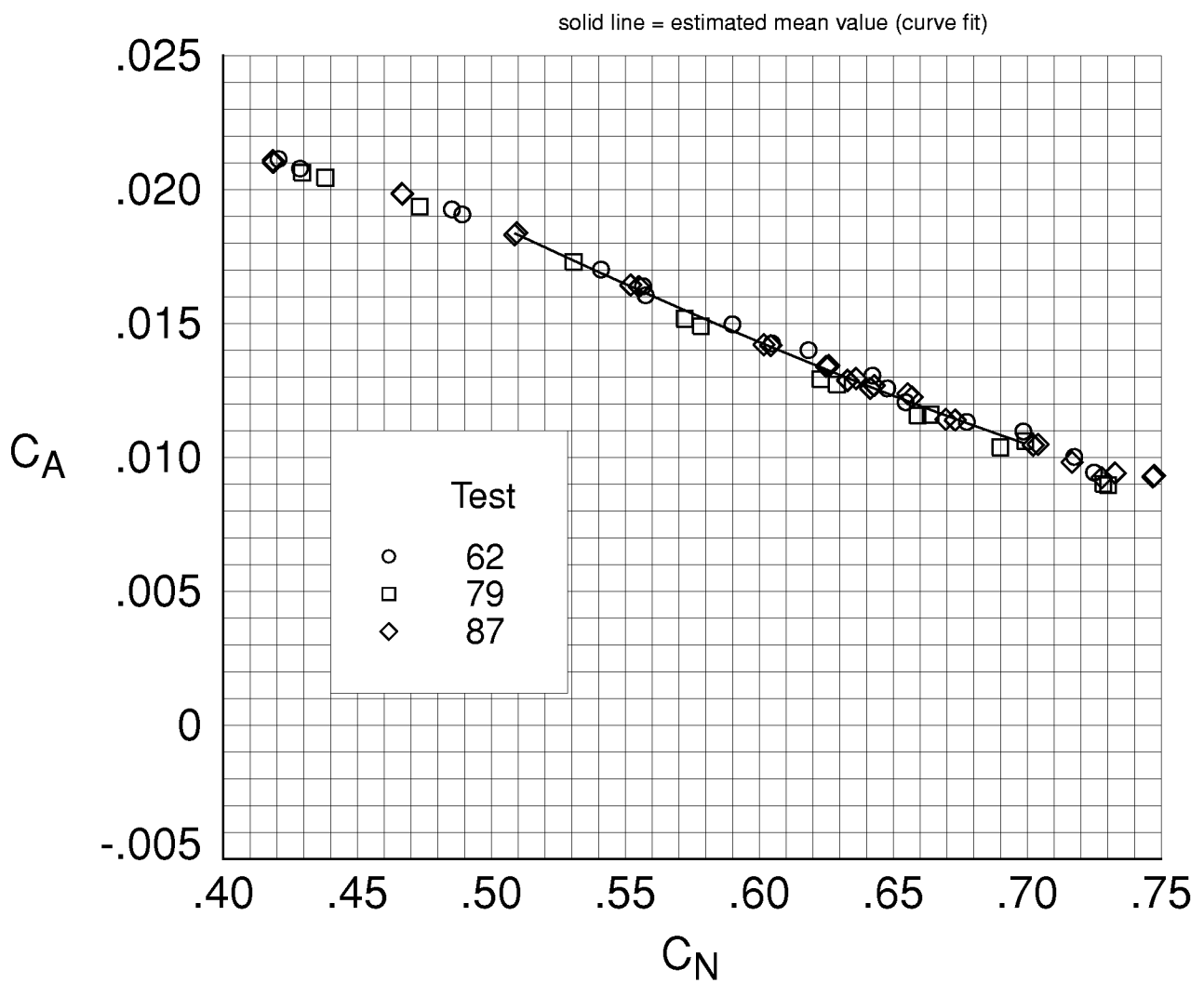
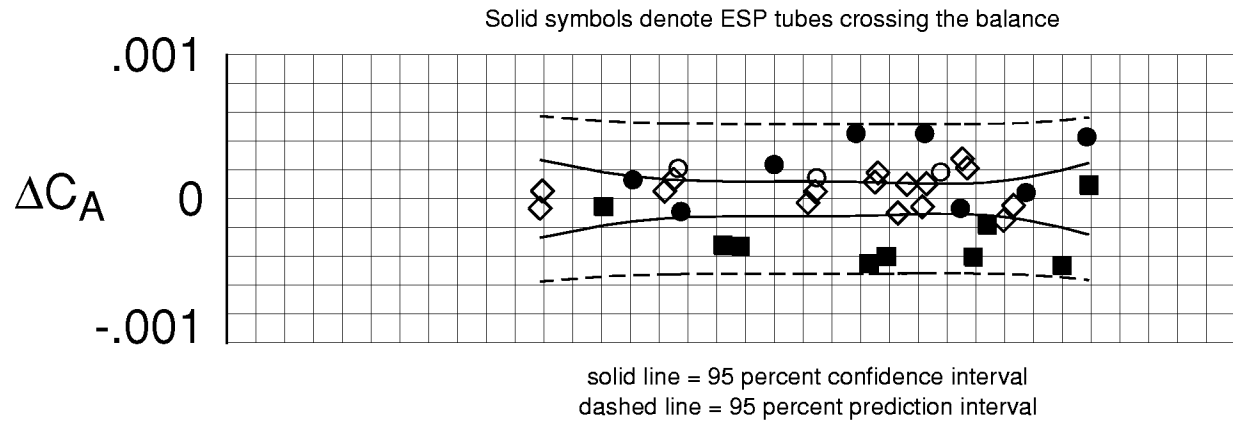
(c) $M_\infty = 0.85$, $R_c^- = 30. \times 10^6$.

Figure 8. Continued.



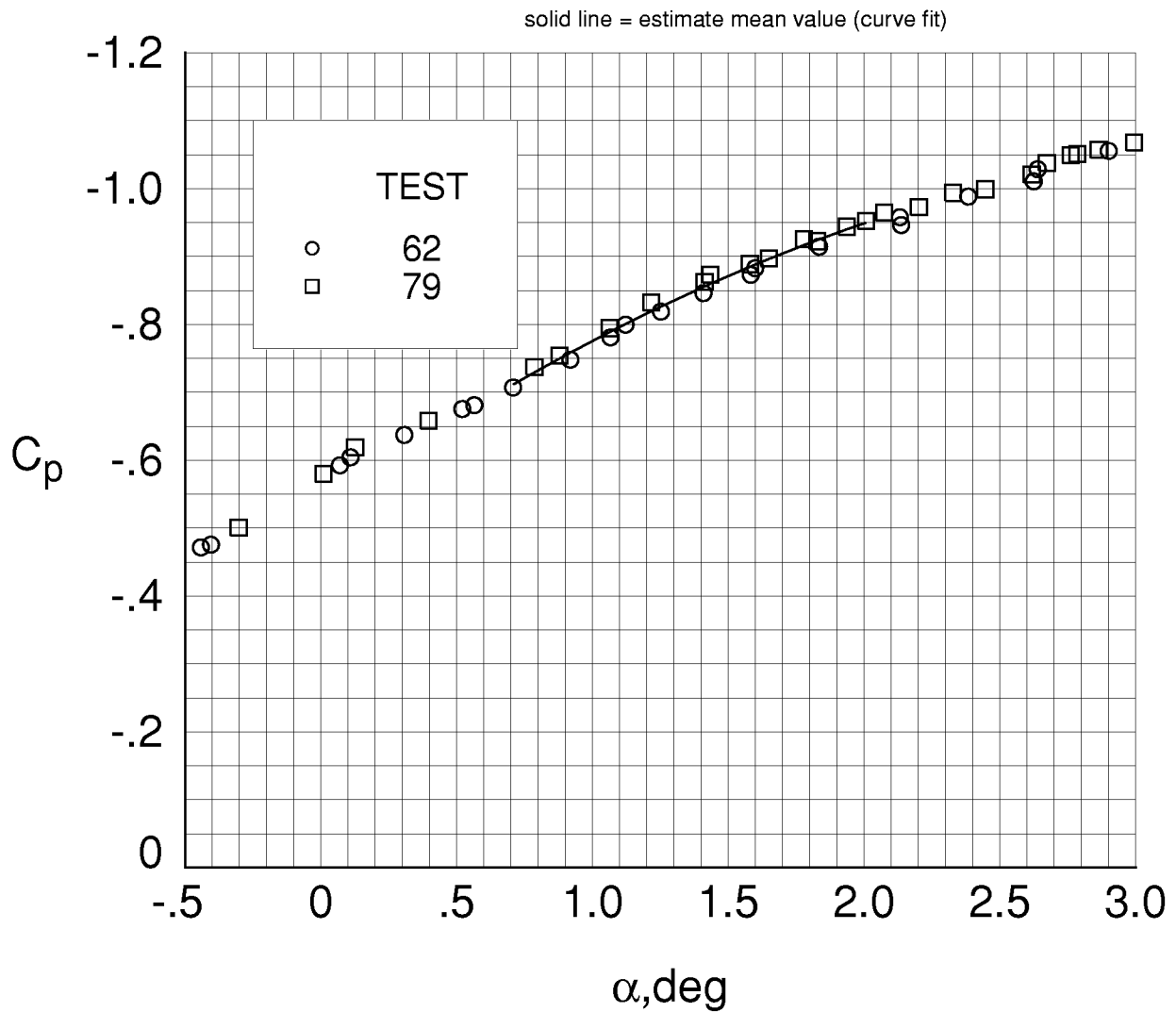
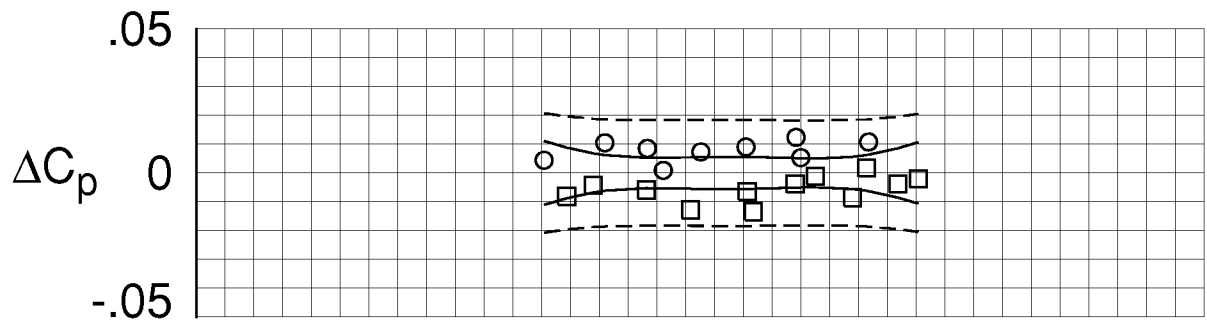
(d) $M_\infty = 0.85$, $R_C^- = 25. \times 10^6$.

Figure 8. Continued.



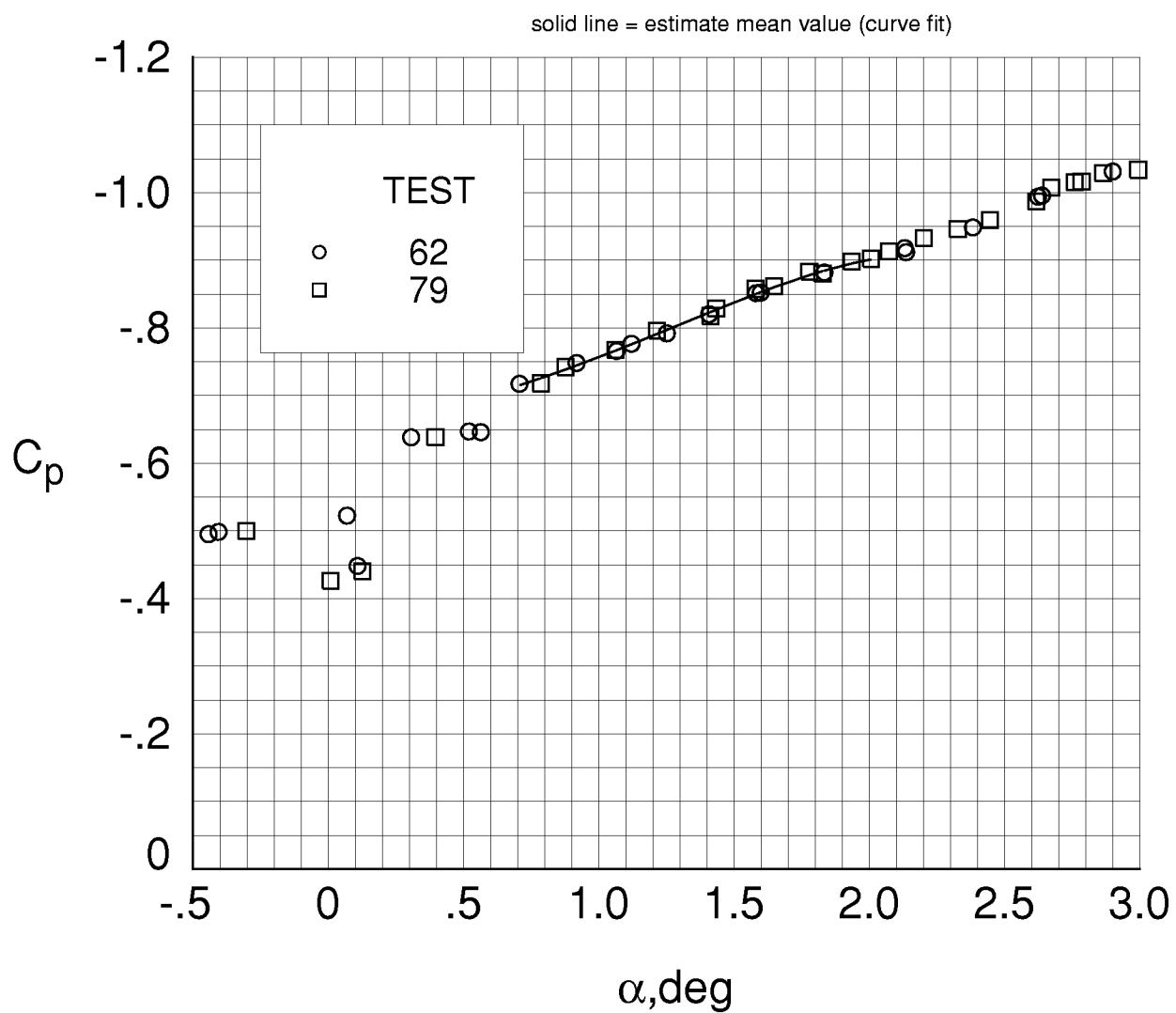
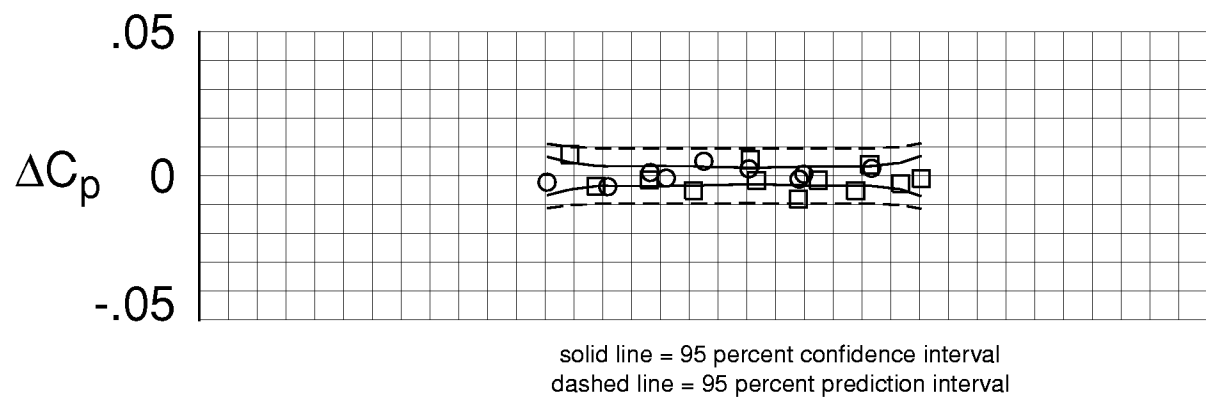
(e) $M_\infty = 0.85$, $R_C^- = 20. \times 10^6$.

Figure 8. Concluded.



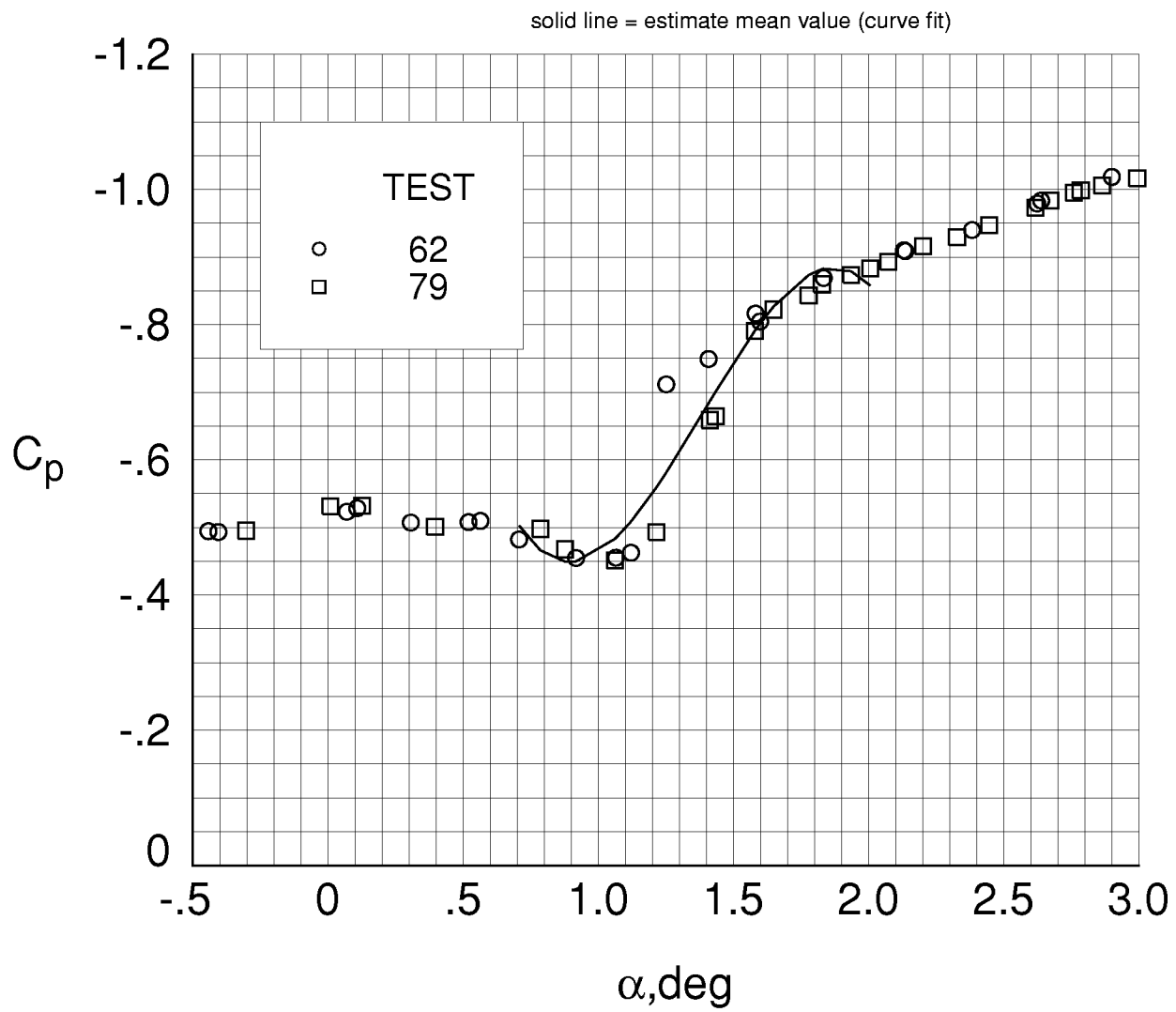
(a) $x/c = 0.05$.

Figure 9. Analysis of repeated C_p data. $\eta = 0.42$, $M_\infty = 0.85$, $R_c^- = 30 \times 10^6$.



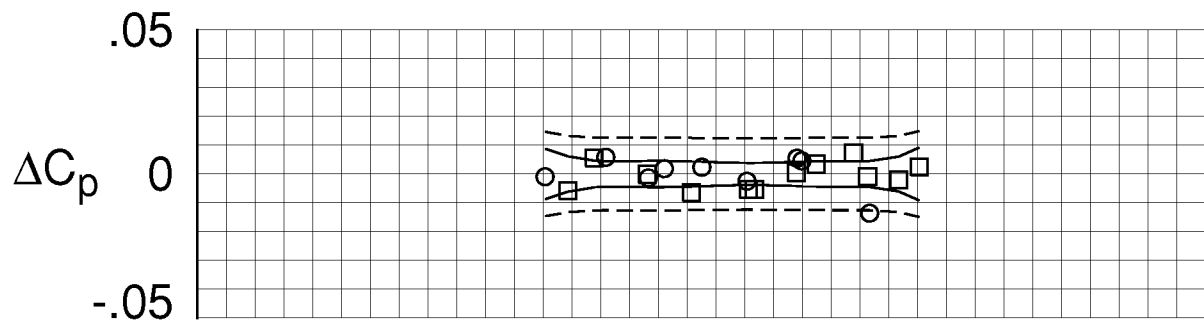
(b) $x/c = 0.25$.

Figure 9. Continued.

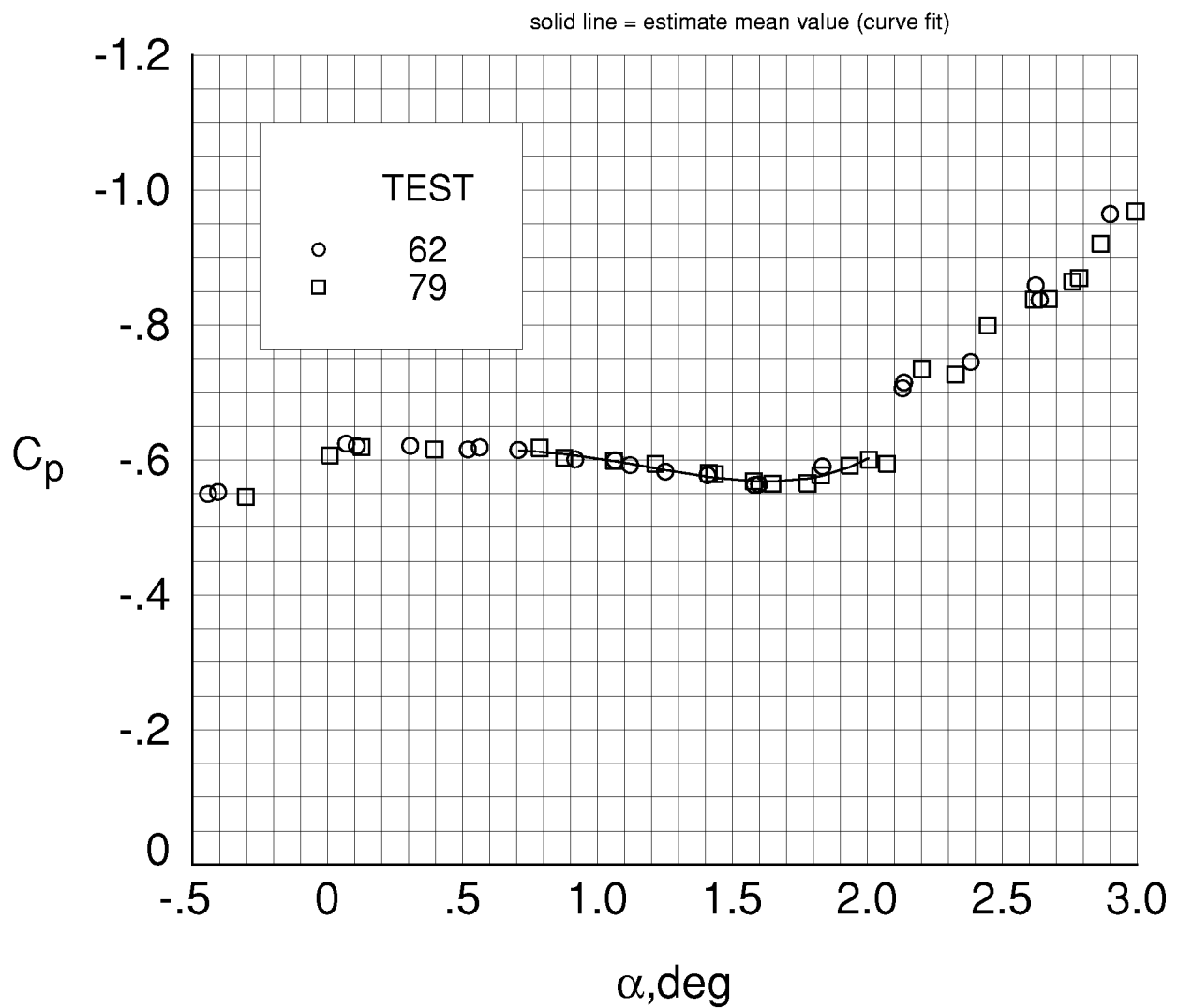


(c) $x/c = 0.45$.

Figure 9. Continued.

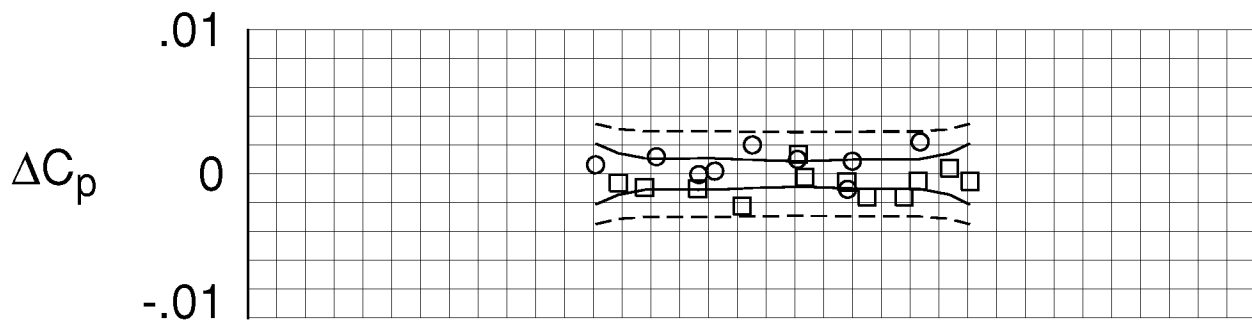


solid line = 95 percent confidence interval
dashed line = 95 percent prediction interval

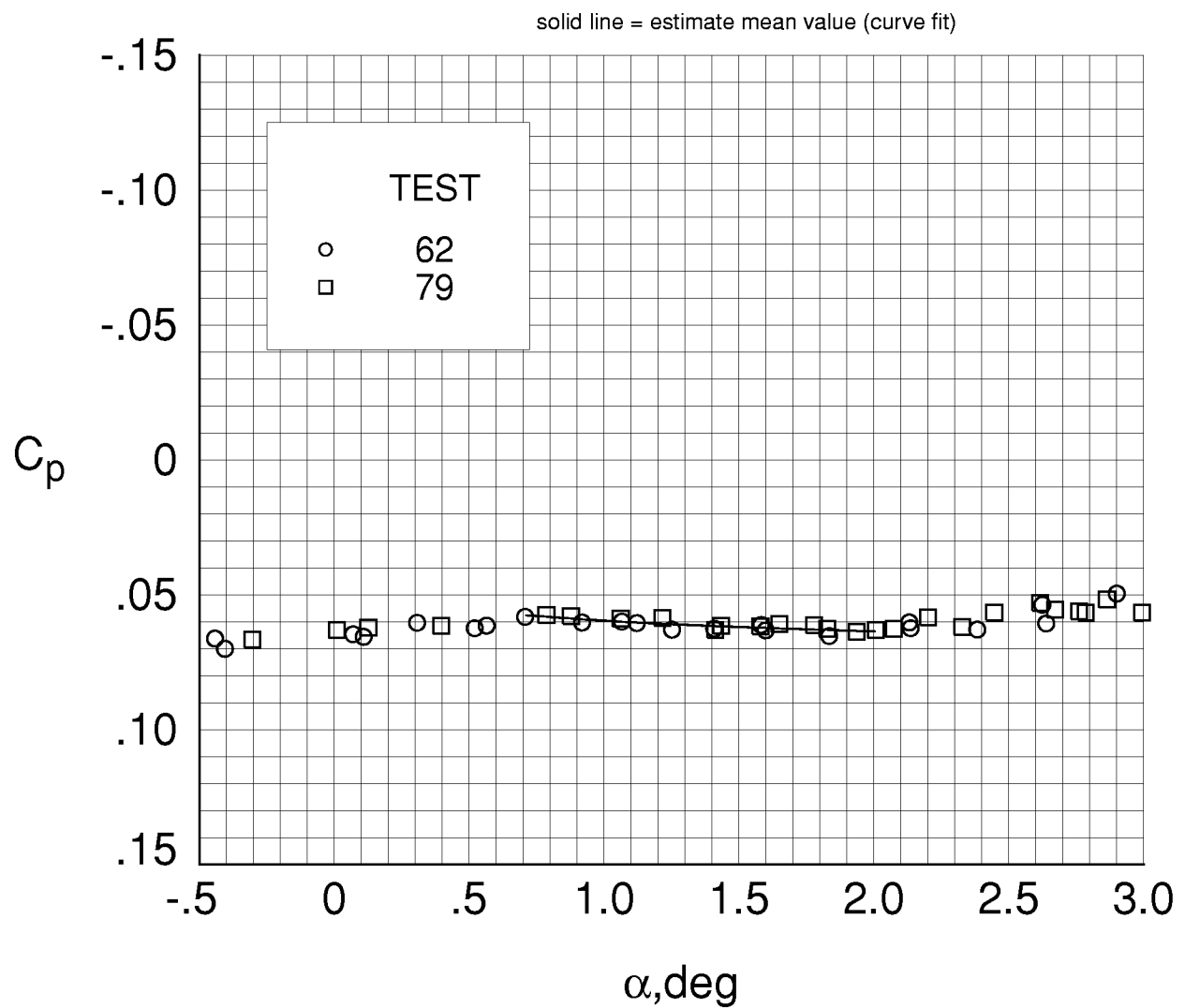


(d) $x/c = 0.62$.

Figure 9. Continued.

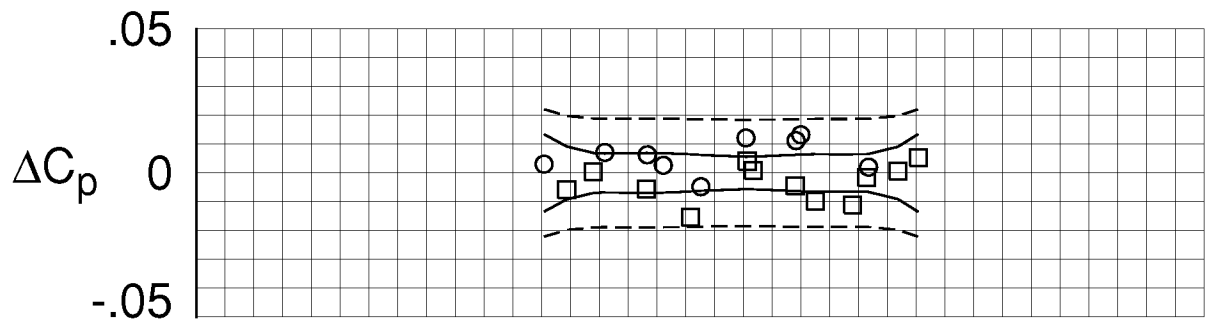


solid line = 95 percent confidence interval
dashed line = 95 percent prediction interval

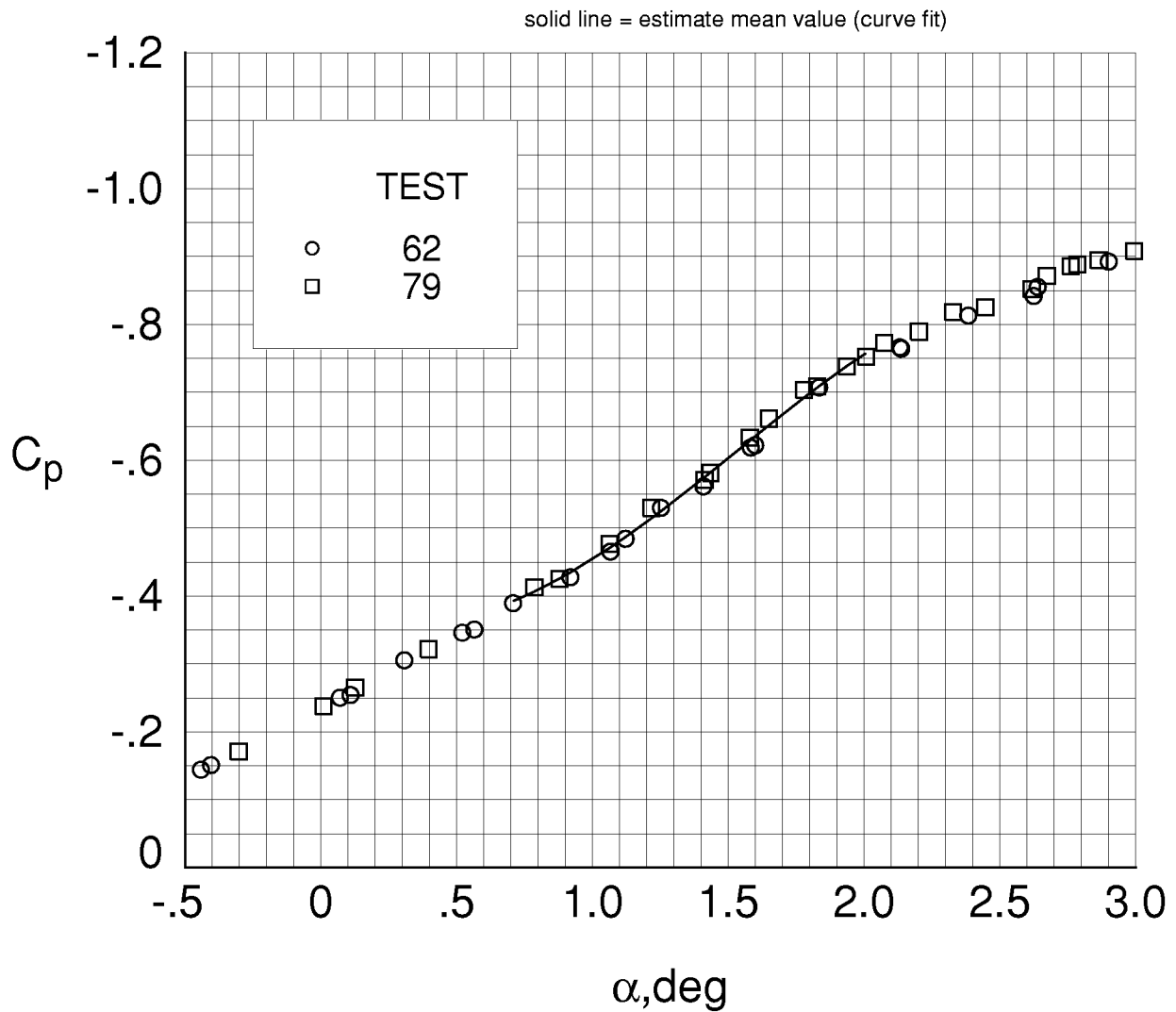


(e) $x/c = 1.00$

Figure 9. Concluded.

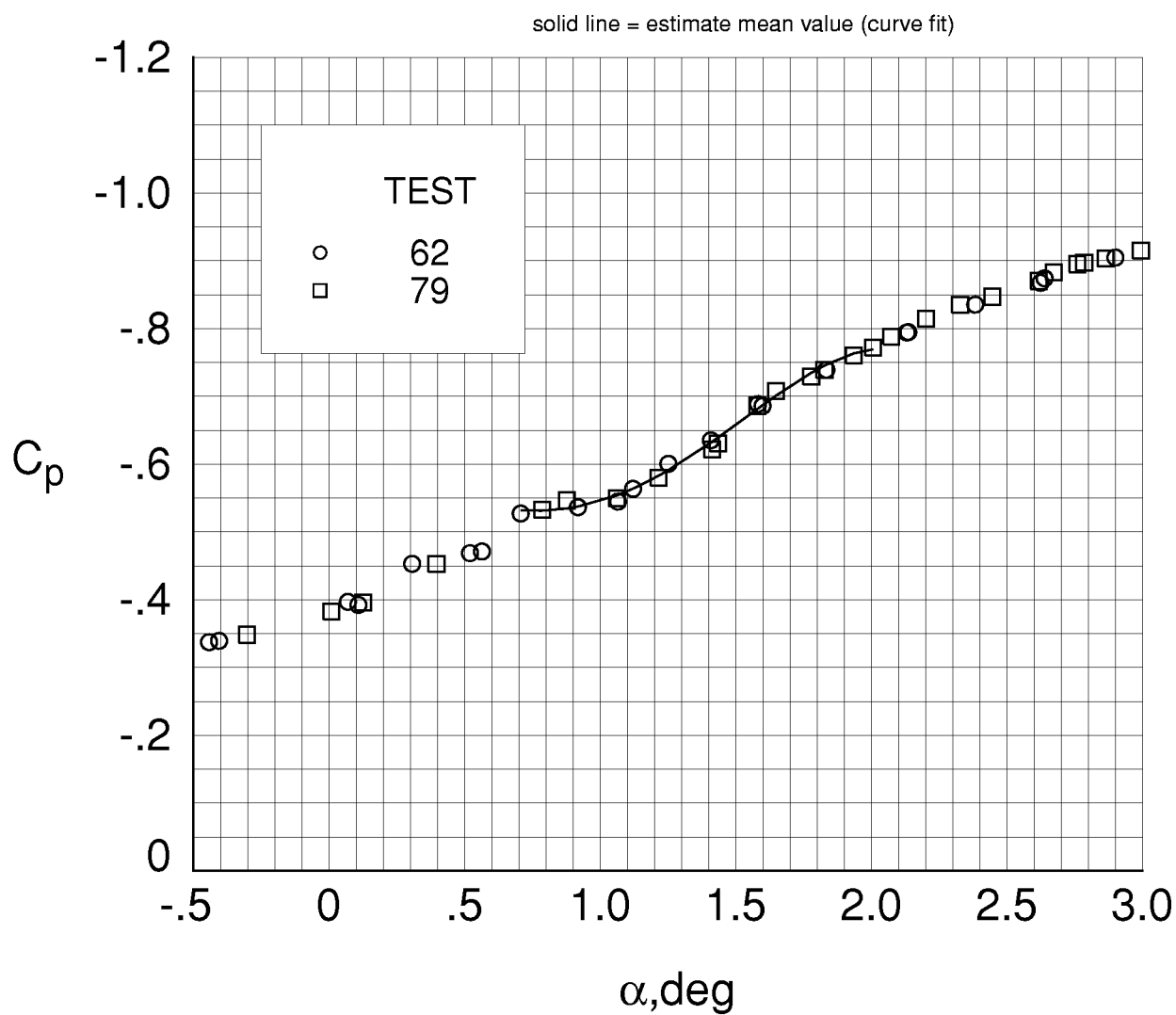
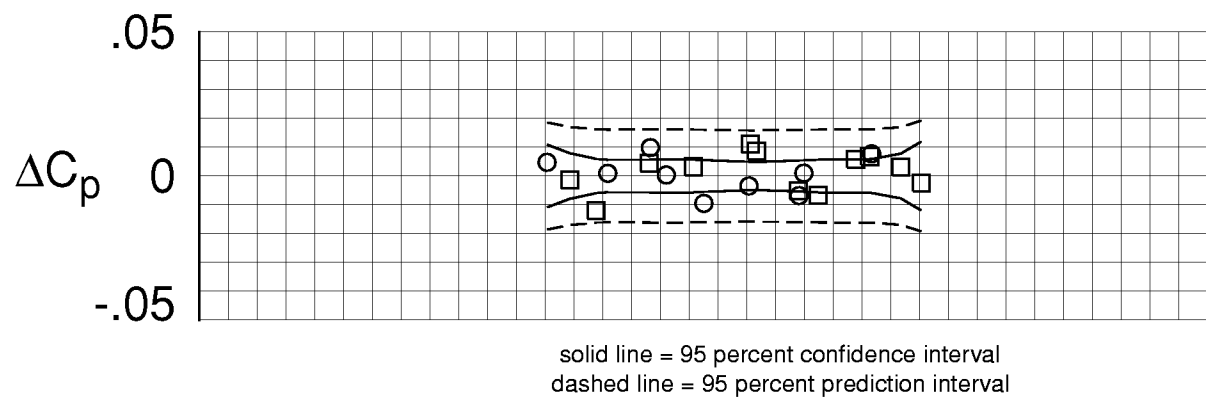


solid line = 95 percent confidence interval
dashed line = 95 percent prediction interval



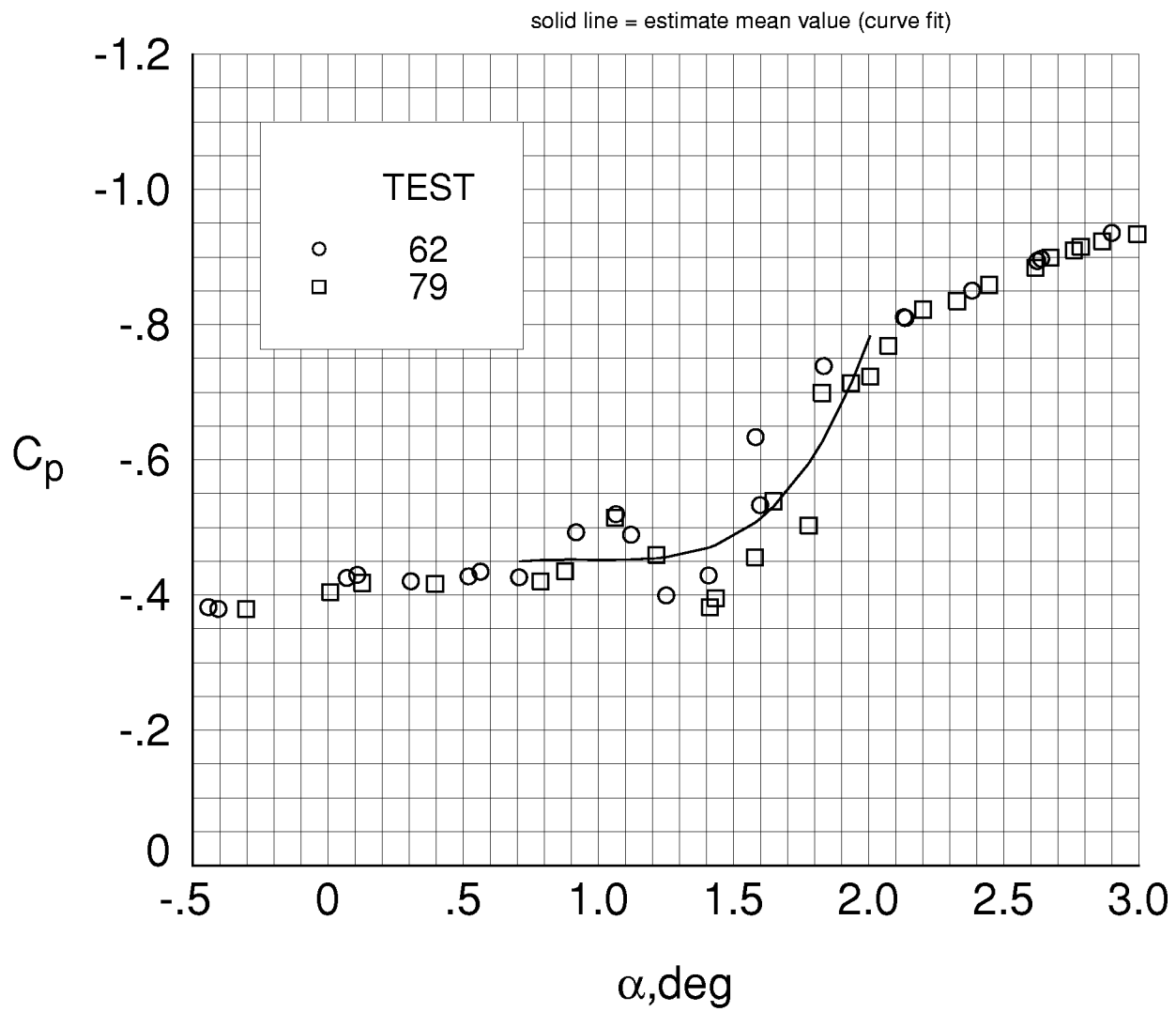
(a) $x/c = 0.05$.

Figure 10. Analysis of repeated C_p data. $\eta = 0.85$, $M_\infty = 0.85$,
 $R_c^- = 30 \times 10^6$.



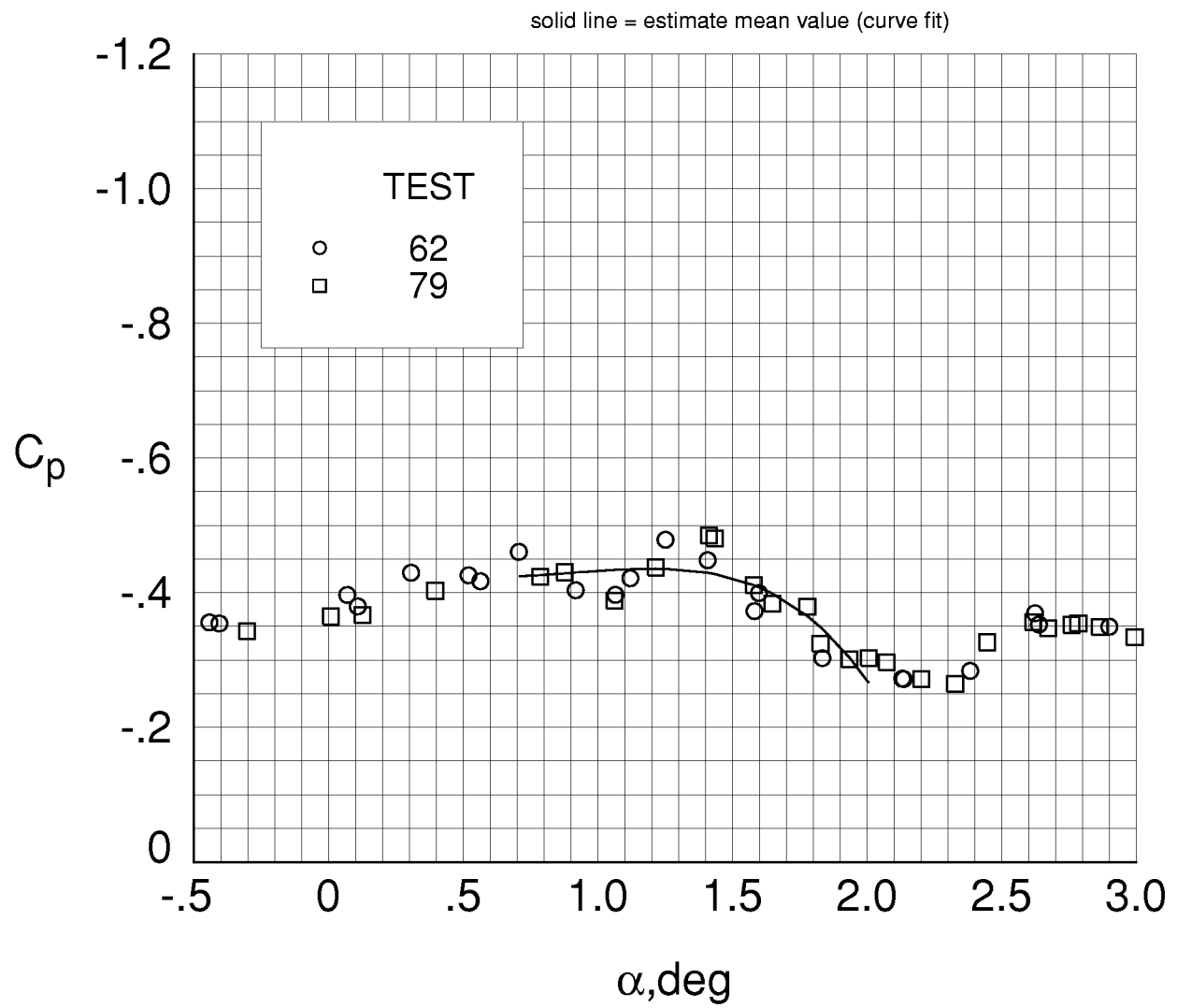
(b) $x/c = 0.25$.

Figure 10. Continued.



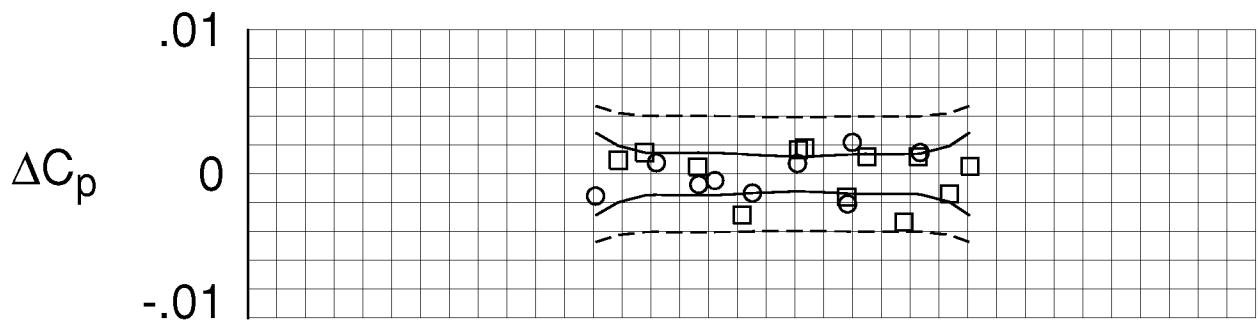
(c) $x/c = 0.45$.

Figure 10. Continued.

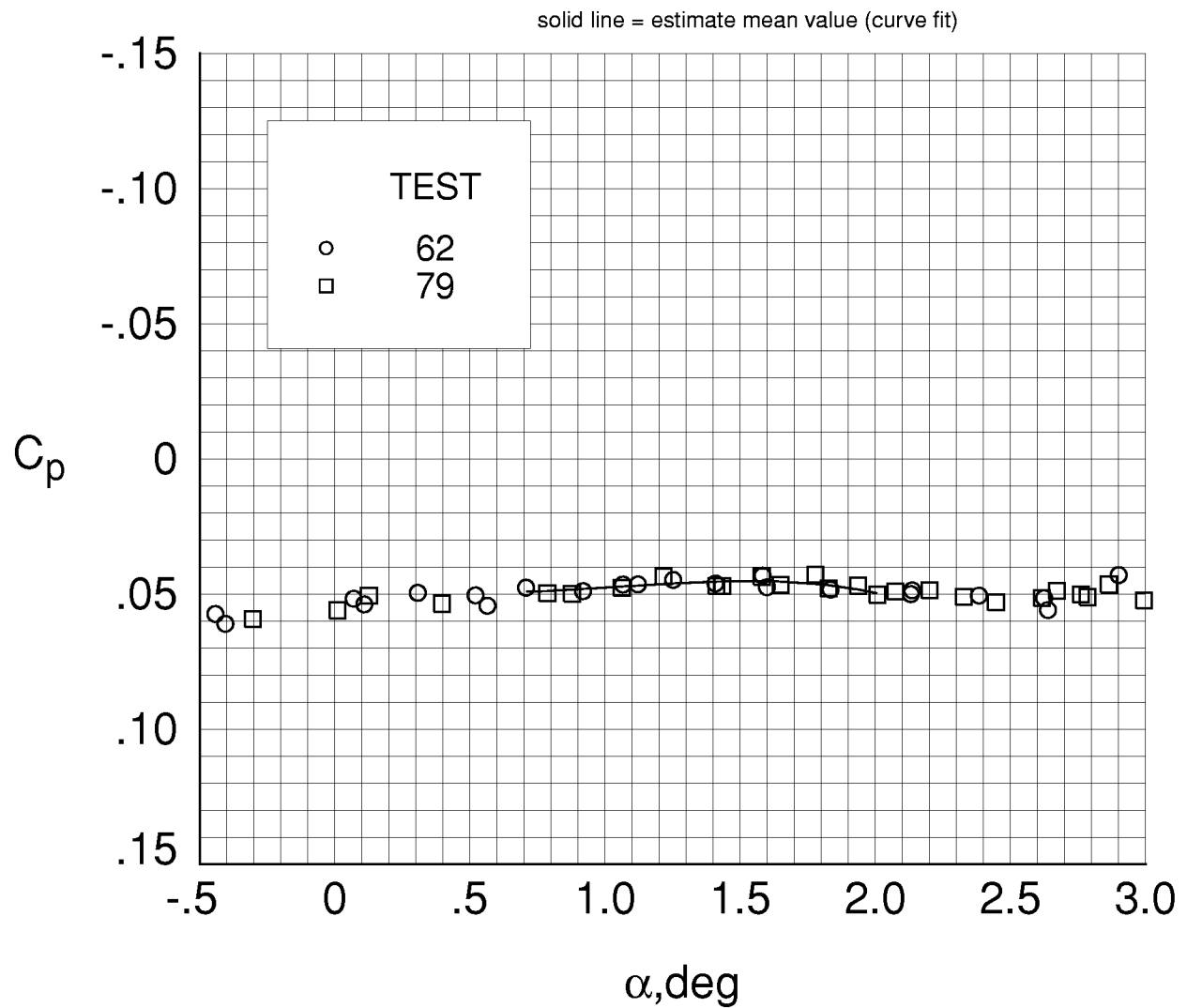


(d) $x/c = 0.62$.

Figure 10. Continued.



solid line = 95 percent confidence interval
dashed line = 95 percent prediction interval



(e) $x/c = 1.00$

Figure 10. Concluded.

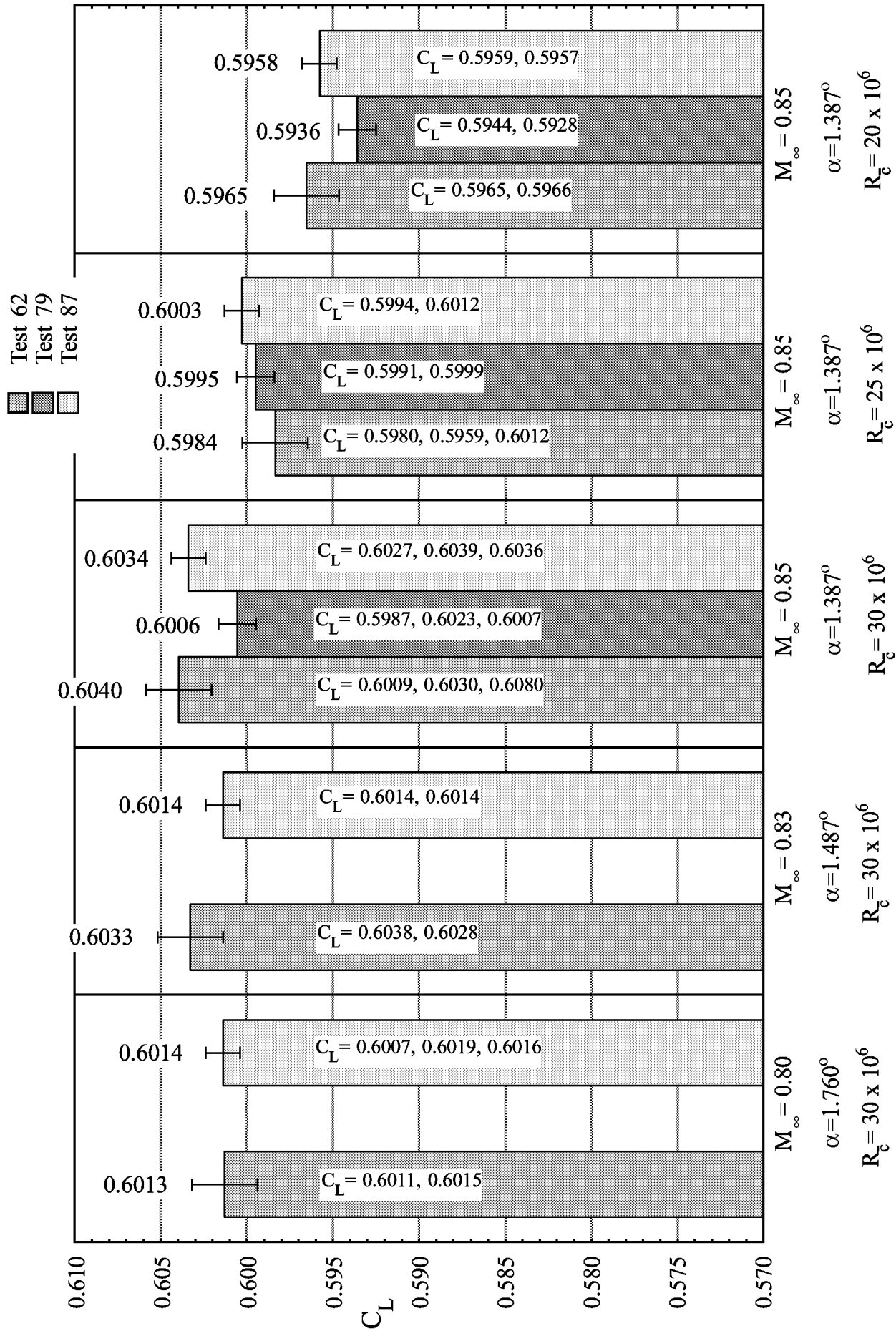


Figure 11. Lift coefficient repeatability between tests. Numbers above columns are average values, numbers used to calculate average are listed within the bar, and the error band (see Table 3) is displayed at the top of the bar.

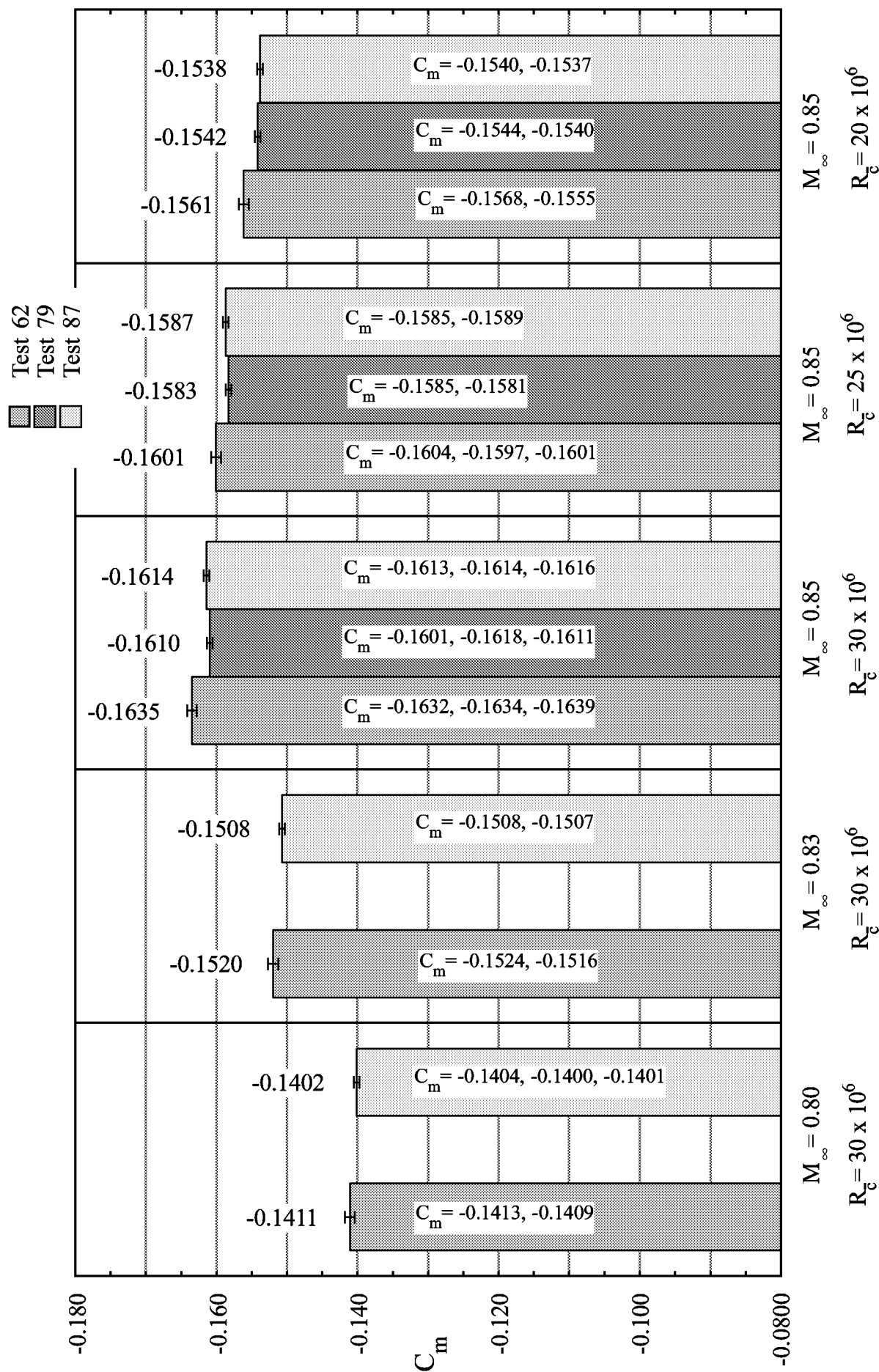


Figure 12. Pitching-moment coefficient repeatability between tests, at $C_L = 0.60$. Numbers above columns are average values, numbers used to calculate average are listed within the bar, and the error band (see Table 3) is displayed at the top of the bar.

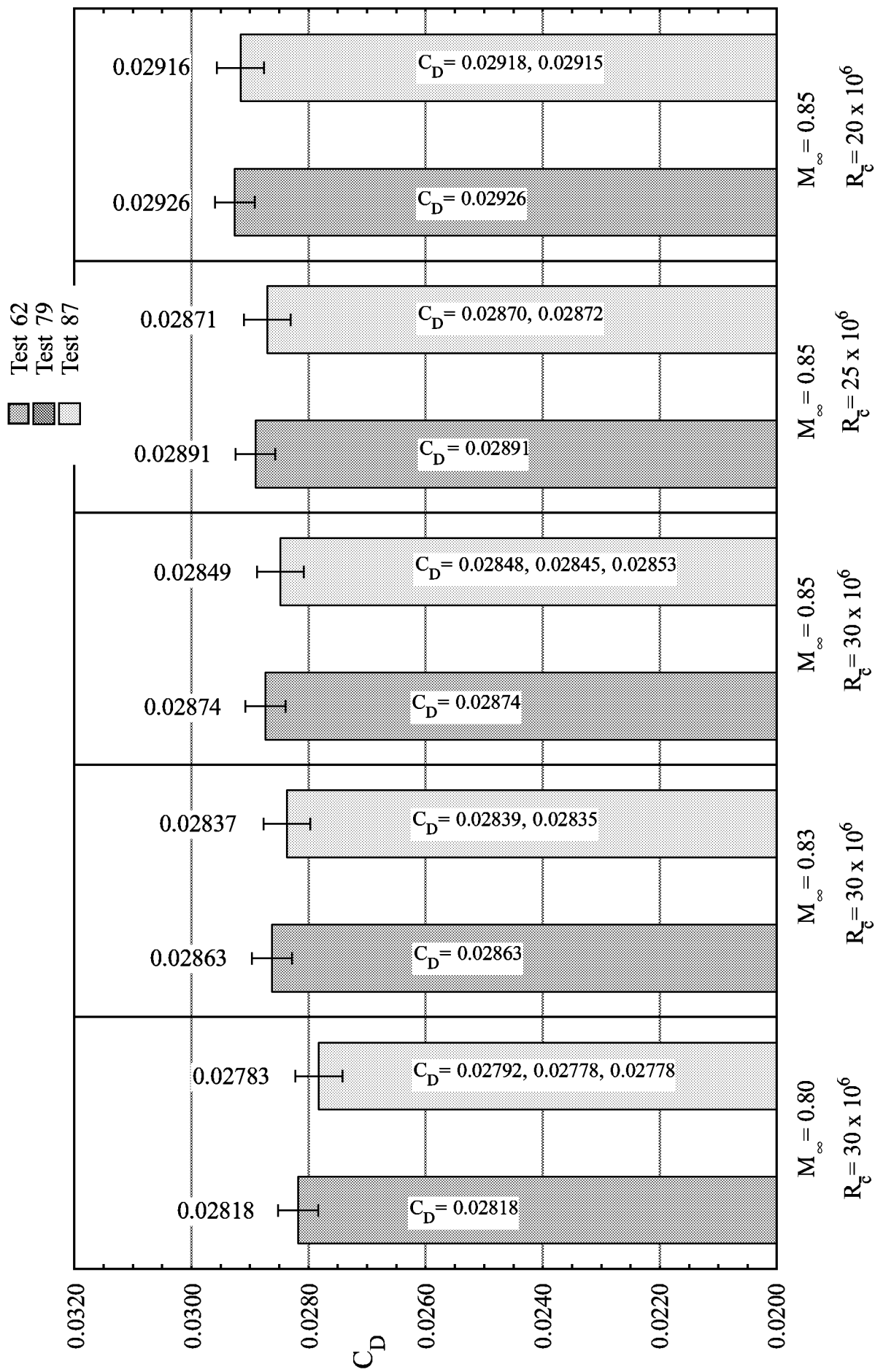


Figure 13. Drag coefficient repeatability between tests at $C_L = 0.60$, for ESP tubes out runs only. Numbers above columns are average values, numbers used to calculate average are listed within the bar, and the error band (see Table 3) is displayed at the top of the bar.

REPORT DOCUMENTATION PAGE			Form Approved OMB No. 0704-0188	
Public reporting burden for this collection of information is estimated to average 1 hour per response, including the time for reviewing instructions, searching existing data sources, gathering and maintaining the data needed, and completing and reviewing the collection of information. Send comments regarding this burden estimate or any other aspect of this collection of information, including suggestions for reducing this burden, to Washington Headquarters Services, Directorate for Information Operations and Reports, 1215 Jefferson Davis Highway, Suite 1204, Arlington, VA 22202-4302, and to the Office of Management and Budget, Paperwork Reduction Project (0704-0188), Washington, DC 20503.				
1. AGENCY USE ONLY (Leave blank)		2. REPORT DATE March 2000		3. REPORT TYPE AND DATES COVERED Technical Memorandum
4. TITLE AND SUBTITLE Test-to-Test Repeatability of Results From a Subsonic Wing-Body Configuration in the National Transonic Facility			5. FUNDING NUMBERS WU 538-14-12-01	
6. AUTHOR(S) Raymond E. Mineck and Odis C. Pendergraft, Jr.				
7. PERFORMING ORGANIZATION NAME(S) AND ADDRESS(ES) NASA Langley Research Center Hampton, VA 23681-2199			8. PERFORMING ORGANIZATION REPORT NUMBER L-17774	
9. SPONSORING/MONITORING AGENCY NAME(S) AND ADDRESS(ES) National Aeronautics and Space Administration Washington, DC 20546-0001			10. SPONSORING/MONITORING AGENCY REPORT NUMBER NASA/TM-2000-210079	
11. SUPPLEMENTARY NOTES				
12a. DISTRIBUTION/AVAILABILITY STATEMENT Unclassified-Unlimited Subject Category 02 Distribution: Nonstandard Availability: NASA CASI (301) 621-0390			12b. DISTRIBUTION CODE	
13. ABSTRACT (Maximum 200 words) Results from three wind tunnel tests in the National Transonic Facility of a model of an advanced-technology, subsonic-transport wing-body configuration have been analyzed to assess the test-to-test repeatability of several aerodynamic parameters. The scatter, as measured by the prediction interval, in the longitudinal force and moment coefficients increases as the Mach number increases. Residual errors with and without the ESP tubes installed suggest a bias leading to lower drag with the tubes installed. Residual errors as well as average values of the longitudinal force and moment coefficients show that there are small bias errors between the different tests.				
14. SUBJECT TERMS Repeatability; National Transonic Facility; Low Wing Transport; Wing-Body; High Reynolds Number			15. NUMBER OF PAGES 81	
			16. PRICE CODE A05	
17. SECURITY CLASSIFICATION OF REPORT Unclassified	18. SECURITY CLASSIFICATION OF THIS PAGE Unclassified	19. SECURITY CLASSIFICATION OF ABSTRACT Unclassified	20. LIMITATION OF ABSTRACT UL	